Carbon Hybrids Electrocatalysts for Oxygen Reduction Reaction in Fuel Cells

By Mo Qiao

Supervisor: Prof Maria-Magdalena Titirici

A thesis submitted for the Degree of Doctor of Philosophy

School of Engineering and Materials Science

Queen Mary University of London

London, United Kingdom

September 2018

Statement of originality

I, Mo Qiao, confirm that the research included within this thesis is my own work or that where it has been carried out in collaboration with, or supported by others, that this is duly acknowledged below and my contribution indicated. Previously published material is also acknowledged below.

I attest that I have exercised reasonable care to ensure that the work is original, and does not to the best of my knowledge break any UK law, infringe any third party's copyright or other Intellectual Property Right, or contain any confidential material.

I accept that the College has the right to use plagiarism detection software to check the electronic version of the thesis.

I confirm that this thesis has not been previously submitted for the award of a degree by this or any other university.

Signature:

Date:

Acknowledgement

To pursue a PhD degree in a country with a contrasting cultural environment is a vital and essential experience in life. It made me understand a variety of culture backgrounds, learn to view and think in a different way both towards science and people. The challenges from both culture and research developed me both as a person and a scientist. I will always fondly remember this unforgettable experience. I sincerely thank China Scholarship Council and Queen Mary University of London for awarding me the CSC-QMUL scholarship, to enable me to pursue my PhD in QMUL.

I would like to thank my supervisor Prof. Maria-Magdalena Titirici for her endless support, patience and encouragement when I struggle with my study and life in the UK. I feel fortunate to have the opportunity to work with her. I admire her forever-lasting enthusiasm towards science and life, her open-minded welcomeness to potential collaborators, and always being energetic and optimistic regardless of the situation. The experience of travelling twice to China with her are eternally etched with happy memories, particularly the day we both got totally soaked by rain on the Great Wall !

I would also like to extend my thanks to all the collaborators and visitors from different parts of the world: Prof. Qiang Zhang and Dr. Cheng Tang was actively involved throughout my PhD research, and they have been an incredible source of information, support and guidance. And Prof. Nicole Grobert, Prof. Yongsheng Hu, Dr Marta Sevilla, Dr Seyyed Shayan Meysami, Dr Yuesheng Wang, Dr.

Guillermo A. Ferrero, Dr Leticia F. Velasco, and the QMUL technician team, all of them have provided incredible support and helpful advices on material synthesis and characterization. Without them this dissertation would not be possible.

I convey my grateful acknowledgement to my colleagues. I'm grateful to Kathrin, Nikos and Servann for the four years of companionship in the lab. I'm grateful to all the group members for creating a superior research environment and being part of my PhD life. And also a big thank you to all of the project students who have worked with me, Wei Vern Hor, Zewen Zhang, Yingzhi Sun and many others. I have been influenced by them in a number of ways, especially their positive attitudes towards life, work and their sincerity and people skills.

A special mention of my second supervisor, Dr Russell Binions, who sadly passed away in April 2017. His shining charisma, his support and encouragement are ever present throughout my PhD. He will be forever remembered in our hearts.

Last but not least, great appreciation is dedicated to my parents and my husband, who provided unconditional love and support. My husband and I got married in the final year of my PhD, with my supervisor Prof. Maria-Magdalena Titirici being one of the witness. The wedding ceremony was one of the key highlights in my PhD.

Abstract

The oxygen reduction reaction (ORR) is a key reaction in fuel cells and metal-air batteries. This process involves multi-electron transfer and is kinetically sluggish due to the high-energy barriers required to break the O-O bond. Current commercial Pt-C electrocalysts for the ORR suffer from high-cost and easy degradation; therefore, the development and rational design of alternative electrocatalysts for the ORR are important. Numerous efforts have been devoted to the development of environmentally benign electrocatalysts of high-performance and low cost. Among those, carbon-based materials have been considered promising alternatives for Pt-free ORR due to their distinct advantages such as high electrical conductivity, low cost, stable physical, and chemistry properties. This thesis includes the synthesis of hydrothermal carbon-graphene hybrid materials as electrocatalysts for ORR, and the engineering on the interface of carbon electrocatalysts at the triple point for enhanced ORR performance. The fundamental knowledge and the research background are introduced and summarized in Chapter 1 and Chapter 2, Chapter 3, respectively. The innovative research work is presented in the subsequent chapters:

In Chapter 5, N-doped nanocarbon/graphene composites were carefully designed as electrocatalysts in ORR, in order to decouple the influence of active sites and electric conductivity, and investigate the underlying relationships between them. Results show that a low conductivity limits the exertion of active sites and results in a conductivity-dependent ORR activity. However, when the conductivity reaches critical value, the active sites can be fully utilized and contribute to a positively correlated ORR activity.

In Chapter 6, an effective strategy was proposed to enhance the oxygen reduction reaction (ORR) performance of MWCNTs in both acid and alkaline electrolytes by coating them with a layer of biomass derivative N-doped hydrothermal carbons. The N-doped amorphous carbon (NC) coating plays triple roles: it (i) promotes the assembly of MWCNTs into a 3D network therefore improving the mass transfer, thus increasing the catalytic activity; (ii) protects the surface present Fe-containing active sites on the MWCNTs from H_2O_2 poisoning; (iii) creates nitrogenated active sites and hence further enhances ORR activity and robustness.

In Chapter 7, a novel and general concept was reported to improve the performance of Pt-free electrocatalysts in oxygen reduction reaction. This concept is based on the addition of oxygenophilic and hydrophobic ionic liquids (ILs) into Pt-free carbon catalyst to form a thin passivating layer at the triple point between the electrocatalyst-electrolyte-gas interface. The IL layer at the catalyst's surface provides a water-equilibrated secondary medium with a higher O_2 solubility, while its hydrophobic nature prevents water from building-up locally. It was also confirmed that the use of a protic ILs favours the ORR in both acid and alkaline media. This concept not only shows significant improvements in ORR in both alkaline and acid electrolyte, but also represents a promising method to be implemented in other renewable energy technologies (i.e. metal-air batteries, supercapacitors) where nanocarbons with improved surface properties are required.

Contents

List of abbreviations and symbols

AFHG	Amine functionalized hole graphene
BET	Brunauer–Emmett–Teller
CNTs	Carbon nanotubes
CQDs	Carbon quantum dots
CS	Chitosan
CV	Cyclic voltammetry
CVD	Chemical vapour deposition
DMFC	Direct methanol fuel cell
EDA	Ethylenediamine
EDS	Energy dispersive spectroscopy
EIS	Electrochemical Impedance Spectroscopy
FTIR	Fourier-transform infrared spectroscopy
GC	Glassy carbon
GN	Nitrogen doped graphene
GO	Graphene oxide
GQD	Graphene quantum dots
HRTEM	High-resolution transmission electron microscopy
HTC	Hydrothermal carbonization
IL1	1-butyl-3-methylimidazolium bis(trifluoromethanesulfonyl) imide
IL2	1-ethylimidazolium bis(trifluoromethylsulfonyl) imide
LSV	Linear sweep voltammograms

MWCNTs	Multi-wall carbon nanotubes
N-CDs/G	N doped carbon dots decorated on graphene
NC	Nitrogen-doped carbons
NCG	NC/graphene composites
NG-NCNT	Nitrogen doped graphene/carbon nanotube nanocomposite
NPGC	N doped porous graphene/carbon
ORR	Oxygen reduction reaction
PEM	Proton-exchange membrane
QSDFT	Quenched Solid Density Function Theory
rGO	Reduced graphene oxide
RDE	Rotating disk electrode
RRDE	Rotating ring-disk electrode
SEM	Scanning electron microscope
TEM	Transmission electron microscope
TGA	Thermogravimetric analysis
TPB	Triple phase boundary
XPS	X-ray photoelectron spectroscopic data
XRD	X-Ray diffraction

List of Figures

List of Tables

1 Introduction

1.1 Fuel cells

The fast-increasing living standards stimulate the global demand for energy. Advanced energy conversion and storage thus play crucial roles in exploiting renewable clean energies, which stimulate significant advancements of the related technologies such as fuel cells, rechargeable batteries, and supercapacitors. Fuel cells are expected to come into widespread commercial use in the areas of transportation, stationary and portable power generation, and thus will help to solve energy shortage and environmental issues. Generally, in a fuel cell, hydrogen molecules react with oxygen and produce water as the only by-product, and clean electricity can be therefore generated by an electrochemical reaction.

There are different types of fuel cells: Proton exchange membrane (PEM) fuel cells, direct methanol fuel cells (DMFC), alkaline fuel cells, phosphoric acid fuel cells, solid oxide fuel cells, etc. Each of them possesses its own advantages and limitations. For example, PEM fuel cell and alkaline fuel cells are most widely used due to their relative low operating temperature and high-power density.[1] Proton exchange membrane (PEM) fuel cells, also known as polymer electrolyte membrane fuel cells, are suggested by the U.S. Department of Energy (DOE) as the primary candidates for light-duty vehicles, buildings, and potential alternatives to much smaller applications such as rechargeable batteries. PEM fuel cells operate at relative low temperatures (around 80 °C), which allow quick start-up (less warm-up time) and less wear on the system components, and therefore lead to a better durability. PEM fuel cells demonstrate high power density but are low in weight

and volume compared with other fuel cells. However, these cells are sensitive to fuel impurities such as carbon monoxide poisoning, therefore additional setup to remove the impurities is required, which increases the overall cost. Alkaline fuel cells (AFCs), on the other hand, were one of the first developed fuel cell technologies. They were long used by the National Aeronautics and Space Administration (NASA) on space missions to generate electrical energy and water on-board spacecraft. The power generation efficiencies of the AFCs can be up to 70%. They use potassium hydroxide (KOH) as the electrolyte and operates at around 70 °C. Hydrogen and oxygen are supplied as reactants, and their high purities are tightly regulated due to the susceptibility of AFCs towards carbon contamination.

1.1.1 Basics of fuel cells

Fuel cells consist of three active components: fuel electrodes as anodes, oxidation electrodes as cathodes, and the electrolyte between them. For a single electrode, it is usually composed of a proton conducting media, an electrocatalytically active catalyst, and an electron-conducting fibres.[1] **Figure 1-1** shows schematic configuration and basic operational process of the PEM fuel cell and alkaline fuel cell.

Take the operational process in PEMFC for an example:

Molecular hydrogen (H_2) is transported from the supplied gas-flow to the anode, where it electrochemically oxidized to produce H^+ and electrons:

$H_2 \rightarrow 2H^+ + 2e^-$ Equation 1-1

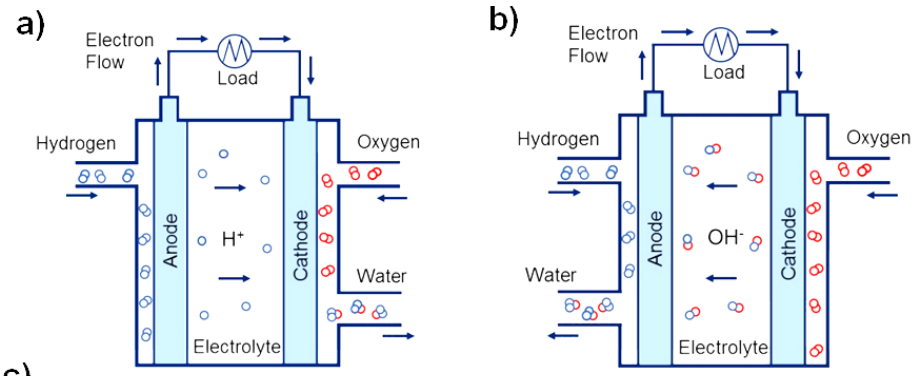

c)

Alkaline media:	$O_2 + 2H_2O + 4e^- \rightarrow 4OH^-$ *(Four-electron process)*
	$O_2 + H_2O + 2e^- \rightarrow HO_2^- + OH^-$ *(Two-electron process)*
	$H_2O + HO_2^- + 2e^- \rightarrow 3OH^-$
Acid media:	$O_2 + 4H^+ + 4e^- \rightarrow 2H_2O$ *(Four-electron process)*
	$O_2 + 2H^+ + 2e^- \rightarrow H_2O_2$ *(Two-electron process)*
	$H_2O_2 + 2H^+ + 2e^- \rightarrow 2H_2O$

Figure 1-1 Schematic illustration of (a) a PEM fuel cell and (b) an alkaline fuel cell, the red and blue circles in the figure demonstrate oxygen and hydrogen atoms, respectively. (c) ORR pathways in acid and alkaline media

The produced H^+ are then conducted by the proton-conductive electrolyte from the anode to the cathode in response to the reactive attraction of hydrogen to oxygen, whilst the electrons are transmitted to the cathode through the external circuit towards the cathode which provides useful electrical work. At the cathode, the transmitted electrons, the electrons that passed through the external circuit, together with the oxygen supplied by cathodic flow combined to form water:

$$\frac{1}{2}\,O_2 + 2H^+ + 2e^- \rightarrow H_2O \quad \text{Equation 1-2}$$

The overall reaction in this fuel cell produces water, heat, and electricity as shown below:

$$H_2 + \frac{1}{2}O_2 \rightarrow H_2O + W_{ele} + Q_{heat} \quad \text{Equation 1-3}$$

The heat and water by-products need be continuously removed with the cathodic outlet flow, in order to maintain ideal isothermal management for continuous electric power generation.[1]

1.1.2 Fuel Cell performance and evaluation

The evaluation of fuel cell devices varies from case to case. In general, it can be considered in four aspects: physical factors, performance factors, durability and running costs. Physical aspects include numbers of cells, stacks, and total size and weight of the whole fuel cell system. It is important to meet the design constraints of size and weight of the fuel cell system especially in the area of transportation and portable device applications. Performance evaluation includes the study on the polarization, power density and system efficiency. The power density curve illustrates the flexibility of the output power that the stack system produces. The optimum operation points (voltage, current and power) of the device system can be determined by the power density curve in combination with the polarization curve.[2] Durability is another main factor when evaluating a fuel cell stack, so that the power generation system functions with minimum maintenance for the expected duration. Furthermore, the running cost of the fuel cell system would be another main concern when considering commercial application.[1]

1.1.3 Polarization curve of fuel cell

The polarization curve characterises the voltage output of the fuel cell for a given current density loading by plotting the cell potential against the current density. The polarization curves are usually obtained using a potentiostat/galvanostat, which set a fixed current from the fuel cell by slowly “stepping up” the load on the potentiostat, and meanwhile

measures the fuel cell output voltage response. It depicts the losses experienced by the fuel cell which would otherwise achieve its ideal performance (**Figure 1-2**).[3]

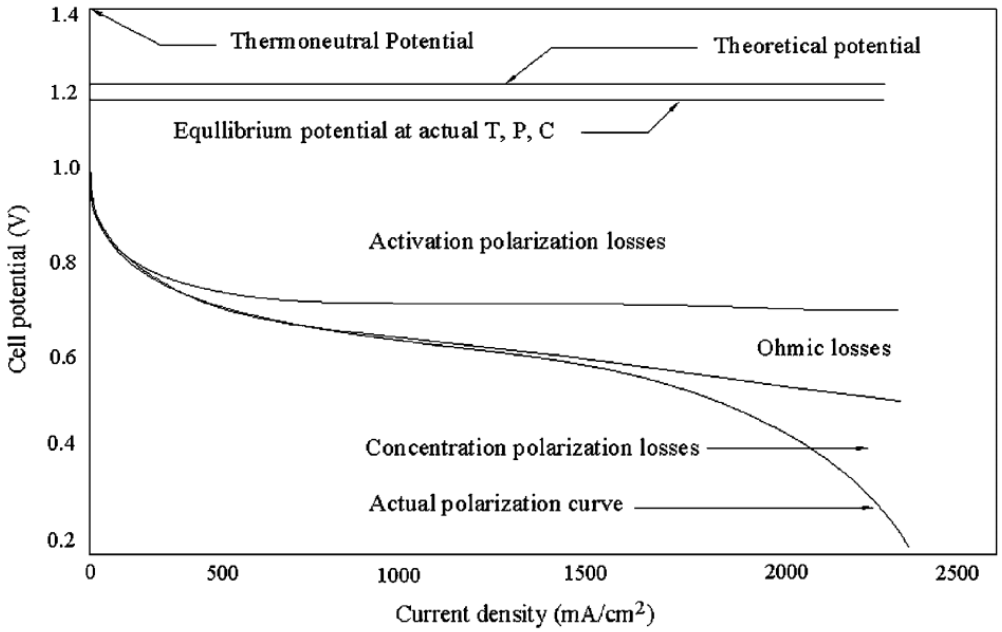

Figure 1-2 A typical polarization curve for a hydrogen–oxygen polymer electrolyte membrane fuel cell. [4]

There are three distinct regions of a fuel cell polarization curve:

I. Activation polarization:

Activation polarization is the overpotential required to overcome the energy barrier for the electron transfer reaction to occur at the electrodes. This overpotential reduces the maximum potential even under open-circuit conditions and dominates the voltage losses at low current density. This type of polarization indicates the catalyst effectiveness at a given temperature.

II. Ohmic polarization:

Ohmic polarization is due to the voltage loss because of the intrinsic electrical resistance of the cell components (electrolyte, the catalyst layer, the gas diffusion layer, etc) when charges flow. This causes the decrease of cell potential which is linear with current. The ohmic polarization region is dominated by the internal ohmic losses and is the desirable operating regime for a fuel cell.

III. Concentration polarization:

Concentration polarization happens due to the mass transport limitation resulted from the reactant and product concentrations. In a working fuel cell, the fuel and oxidant need to be continuously supplied to produce electricity, whilst the products need to be removed constantly to achieve the maximum performance. The mass transport process in a fuel cell is dominated by convention and the laws of fluid dynamics and can be reduced by improving the mass transfer and flow structures.

1.1.4 Oxygen reduction reaction

The oxygen reduction reaction (ORR) plays a critical role in fuel cells and many other systems, such as metal-air batteries and oxygen sensors.[5-8] The ORR process involves a multi-step proton-coupled electron transfer and high-energy barriers for the initial oxygen adsorption and O-O bond breaking, resulting in sluggish kinetics and low efficiencies.[9, 10] In principle, the ORR can happen in both alkaline and acid electrolyte. As shown in **Figure 1-1**c, in both media, either a two-electron transfer pathway occurs to produce peroxide species as an intermediate, or a four-electron pathway takes place which directly produce H_2O as the only by-product. Four-electron pathway is more desirable due to a higher conversion efficiency.[11] Effective catalysts are required to accelerate ORR towards

a lower onset potential, higher saturated current density, and an improved long-term stability.[12, 13]

ORR kinetics

It is expected that the oxygen reduction reaction happens at the potential range as close as possible to the reversible electrode potential with a satisfactory reaction rate also required. The relationship between electrical current and electrode over-potential follows the Butler–Volmer equation, also known as Erdey-Grúz–Volmer equation:

$$j = j_0 \cdot \left(e^{\frac{n_{\alpha_O} \alpha_O F \eta}{RT}} - e^{\frac{n_{\alpha_O} (1-\alpha_O) F \eta}{RT}} \right) \quad \text{Equation 1-4}$$

where: j is the ORR current density (the electrode current density), j_0 is the exchange current density, $n_{\alpha o}$ is the number of electrons transferred in the electrode reaction, α_o is the charge transfer coefficient, ɳ is the over-potential of ORR, F is the Faraday constant, R is the universal gas constant, T is the absolute temperature in Kelvin.

When the over-potential is high, the value of the latter term in Equation 1-4 is negligible, the equation can then be further evolved into a linear relationship between the over-potential (η) and the logarithm of the current (log *j*), where this slope is called the Tafel slope (**Figure 1-3**). The Tafel slope relates the electrochemical kinetics to the over-potential in a ORR process, a higher Tafel slope indicates faster ORR kinetics.

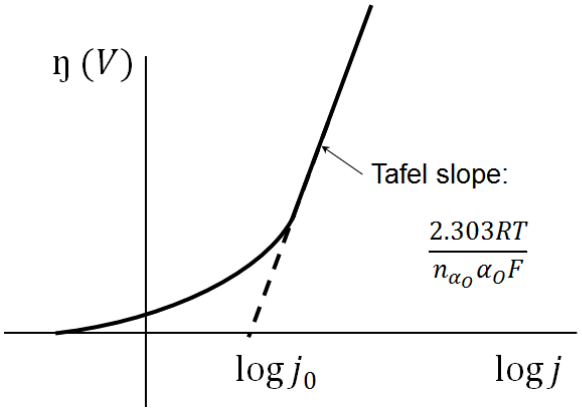

Figure 1-3 An example of the Tafel slope

ORR evaluations

A variety of electrochemical measurements are applied to evaluate the ORR performance in a three-electrode electrochemical cell. Among them, voltammetric technique is a most important and widely applied technique, in which current response is measured as a function of varied potential. A steady-state polarization curve is thereby obtained by holding the electrode potential and recording the corresponding current response. In an ORR process, high current density is expected at lower over-potential.

Cyclic voltammetry (CV) is usually the first volammetric technique performed for each sample for initial qualitative studies of new systems. During the CV measuring process, the potential between the working electrode and the reference electrode is swept back and forth within predetermined voltage range at a chosen voltage step. The current response is thereby recorded in the potential cycling region. **Figure 1-4** represents the typical CV curve of Pt-C. Six different potential regions can be depicted from the CV curve: hydrogen evolution (Pt-H formation), hydrogen adsorption (Pt-H oxidation), the double layer region, Pt oxidation (Pt-OH to Pt-O formation), Pt-O reduction (to Pt), and hydrogen

desorption region. The ORR activity can be observed from the voltage of Pt-O reduction, where higher potential shows better ORR catalytic activity.[14]

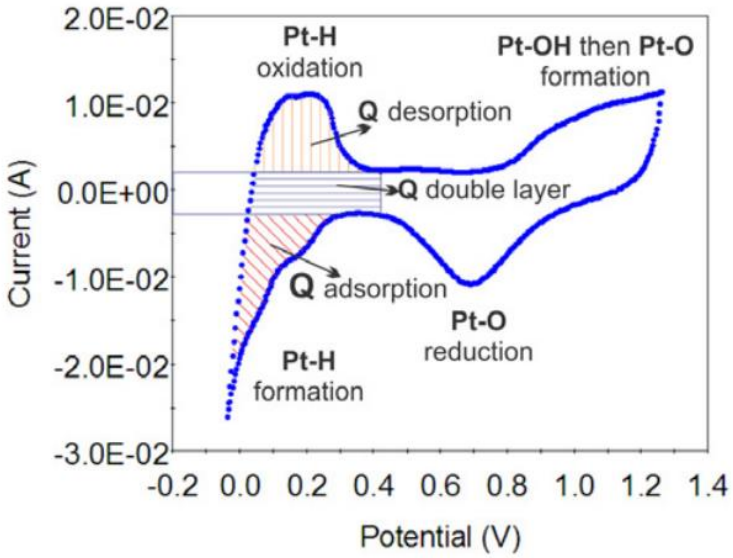

Figure 1-4 Typical CV curve of Pt-C catalyst in acidic aqueous solution[14]

Electrochemical impedance spectroscopy (EIS) is another powerful measurement based on voltammetric technique to measure the ohmic electrolyte losses in a three-electrode electrochemical cell. During the measurement, sinusoidal potential is applied to the working electrode to obtain a sinusoidal current response (**Figure 1-5**a). In addition, the EIS technique involves frequency control, which is based on the concept that an interface can be viewed as a combination of passive circuit components, such as resistance, capacitance, etc. When a chosen voltage is given, the current responses are usually represented by a Nyquist plot or Bode plot.

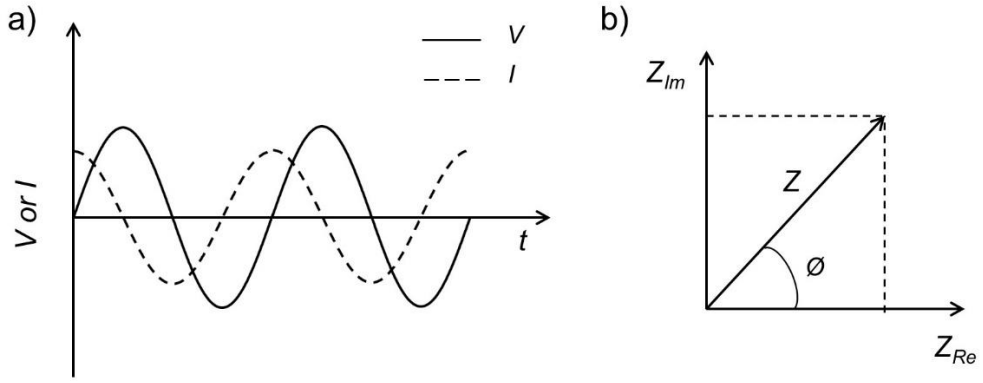

Figure 1-5 Schematic of (a) sinusoidal voltage perturbation and current response, and (b) impedance presented in the complex plane

The impedance is presented in the complex plane (**Figure 1-5**b, z = Z0 ($Cos\,Ø + j\,sin\,Ø$) = ZRe − jZIm Equation 1-5), which can be demonstrated by Nyquist plot[15]:

Z = Z_0 ($Cos\,Ø + j\,sin\,Ø$) = $Z_{Re} - jZ_{Im}$ Equation 1-5

Where Z_0 is the magnitude of the impedance, Ø is the phase angle, Z_{Re} is the real parts of the impedance Z (also demonstrated as Z'), Z_{IM} is the imaginary part of the impedance Z (also demonstrated as Z'').

When the circuit is subject to a pure resistance of value R (**Figure 1-6**a), then

$Z_0 = R,\ Ø = 0$

for all frequencies.

When the circuit is subject to a pure capacitance of C (Figure 1-6b), then

$Z_0 = \frac{1}{\omega C},\quad Ø = -\frac{\pi}{2}$

where ω is the radial frequency.

When the circuit connects the resistance and capacitance in series (***Figure 1-6***c), then

$$Z_0 = \sqrt{R^2 + \frac{1}{\omega^2 C^2}}, \quad \emptyset = \arctan(-\frac{1}{R\omega C})$$

When the circuit connects the resistance and capacitance in parallel (Figure 1-6d), then

$$Z_0 = \left(\frac{1}{R^2} + \omega^2 C^2\right)^{-\frac{1}{2}}, \quad \emptyset = \arctan(-R\omega C)$$

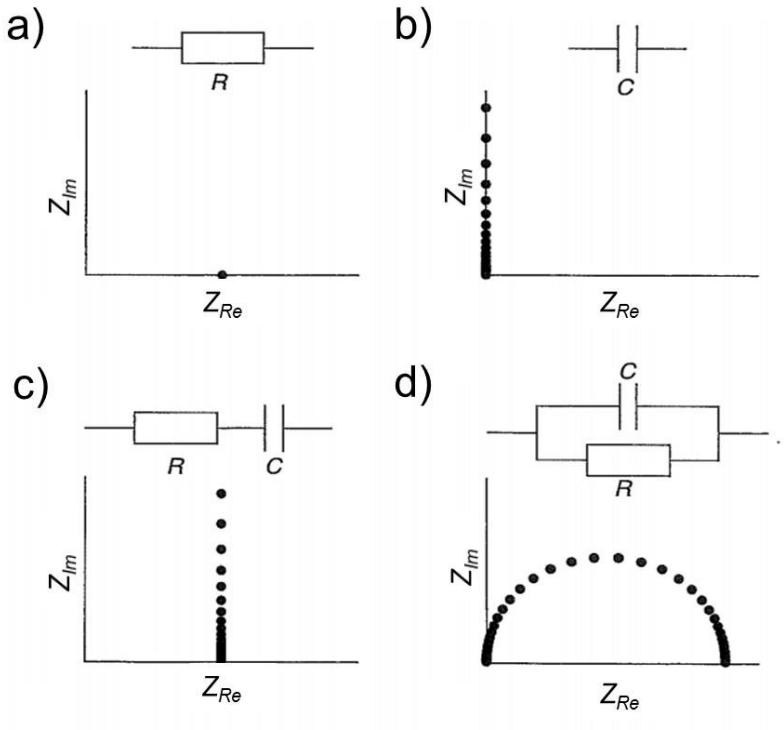

Figure 1-6 Nyquist plots for different equivalent circuits. Adapted from [15].

Many of the experimental measured EIS results are mixture of the above typical Nyquist plots, as shown in Fig 3. This is because an electrochemical cell can be modelled as a combination of different passive electrical circuit elements. Generally, in an EIS

measurement, the low frequency region is mainly controlled by mass-transfer process, and the high frequency region is mainly dominated by charge transfer process.

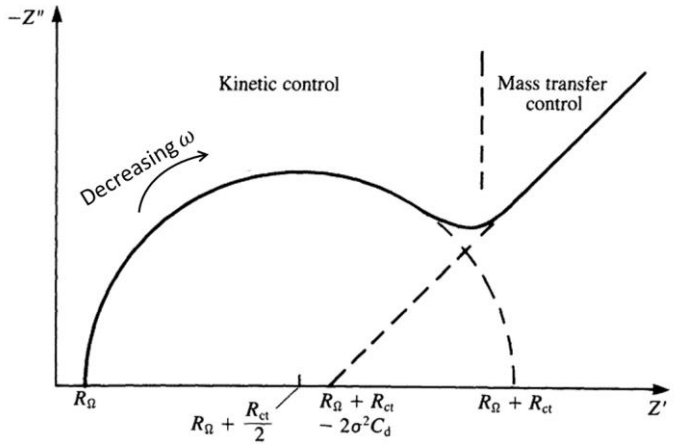

Figure 1-7 Nyquist plot of impedance in the complex plane of a simple electrochemical system. Adapted from [16].

Nyquist plots have been proved to be very useful for evaluating the impedance parameters based on the single or multiple arcs in the figures, however the information is not yet complete because the frequency is not indicated in the Nyquist plots. Bode plot, on the other hand, shows the plots of magnitude of impedance and phase angle versus frequency **(Figure 1-8).** When the circuit is dominated by resistive behaviour, a horizontal line can be observed in the presentation of log Z_0 vs log f. When the circuit is dominated by a capacitance behaviour, a straight line with a slope of -1 can be seen in the presentation of log Z_0 vs log f. Sometimes the Bode plot is shown in presentation of Z_{Re} and Z_{im} vs log f. Both forms of the Bode plot contain all the information obtained via EIS measurement.

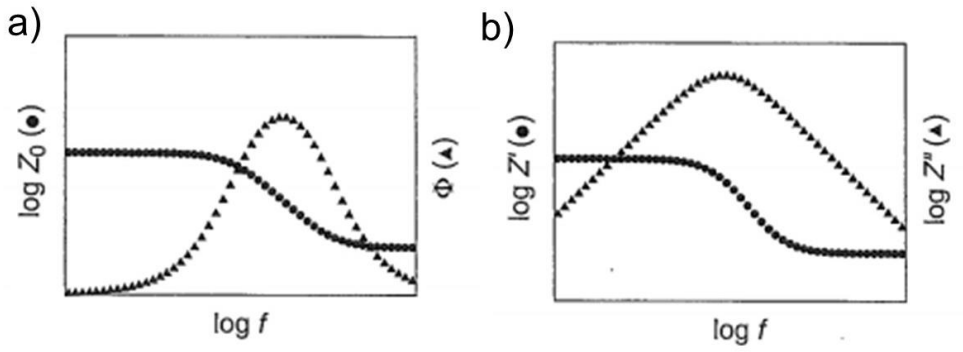

Figure 1-8 Schematic of Bode plots, adapted from [15]

Catalyst stability is a key issue to consider in development of the advanced electrocatalyst. During the ORR process, the catalysts tend to degrade due to metal dissolution (especially in acid electrolyte), carbon corrosion, and by-product poison. Chronoamperometry is widely applied to demonstrate the stability of the electrocatalysts by measuring the current response as a function of a chosen potential for a duration of time. It gives additional idea on whether the electrode can generate stable currents at fixed potential during the electrochemistry process.[17]

Three-electrode electrochemical cell test is most commonly applied to evaluate the ORR performance of a fuel cell electrocatalyst. A three-electrode electrochemical cell, as shown in **Figure 1-9**, mainly consists of three parts: a working electrode (WE) which is held by the rotating disk electrode (RDE) or ring rotating disk electrode (RRDE), a reference electrode (RE) for potential control, and a counter electrode (CE) to pass the current. In an electrochemistry process, the three electrodes are submerged in an aqueous electrolyte (either alkaline or acid) and connected to a potentiostat/galvanostat. A potentiostat uses the three electrodes to control the potential at the working electrode and measures the current flow between the working electrode and the electrolyte. A

galvanostat carries out measurement in the contrary way by controlling the current and measuring the potential.[18]

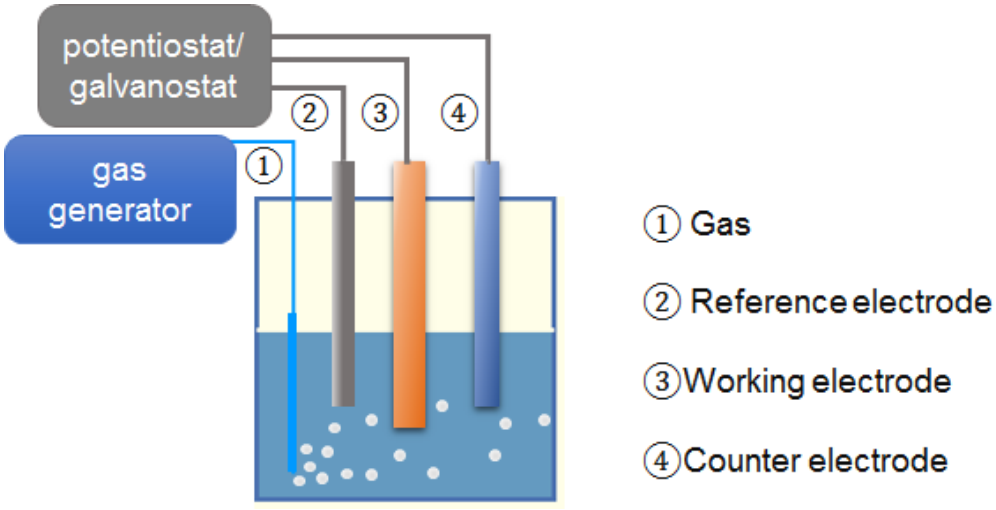

Figure 1-9 Schematic illustration of three-electrode system, the white circles in the images demonstrate the oxygen bubbles

The electrochemistry process happens on a RDE follows the Koutecky-Levich equation:[19]

$$\frac{1}{I} = \frac{1}{I_k} + \frac{1}{I_{lev}} \qquad \text{Equation 1-6}$$

where I refers to the disk current density, I_k refers to the kinetic current density, I_{lev} refers to the Levich current density. I_k and I_{lev} in Equation 1-6 can be further described by the below equations: [19]

$$I_k = nFAK_{O_2}C_{O_2}\Gamma_{catalyst} \qquad \text{Equation 1-7}$$

$$I_{lev} = 0.201nFAC_{O_2}D_{O_2}^{\frac{2}{3}}v^{-\frac{1}{6}}w^{\frac{1}{2}} \qquad \text{Equation 1-8}$$

in which, n is electron transfer number, A is the area of the electrode, K_{O2} refers to the rate constant of the reaction, C_{O_2} is the concentration of O_2 dissolved in the electrolyte,

$\Gamma_{catalyst}$ is the surface loading of the catalyst, D_{O2} is the diffusion coefficient of the O_2, *v* is the kinematic viscosity of the electrolyte solution, while *w* is the rotation rate of the RDE represented by rpm.

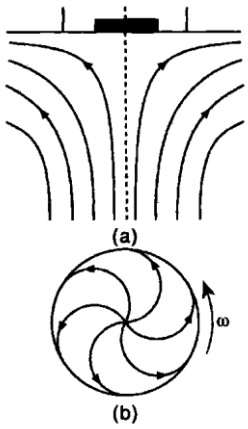

Figure 1-10 Schematic illustration of the flow pattern created by the RDE. (a) view from the side showing how the solution is pumped towards the disc, then thrown outwards. (b) view from below, solution flow close to the electrode surface.[18]

An RDE electrode is powerful in hydrodynamic control by setting a variety of rotating rates to control the flow of electrolyte to the electrode surface, which thereby dominates the diffusion layer thickness (**Figure 1-10**): At high over-potential, a limiting current may be obtained. This limiting current is dominated by the thickness of the diffusion layer, the rate of reaction, as well as the scan rate in the electrochemistry process, and therefore varies with different rotating speed of the RDE. The thickness of the diffusion layer could be decreased by increasing the rotating speed of the RDE, which leads to a high level of diffusion flux at the electrode interface. This technique enables forced convection and reduces the diffusion layer thickness compared with natural convection.

A RRDE consists of similar structure to the RDE, meanwhile, it contains a ring electrode as an additional working electrode (**Figure 1-11**a). These two electrodes work independently and are separated by an electrical insulating barrier. The overall flow pattern at the RRDE initially brings molecules or ions to the disk electrode. After encountering the disk electrode, the subsequent outward radial flow carries a portion of these molecules or ions across the surface of the ring electrode (**Figure 1-11**b). This flow pattern allows the upstream products generated by the half reaction at the disk electrode to be detected as they are swept downstream and pass the ring electrode.[18]

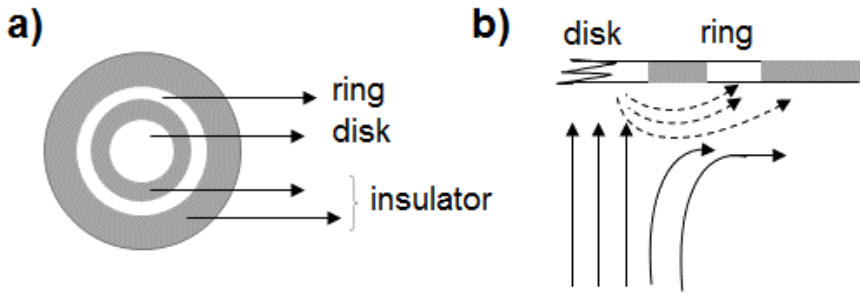

Figure 1-11 (a) Illustration of the RRDE structure from the view from below, and (b) the solution flow pattern at the RRDE surface[18]

1.2 Electrocatalysts for ORR in fuel cells

Metallic Pt and Pt-based alloys are considered the best performing and efficient electrocatalysts. However, the high cost, scarcity, unfavourable geographic distribution, and poor stability, severely hinder the large-scale application of Pt in these fields.[13] Therefore, the development of Pt-free electrocatalysts for ORR with considerable catalytic activity and improved durability is highly desirable.

The ideal electrocatalyst for ORR requires a conductive and porous framework to facilitate electron transfer and mass/gas diffusion at the interface between the electrolyte,

active sites, and gas phase. In addition, effective and fully accessible active sites are required for superior catalytic activity. Carbon based materials have been considered promising alternatives for ORR. Porous carbons have been regarded to be promising candidates because of their unique electronic and tuneable nanostructured features, as well as their robustness, giving them great potential as the catalyst matrix for electrocatalytic process in electrolytes.[20] Nanocarbon catalysts coordinated with heteroatoms, especially N-doped nanocarbon in coordination with transitional metals (Fe, Co Ni, etc.), have demonstrated comparable catalytic performance with commercial Pt in both acid and alkaline electrolyte.[21]

1.2.1 Graphene materials

Graphene is a one-atom thick layer carbon material consists of sp^2 hybrid carbon atoms which are densely packed into a two-dimension (2-D) honey comb crystal lattice. This unique structure containing the delocalized π-system provides graphene and its allotropes remarkable chemical and physical properties, such as high electrical and thermal conductivity, high stiffness, mechanical strength, high specific surface area, etc. Those distinctive properties make graphene promising candidates in overcoming limitations of conventional materials used in energy conversion and storage devices. The range of graphene materials include graphene sheets, platelets, ribbons, oxidized graphene, chemically/thermally reduced graphene and oxidized graphene ribbons unzipped originating from CNTs, etc (**Figure 1-12**). Each of those is slightly different in the compositions of the edge/defects structure and functional groups on the surface, making it different in physical and chemical properties. However, all of them possess the excellent

properties of graphene materials. Herewith hydrothermal treatment on those as-prepared graphene will be discussed as a whole.

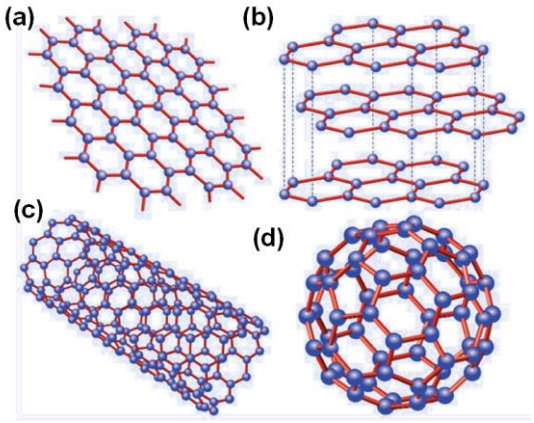

Figure 1-12 Schematic of graphene materials: (a) graphene consists of a 2D hexagonal lattice of carbon atoms, (b) graphite, which is a stack of graphene layers, (c) carbon nanotubes, which are rolled-up cylinders of graphene, and (d) buckminsterfullerene (C_{60}), of which molecule consists of graphene balled into a sphere by introducing some pentagons as well as hexagons into the lattice.[22]

Graphene was first reported to be applied as efficient metal-free electrocatalyst for oxygen reduction reaction (ORR) in the year 2009, when Liming Dai and co-workers reported a vertically aligned nitrogen-containing carbon nanotubes (VA-NCNTs) that showed superior ORR activity than commercial Pt/C catalyst.[23] Tremendous interests were then focused on the development of graphene-based metal-free electrocatalyst for ORR as promising Pt alternatives. After years of extensively investigation, rapid progress has been made in the development of graphene-based electrocatalyst. The state-of-art Pt-free catalysts reported with superior long-term stabilities, better methanol tolerance and catalytic activities, combined with supplementary techniques such as theoretical investigations and metal-poisoning tests, have strongly demonstrate the remarkable potential of graphene-based electrocatalysts.[24-28] The topological defects and edges have been proven to be active sites in recently years,[29, 30] yet the ORR catalytic activity of

pristine graphene is still largely limited by the lack of sufficient intrinsic active sites.[31-33] Therefore post-treatment that introduces extra edges, defects and heteroatom doping is highly desired to create effective active sites.

1.2.2 Heteroatom doping to create active sites

The active sites can be modulated in terms of electron density distribution, electron acceptor/donor ability, spin density, oxygen vacancies, etc. to reduce the energy barrier of O_2 adsorption and O-O dissociation.[34] As an undisputedly critical factor determining the catalytic activity, the investigations on the format and mechanisms involved in the operation of the active sites have received the most intensive attention and research efforts in recent years. Active sites can be derived from heteroatom dopant, while the edges and topological defects on graphene structure also play a role as active sites (**Figure 1-13**). The theory, potential reaction mechanisms and experimental studies on targeted and accurate design of the active sites have been thoroughly and sufficiently reviewed by researchers in the field.[35-44]

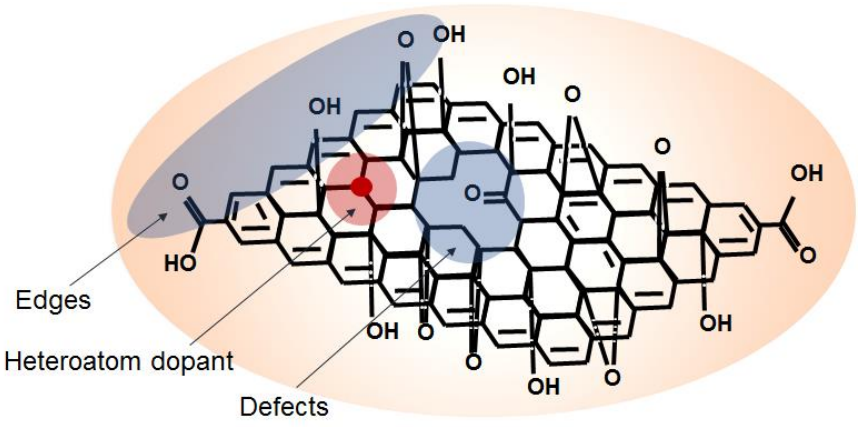

Figure 1-13 Schematic of catalytic active sites consists of heteroatom dopants, edges and topological defects on graphene structure.

The heteroatom-dopant in carbon nanostructure can make efficient active sites by inducing charge redistribution around the heteroatom dopants, which weakens the O-O bonding by changing the O_2 chemisorption mode, and therefore improves the catalytic activity of the carbon catalysts in ORR. N, P, S, B and non-precious transitional metals such as Fe, Co, Ni are most commonly used. [14, 45, 53-56] Among different dopants, Fe-N-C catalysts are particularly promising due to the balance between electrocatalytic activity and availability of resources.

The electronegativity of nitrogen (3.04) is higher than that of carbon (2.55), which results in positively charged carbon atoms becoming adjacent to the nitrogen dopants.[46] For now, it is believed that three types of N-doped configurations can play as active sites in ORR: pyridinic-N, graphitic N and pyrrolic N (**Figure 1-14**a). The specific role that each nitrogen bonding configuration plays has not yet been fully discovered, due to the complex reaction mechanism of the ORR process. Until today, there is no complete theory to fully explain the entire mechanism of the active sites. In addition to that, the difficulty to customise the specific types and amounts of doped nitrogen increase the complexity of this issue.[47] There are, however, enormous theoretical and experimental studies that have been conducted to try to uncover the role of different nitrogen bonding in the ORR performance of carbon-based catalyst.[48-50] Some research reports claim that pyridinic-N plays an important role in deciding the onset potential, while the amount of pyridinic and graphitic nitrogen determines the saturated current density.[51]

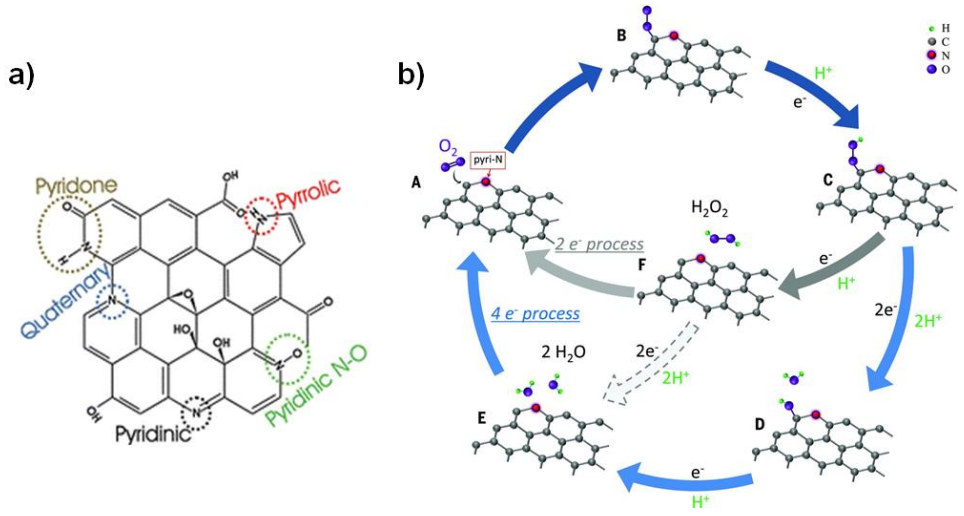

Figure 1-14 (a) Bonding configurations of N atoms in N-graphene [52] (b) Schematic pathway for oxygen reduction reaction on nitrogen-doped carbon materials in acid media.[38]

The addition of Fe in coordination with carbon and nitrogen forms highly efficient active sites by further adjusting the electron negativity and thus boosting the ORR activity. Some of Fe-N-C catalysts have been synthesized by pyrolyzing Fe-N_4-type macrocycle complexes, whilst the pyrolysis or inorganic precursors containing Fe and N are also widely applied.[53-59] The chemical configuration of Fe based active sites are mainly detected by X-ray photoelectron spectroscopy (XPS), X-ray absorption fine structure (XAFS), and Mossbauer spectroscopy, etc. It was recently proposed that the Fe based active sites mainly contain edge plan FeN_2/C, edge plan FeN_4/C, as well as basal plane macrocyclic FeN_4/C species.[60-64] In the year 2012, Kramm U.I., et al. reported that five different Fe-species were detected in the Fe-based catalysts obtained via pyrolysis of iron acetate as Fe precursor:[65] three of them are FeN_4-based sites with their ferrous ions in a low (D1), intermediate (D2), and high (D3) spin state (**Figure 1-15**), respectively, and the other two (D4 and D5) are single Fe-species consisting of surface oxidized nitride nanoparticles. The author claimed that among the five Fe-based active sites, only D1 and

D3 display catalytic activity towards ORR in acid electrolyte. This was the first time that the improved ORR kinetics of these Fe-N_4 centres was attributed to the Fe ion centres with higher electron densities. Other than the superior catalytic activity of Fe-N_x active sites, the stability of the Fe-based active sites is another critical issue that affects the ORR performance, especially in acid media. It has been reported that the pyridinic-like and pyrrolic-like Fe coordination were lost from the Fe-based catalyst during an ORR process, and the durability of the Fe-based catalysts largely depends on the stability of those porphyrazin-like Fe coordination.[66] The loss and deactivation of those Fe-based active sites can be mainly attributed to the corrosion/oxidation of the active centre and carbon support, poisoned by the intermediate by-products such as hydrogen peroxide, etc.[67, 68]

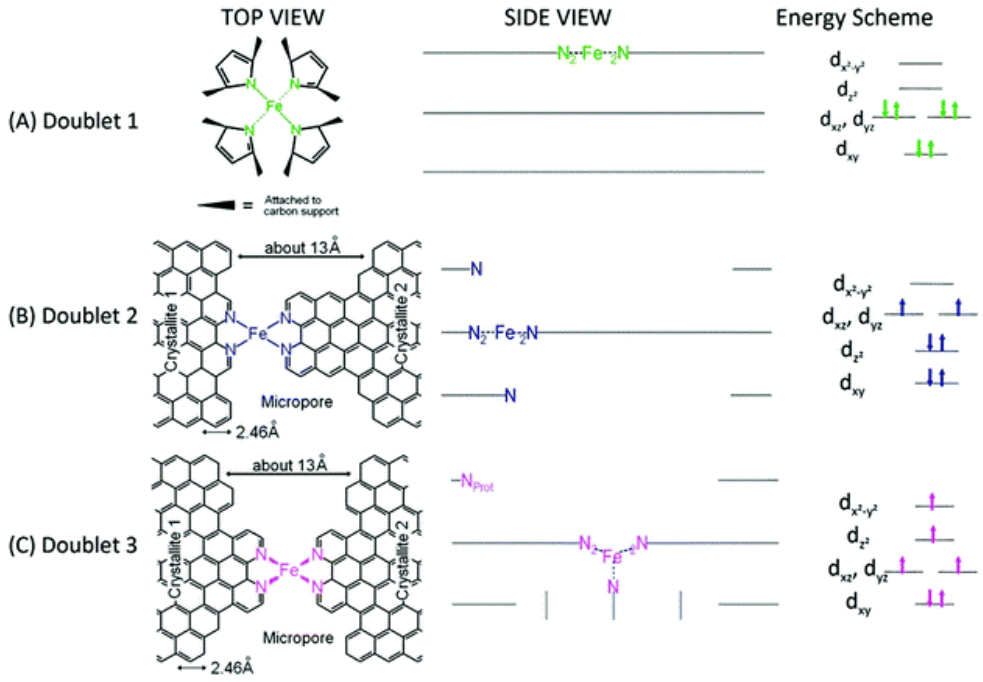

Figure 1-15 Side views and top views of the proposed structures of: (a) the FeN_4/C catalytic site in heat-treated, macrocycle-based catalysts assigned to Mossbauer doublet D1; (b) the FeN_{2+2}-like micropore-hosted site found in the catalyst prepared with iron acetate and heat-treated in ammonia assigned to doublet D2; and (c) the N–FeN_{2+2}-like composite site, where N–FeN_{2+2} is assigned to doublet D3. In all side views, graphene planes are drawn as lines.[65]

The detailed mechanism behind the high activity of Fe-N-C catalysts remains elusive and is still under debate. For example, it is not yet clear whether Fe is only involved in promoting the formation of the active sites, or if it directly catalyses ORR.[59, 63, 69-75] An example of proposed ORR pathway on N-based, and Fe, N-based active sites is listed in **Figure 1-14**b and **Figure 1-16**, respectively.[76] Up to now, it is generally accepted that Fe plays an essential role in improving the ORR activity of the catalyst and that even trace amounts of Fe lead to remarkable enhancement of ORR activity.[77-79]

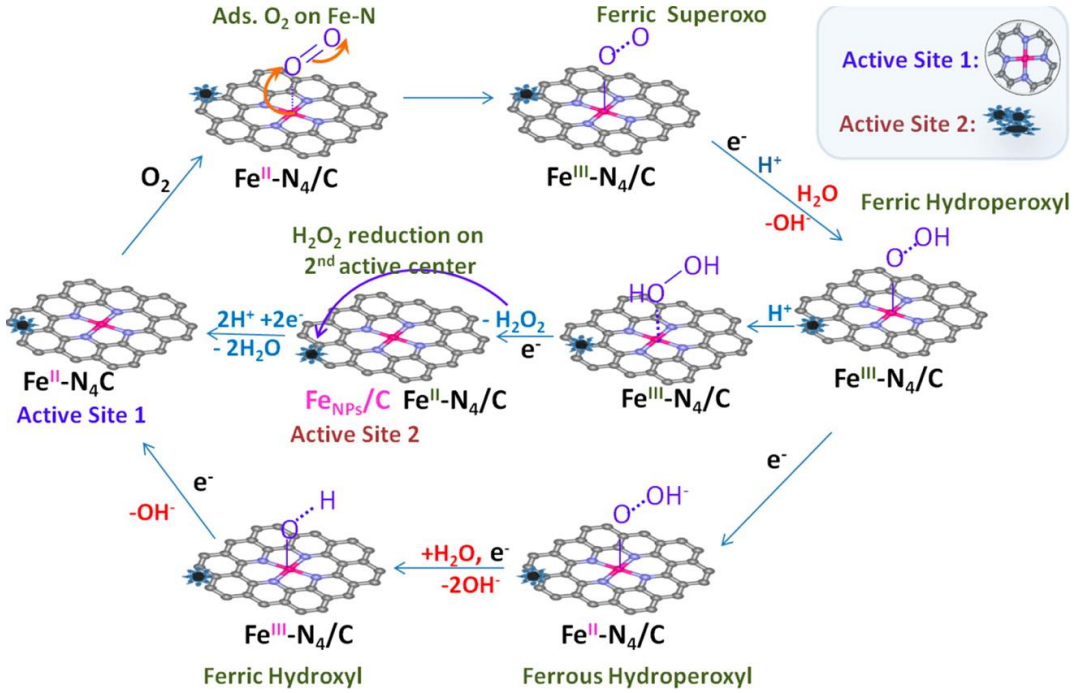

Figure 1-16 Proposed ORR mechanistic pathways on Fe–N_4/C and adjacent Fe_{NPS}/C in acidic (H^+) and alkaline (H_2O/OH^-) electrolyte.[76]

Further than the heteroatom dopant, theoretical and experimental studies have proved that edges and defects (pentagonal, zigzag edge, etc) with unpaired electrons and carboxylic groups also facilitate the O_2 trapping and electron transport, and results in a better catalytic activity.[25, 58, 80-89] The excellent catalytic activity resulted from altered charge or

spin distribution of the sp^2 panel, in which the flowing free electrons favour the O_2 adsorption and subsequently weaken O-O bond. Meanwhile, when coordinating with transitional heteroatom dopants, the defects, especially in combination with the heteroatom dopants show synergistic effects and boost the ORR activity of the catalyst.[90] Zhang Q.'s group has demonstrated the theoretical and experimental progress of topological study on the intrinsic defects and edges towards ORR reaction.[24, 29, 30, 91]

1.2.3 Hydrothermal carbonization

Among various post-treatment techniques to introduce active sites and improve ORR catalytic activity, the hydrothermal carbonization (HTC) approach appears to be a powerful technique in terms of scalability and processability.[32, 92, 93] In a hydrothermal carbonization process, reactions take place in a sealed autoclave in the presence of carbohydrate precursors and water as solvent. The sealed autoclave is then heated under certain temperatures and vapor pressures and sometimes in the presence of a catalyst. During the HTC process, accelerated physical and chemical reaction between the solvent and precursor takes place under high pressure, which promotes the decomposition of precursor into carbohydrate structure and the assembly process among different precursors to ultimately result in HTC carbonized materials/composites. The first introduction of HTC technique into materials can be traced back to 100 years ago, when people started to simulate the accelerated natural coalification and understand the process of the formation of coal.[94, 95] In comparison, HTC today has been developed into a well-established technique, and has now been widely applied to promote the assembly process of chemical reactants.[96] The scalability and processability of HTC largely compensate for

the scale-up problems in the current harsh methods such as CVD method and chemical/thermal exfoliation method in the production of graphene-based materials. Therefore, HTC becomes a powerful technique for the further development and scale-up of advanced functional carbon materials. The produced carbon materials out of the HTC approach usually consist of oxygen-containing functional groups, which make them accessible for post-functionalization treatment such as compositing and polymerization. Moreover, HTC is a very flexible synthesis approach due to its aqueous media, which makes it possible to introduce different elements into as-prepared products via solution promoted self-assembly process, and results in multi-functionalized hybrids and composites[97].

So far, HTC technology is basically classified according to applied temperature. High temperature-based HTC requires temperatures between 300 °C and 800 °C, which usually enables the synthesis of carbon nanotubes (CNTs), graphite materials as well as activated carbons. Low-temperature process, on which this project will be focused, happens below 300 °C, and this synthesis condition presumably mimics natural coalification.[94, 98]

The formation mechanism of low-temperature hydrothermal carbonization process is complicated due to various furan-type dehydrated intermediates and intricacy of chemistry.[94] To solve this problem, simple carbohydrates such as D-glucose have been utilized to understand the reaction mechanism in the HTC process. Baccile and Titirici came up with a structural model helping to solve the problem. With ^{13}C isotope in D-Glucose as the model, and combining ^{13}C NMR with GC-MS, they proposed a final structure for the HTC product derived from monosaccharide[99]. During the HTC process,

series of dehydration, polymerisation and aromatisation reactions take place, which results in a condensed furanic system bridged by aliphatic regions and terminal hydroxyl and carbonyl functional groups[100]. After initial dehydration and retro-aldol condensation, of which the former process is more favoured, hydroxymethylfurfural (HMF) results from hexoses while furfural resulted from pentose are obtained as intermediate product (**Figure 1-17**). In the following process, a nucleus forms and thus particle grows with incorporation of HMF derived monomers, resulting in spherical carbonaceous particles (**Figure 1-18**).

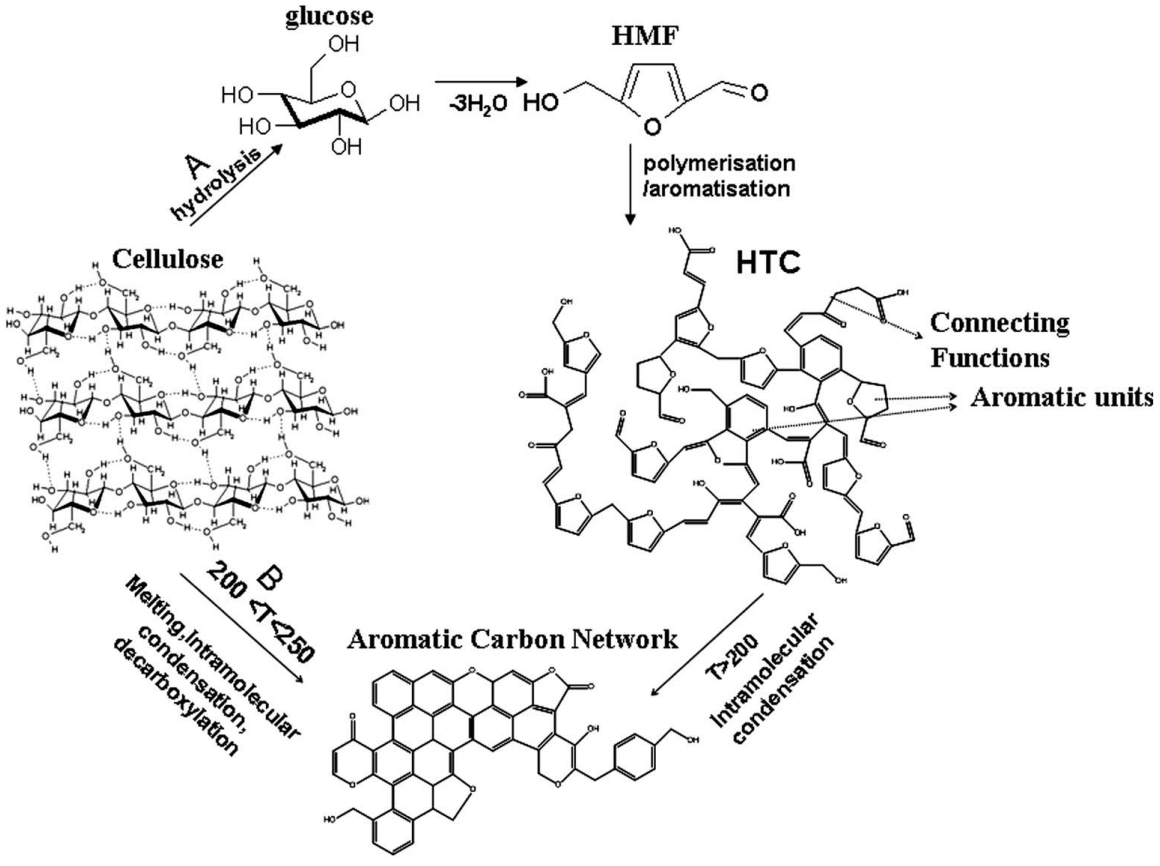

Figure 1-17 Conversion of cellulose into HTC: (A) via HMF resulting in a furan-rich aromatic network and (B) direct aromatization.[100]

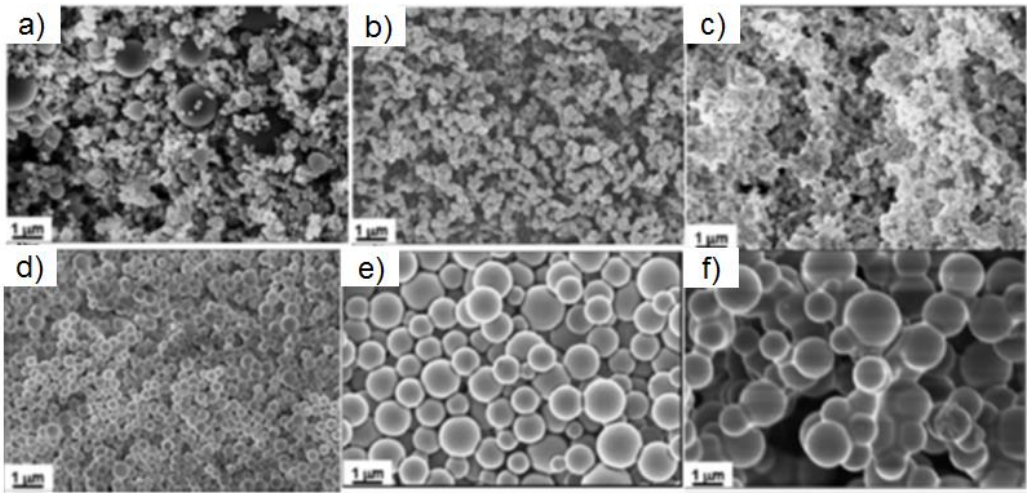

Figure 1-18 SEM micrographs of HTC materials obtained at 180 ºC from: (a) glucose; (b) fructose; (c) hydroxymethyl furfural (HMF); (d) xylose; (e) furfural; and (f) sucrose.[100]

HTC can be used to promote the assembly process of chemical reactants with other preformed carbon nanostructures. For example graphene or CNTs can be combined with nitrogen containing biomass precursors such as chitosan or urea to create functionalized hybrid materials.[101, 102] The scalability and easy processability of the HTC technique is hereby remarkably favored over other existing methods (CVD, chemical or thermal exfoliation, etc.) to produce carbon-carbon composites. HTC usually helps to develop graphene-based materials in three aspects: 1) to reduce graphene oxide (GO) into reduced graphene oxide (rGO), which is more catalyticaly active towards ORR; 2) to promote self-assembly of GO into 3-D aerogel/hydrogels; 3) to promote assembly of graphene allotropes with other compositions. In this work, HTC will be presented as assembly process of chemical reactants with other preformed carbon nanostructures resulting in multi-functionalized carbon-carbon composites and their electrochemical performance will be discussed.

1.3 Surface engineering on the nanocarbon catalyst

Numerous efforts have been devoted exploring different strategies to improve the catalytic efficiency of the nanocarbon catalysts via tailoring the carbon nanostructure, aiming to achieve a carbon matrix with superior intrinsic properties in terms of high electrical conductivity and efficient and easily accessible active sites in order to achieve a superior ORR performance.[103, 104] The precise control over the atomic structure via carefully designed synthetic routes allows the fundamental investigation of the mechanism of the active sites. However, this is very challenging to achieve in practice due to the versatility of carbon, and the fact that controlled synthesis of carbon nanostructures attracts considerable efforts.[105-109]

Another challenge in carbon electrocatalysis is the fact that the ORR happens at the interface between O_2 gas, liquid aqueous electrolyte and solid carbon catalysts. This is called the triple-phase boundary (TPB) microenvironment consisting of catalyst-electrolyte-gas bubble, where ORR reaction actually occurs. (**Figure 1-19**a-c). While different synthetic methods have been employed for the synthesis of various carbon nanostructures, approaches involving the manipulation of the TPB environment are less encountered. Several ORR pathways happen in the TPB microenvironment including multi-phase mass transfer, diffusion of reactants (O_2, protons/electrons) and products (water, etc) between the electrochemical surface and the electrolyte, surface reactions, including oxygen adsorption, interfacial charge transfer, and desorption of intermediates/products near the active sites.[44, 110-112] Hence, the optimization of this TPB microenvironment by engineering the surface of electrocatalyst, especially at the internal

pore surface, is therefore a promising method to facilitate the TPB interface chemistry and boost the activity of the active sites.

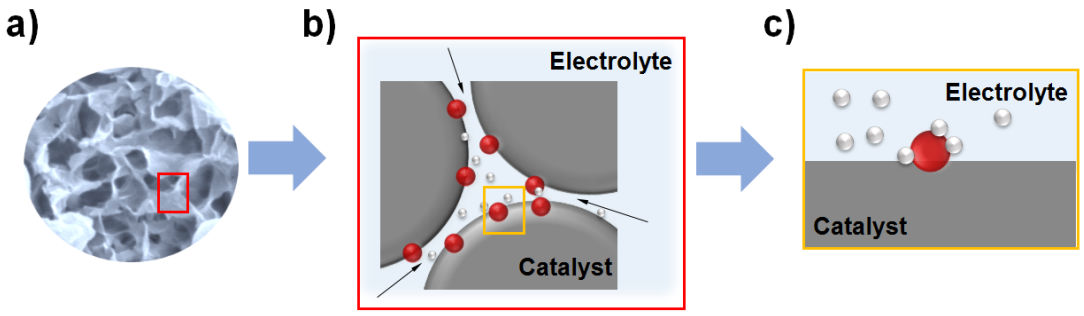

Figure 1-19 Schematic illustration of the triple-phase boundary composed by catalyst-electrolyte-oxygen: a) images of porous carbon electrocatalyst, b) schematic illustration of the red inset in (a), showing the porous nanostructure while the arrows indicate the mass transfer/diffusion of electrolyte and oxygen towards nanopores, and interaction with the active sites. c) magnification of the yellow inset in (b), showing the concept of a triple-phase boundary. The white and red spheres in the figure refer to O_2 molecules and active sites, respectively.[113]

1.4 Aims and objectives

This thesis focuses on approaches for interfacial/ surface engineering of non-precious carbon hybrids catalyst, with the aim to develop novel synthesis strategy for further development of highly efficient, stable, low cost and environmentally benign advanced nanocarbon catalysts.

In Chapter 1, the fundamental knowledge and the research background of this PhD thesis are introduced and summarized.

In Chapter 2, state-of-art application of HTC in the assembly of metal-free nanocarbon hybrids has been reviewed.

In Chapter 3, state-of-art surface engineering of non-precious metal carbon hybrid catalysts to promote ORR has been reviewed.

In Chapter 4, characterization techniques and electrochemistry measurement methods applied in this thesis are presented.

In Chapter 5, N-doped nanocarbon/graphene composites were carefully designed as electrocatalysts in ORR, to decouple the influence of active sites and electric conductivity and investigate the underlying relationships between them.

In Chapter 6, an effective strategy was proposed to enhance the oxygen reduction reaction (ORR) performance of MWCNTs in both acid and alkaline electrolytes by coating them with a layer of biomass derivative N-doped hydrothermal carbons.

In Chapter 7, a novel and general concept were reported to improve the performance of Pt-free electrocatalysts in oxygen reduction reaction. This concept is based on the addition of oxygenophilic and hydrophobic ionic liquids (ILs) onto Pt-free carbon catalyst to form a thin passivating layer at the triple point between the electrocatalyst-electrolyte-gas interface.

In Chapter 8, conclusion and perspective of this work are discussed.

2 Literature review I: Hydrothermal-graphene nanocarbon composites bases electrocatalysts for oxygen reduction reaction

This chapter focuses on summarizing the HTC assembly of metal-free carbon hybrids to present the application of HTC methodology. The transitional incorporated nanocarbon hybrids generally possess similar assembly process and principle to that of metal-free hybrids, examples will be mentioned in the following chapter.

2.1 Carbon nanostructures/biomass-derived hydrothermal carbon composites

Wu and co-workers in 2013 produced N doped graphene materials using urea as nitrogen resource. They have found that increasing the amount of urea resulted in higher N content and promoted reduction of GO in the as-prepared N doped graphene. The explanation was that during the HTC process, ammonia was slowly released from urea, which reacted with oxygen-containing functional groups leading to N doping, meanwhile ammonia also increased the pH of the solution, leading to a more effective deoxygenation of GO.[101]

Zheng and co-workers also developed N-doped graphene using the HTC synthesis of graphene with urea as nitrogen precursor (denoted as HNG), followed by an annealing at 600 °C under Ar atmosphere (denoted as HTNG). Pristine graphene was prepared by directly annealing GO for comparison (denoted as TG) (**Figure 2-1**a). The annealing process led to an increased ratio of graphitic N and a significant decrease of pyrrolic N. The annealing treatment resulted in a more positive half-wave potential, more obvious diffusion-limited region and showed a preference for a 4-electron transfer process (**Figure 2-1**b).[114] Bao and co-workers produced a sandwich-like structure comprising of N doped

porous graphene/carbon (NPGC) composites, using glucose as a carbon source and ethylenediamine (EDA) as nitrogen source. The as-obtained NPGC-950 showed excellent ORR activity which is comparable with commercial Pt on carbon. The remarkable catalytic activity was attributed to its high surface area (1512 m^2g^{-1}) and the high ratio of effective nitrogen active sites (0.26 at% of pyridinic N and 0.69% of graphitic N).[115]

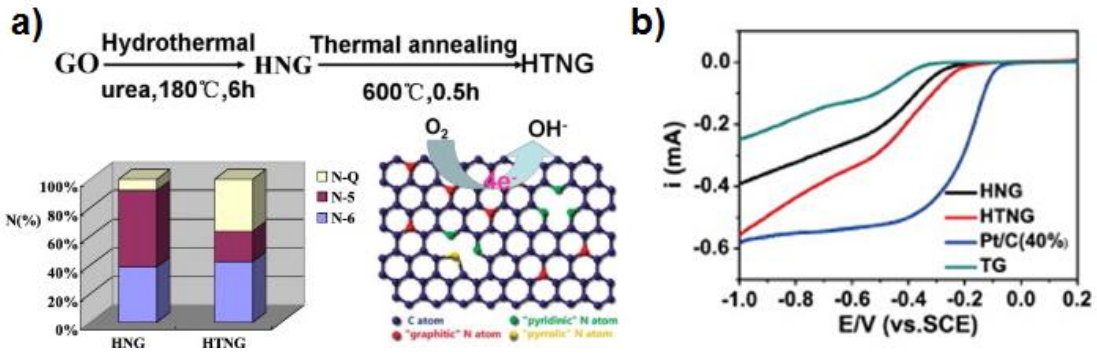

Figure 2-1 (a) Graphital abstract demonstrate the HTC assembly process and ORR pathway. (b) Linear sweep voltammetric curves (LSVs) of ORR at HNG/GCE, HTNG/GCE, TG/GCE and Pt disk electrode in an O_2-saturated 0.1 M KOH aqueous solution (scan rate: 10 mV/s, rotation rate: 1200 rpm).[114]

Niu and coworkers in 2016 developed a rationally designed strategy for one-pot N doped carbon dots decorated GO hybrid (N-C dots/GO) (**Figure 2-2**A). Urea was applied not only as a nitrogen resource, but also as an anchor for citric acid (which was the precursor for the carbon dots) on GO via the amination reaction. The GO/Urea/Citric acid intermediate was carbonized to form *in situ* N doped C dots on GO. The onset potential of the N doped C dots/GO is slightly more negative than commercial Pt-C (~100 mV), while the current density is comparable with that of Pt-C (**Figure 2-2**B).[116]

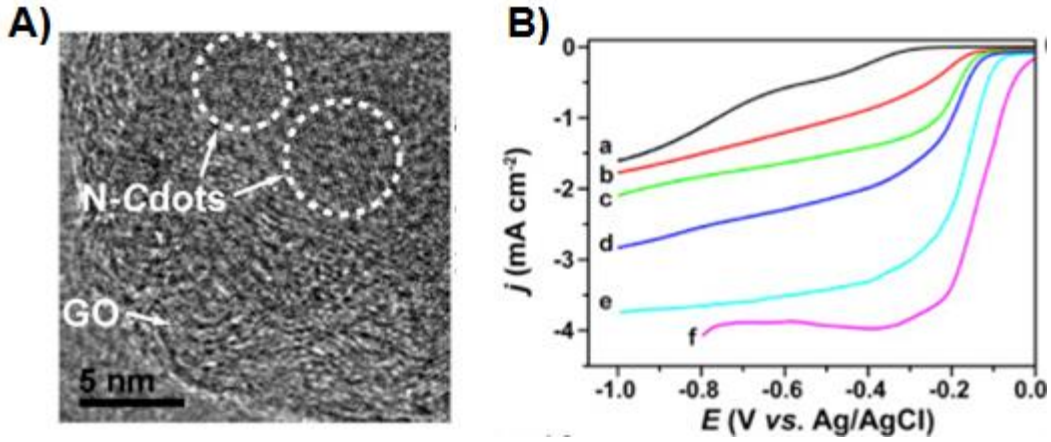

Figure 2-2 (A) The HRTEM images of the as-prepared N-Cdots/GO hybrid. (B) LSVs for the bare GCE (a), GO (b), N-Cdots (c), N-Cdots/GO mixture (d), N-Cdots/GO hybrid (e), and Pt/C (f) at 1000 rpm in O2-saturated 0.1M KOH solution at a rotating rate of 1000 rpm.[116]

2.2 Assembly of carbon nanostructures and biomass-derived carbon materials using hydrothermal processes

Apart from acting as catalytic component itself, graphene and CNTs can also be used as an effective carrier for other active components. The hydrothermal process hereby plays a role in promoting the assembly of the carbon nanostructures instead of hydrothermal carbonization process. Fei and co-workers in 2014 synthesized GQD/graphene hybrid nanoplatelets with B, N co dopant. The GQD was prepared by oxidizing anthracite coal in acid. The hydrothermal process promotes the self-assembly of GQD on graphene substrate, while B, N was doped by followed annealing process. The doping amount can be controlled by adjusting the annealing duration. The optimized hybrids demonstrated a remarkable ORR activity with ~15 mV more positive onset potential and similar limiting current density compared with commercial Pt-C.[117] Hu and co-workers produced N doped carbon dots decorated on graphene (N-CDs/G) via hydrothermal treatment in the year 2015. The N-CDs were obtained by electrochemical etching of coal-based rods in an

electrolyte which contained ammonia, then the N-CDs were combined with GO via hydrothermal process to produce the N-CDs/G hybrid. The as-prepared N-CDs/G hybrids showed comparable activity and better stability in comparison to the commercial Pt-C catalyst in alkaline electrolyte (**Figure 2-3**).[118] The hydrothermal process promoted the

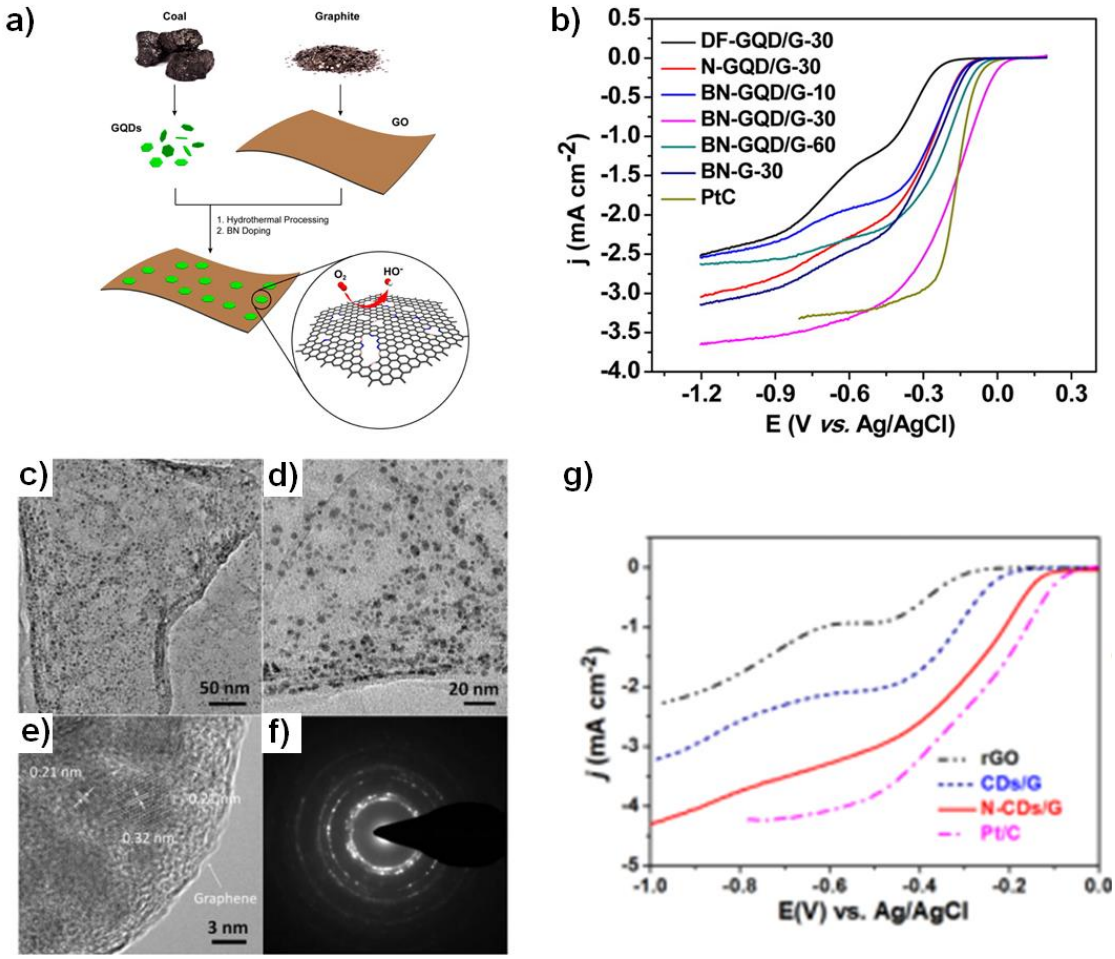

Figure 2-3 (a) Illustration of the preparation procedure for the BN-GQD/G nanocomposite. (b) RDE linear sweep voltammograms of ORR on DF-GQD/G-30, N-GQD/G-30, BN-GQD/G-10, BN-GQD/G-30, BN-GQD/G-60, BN-G-30, and Pt/C at a rotating speed of 900 rpm and scan rate of 5 mV s^{-1} [117] (c-e)TEM and HRTEM images of N-CDs/G hybrid. (f) SAED pattern of the N-CD2/G hybrid. (g) RDE voltammograms of rGO electrode, CDs/G electrode, N-CDs/G electrode, and Pt/C electrode in an O_2-saturated 0.1 M KOH solution at a rotation rate of 1600 rpm. Scan rate: 10 mV s^{-1}.[118]

self-assembly of GQD on the surface of GO via interactions between the hydroxyl and carbonyl functional groups of GO and GQDs, leading to the formation of GQD/G hybrid nanoplatelets. The graphene sheets not only serve as 2D platforms to facilitate the uniform distribution of GQDs on the 2D substrate, but also improve the electron transfer to interconnect the GQDs via the high electrical conductivity. Meanwhile, the porous scaffold of the as-prepared GQD/G nanosheets enhanced the facile mass transfer such as electrolyte and electro-reactants/products. The GQD with rich exposed edges and oxygen containing functional groups, on the other hand, allows for easy incorporation of dopants as potential active sites for the ORR reaction.

2.3 Hydrothermal assembly of other carbon nanostructures

Chen and co-workers in 2013 reported a N doped graphene/CNT composite prepared by HTC process of GO, oxidized CNTs and ammonia as nitrogen precursor at 180 °C for 12 hours (**Figure 2-4**).[119] The N content of graphene sheets and CNTs was 3.2 at% and 1.3 at%, respectively, according to EDX analysis of TEM. The as-obtained nitrogen doped graphene/carbon nanotube nanocomposite (NG-NCNT) showed a higher catalytic activity than both nitrogen doped graphene (NG) and nitrogen doped carbon nanotube nanocomposite (NCNT), which demonstrated a synergistic effect of graphene and CNTs. The authors attributed this synergistic effect to: (i) the insertion of 1-dimensional CNTs between graphene sheets, thus prevent the graphene sheets from restacking and increasing the exposed active sites, (ii) the 3D interpenetrated network structure promoted electron and mass transfer. Jiang and co-workers in 2014 further developed amine functionalized hole graphene (AFHG), by a subsequent etching in the presence of KOH to produce holes

on graphene flakes. The large number of holes in the graphene sheet gave more active edge N atoms and enhanced the ORR catalytic activity.[12] In fact, chemical etching using KOH, H_2O_2, etc. has been widely employed to produce holy graphene nanosheets either during or after the HTC process, as an effective method to promote the content of pyridinic N and other edge-derived active sites.[12, 120, 121]

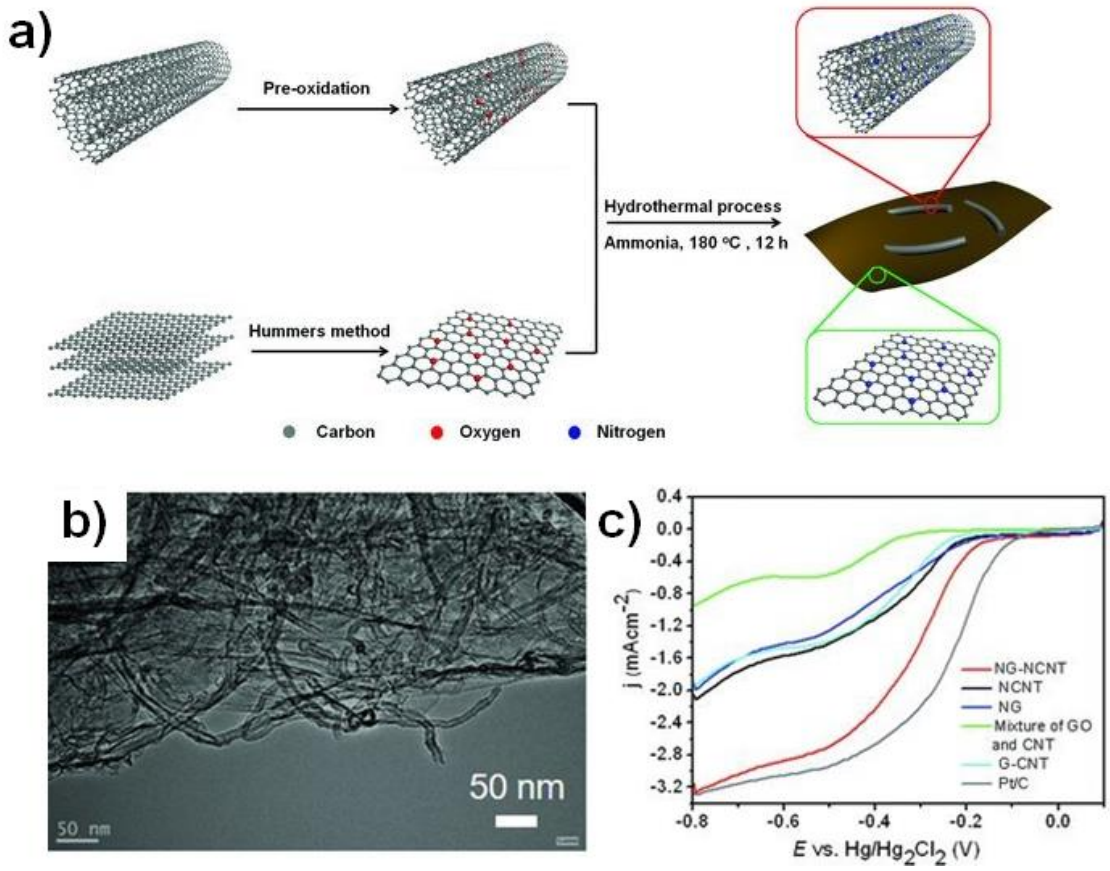

Figure 2-4 (a) Schematic illustration of the preparation of the NG-NCNT nanocomposites (blue balls, N; red balls, O; gray balls, C). (b) STEM image of the typical NG-NCNT nanocomposite (c) RDE voltammograms in O_2-saturated 0.1 M KOH solution at room temperature (rotation speed 1600 rpm, sweep rate 20 mV s^{-1}) for the NG-NCNT, NCNT, NG, G-CNT, Pt/C and directly mixed product of GO and OCNT. [119]

Ensafi and co-workers in 2016 produced pyridine-functionalized N graphene via HTC treatment of NH_4OH aqueous with GO suspension.[122] Amino-functionalized graphene

(AG) was synthesized by Yanglong's group via a HTC process of graphite oxide in the presence of ammonia solution (**Figure 2-5**a). They have demonstrated the important contribution of the amino group by eliminating the amino group by diazotization and hydrolysis, and demonstrated the superiority of solution-phase synthesis in the design and synthesis of N containing electrocatalyst. They have also studied the role of various nitrogen species via adjusting the annealing temperature following the HTC process (**Figure 2-5**b-d). The results showed that the onset potential and electron transfer number of the ORR process were determined by graphitic and amino N, while the improved ORR saturated current density resulted from the total amount of graphitic and pyridinic N.[123]

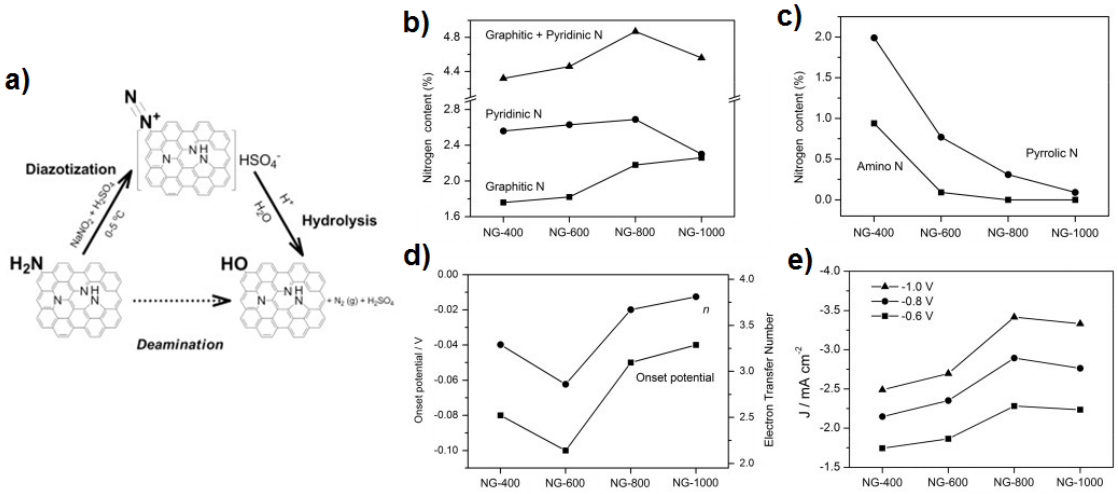

Figure 2-5 (a) Schematic illustration of deamination process for the preparation of deaminated NG: diazotization and hydrolysis. The content of (b) pyridinic N, graphitic N, (c) pyrrolic N, and amino N in annealed NG samples. The change in (d) the onset potential, electron transfer number, and (e) oxygen reduction current density at different potentials of annealed NG electrodes. [123]

Chen and co-workers in 2014 produced sulfurized graphene nanosheets via a low temperature process. The S-RGO-180 showed a close onset potential and an even higher saturated current density than commercial Pt-C, demonstrating more positive onset-

potential and larger current density compared to the samples without S doping. The Na_2S used in this work not only acts as S resource but also as a reductant to reduce GO into rGO. The authors believed that the abundant open edges and defects in graphitic frame works introduced by S doping was the main reason for the improved ORR performance.[81]

Heteroatom co-doping strategies are also widely applied into graphene HTC assembly of carbon nanostructures/hydrothermal carbon composites. For example, Su and co-workers in 2013 produced N, S co doped 3D graphene frameworks via a one-pot HTC treatment using NH_4SCN as N, S dual-containing precursor. The NH_4SCN decomposed into highly reactive N/S-rich species such as NH_3, H_2S, CS_2, etc. to react with the defective sites and oxygen functionalities on GO substrate. GO at the same time was reduced to rGO and assembled into 3D graphene frames during the HTC process. The as-obtained sample contains 12.3 wt% and 18.4 wt% of N, S, respectively. It showed a four-electron transfer pathway, comparable kinetic-limiting current density, better stability and tolerance to methanol compared with commercial Pt-C.[124] Moreover, B, N co doped graphene has also been developed as an effective ORR catalyst. The synergistic effect between B and N resulted in comparable saturated current density, better durability and methanol tolerance compared with commercial carbon. Those B, N co doped graphene is normally prepared combining HTC treatment to dope N, followed by annealing process to further dope B into the graphene matrix.[125-127]

2.4 General discussion and comparison

Detailed information of the typical samples discussed above are shown/listed in **Figure 2-6**/Table 2-1 For the low temperature HTC-synthesized samples, the addition of

graphene leads to a more positive onset potential, higher limiting current density, as well as improves the electron transfer number and decreases H_2O_2 yield especially at high over potential.[102, 116, 118] This is because the graphene structure promoted the electron transfer during the ORR reaction. The performance of the as-prepared carbon-carbon composites distinctly varies with different ratio of precursors, which leads to a different assembly of carbon matrix and distribution of active sites.[102] The addition of small amounts of graphene could lead to remarkable changes/improvements in morphology, physical and chemical properties, as well as electrochemical performance.

Among different formats of graphene materials, GO is the main option as the graphene precursor for HTC assembled carbon-carbon nanocomposites (Figure 2-6). This is because the rich edges, topological defects and oxygen contained functional groups on the panel structure of GO possess abundant free electrons, which favours the hybridization of graphene with HTC precursors.[128, 129] During the hydrothermal process, the GO is converted into rGO showing a higher electrical conductivity, while biomass and other precursors with heteroatom resources are hydrothermally carbonized into heteroatom doped carbon. However, because of the high O/C ratio, the electrical conductivity of HTC-derived rGO is not as high as other formats of graphene materials (eg. CNTs, thermally reduced graphene, etc), which limits the further improvement of the catalytic activity of the composites. On this consideration, addition of reducing agents (citric acid, etc) would be expected to promote the removal of the oxygen containing functional groups, thus further promoting the electrical conductivity of the composites. High temperature annealing has been applied to further improve the electrical conductivity of carbon matrix, this treatment improves the catalytic activity to some

extend but is still controversial because this method causes dramatic loss of heteroatom derived active sites under high temperatures.[102, 115, 117]

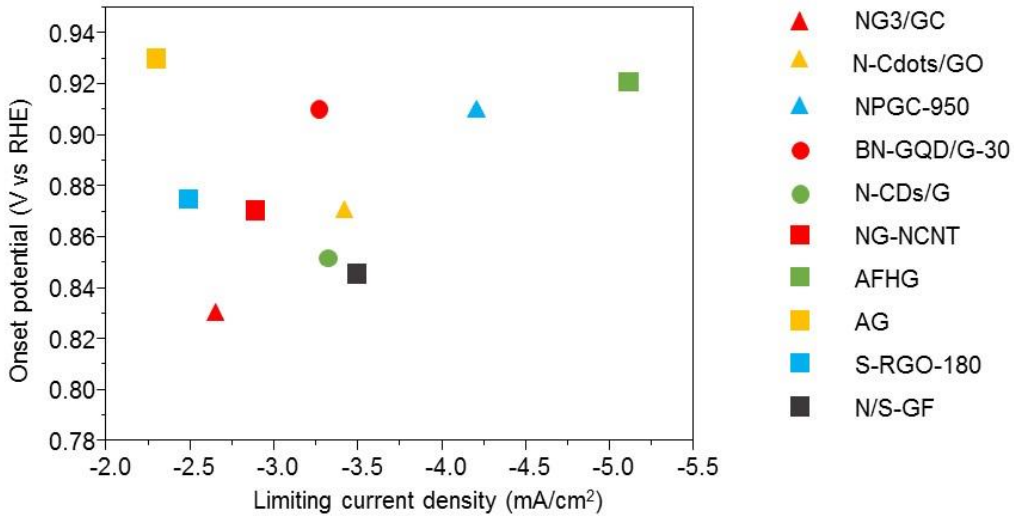

Figure 2-6 Graphical overview of onset potential and limiting current density for the best performing sample of each reference presented in chapter 3, taken from Table 2.

The assembly of as-prepared nanostructures, for example, carbon quantum dots (CQDs), on graphene and CNTs represent another promising technique for electrocatalysis. The CQDs derived from biomass precursors usually possess a high N content and a stable carbonaceous structure, meanwhile the superior conductivity of graphene in the composites compensates for the poor electrical conductivity of quantum dots and thus further facilitates the electron transfer.[128, 129] Overall, hybridization of N doped graphene/CNT composites is regarded as an effective strategy to produce electrocatalysts with 3-D structure, this structure results in improved mass and electron transfer, thus leads to superior catalytic activity.[119, 130, 131] Another limitation is that almost all the catalysts discussed were evaluated in alkaline electrolyte. An efficient HTC catalyst for ORR in acid media where a PEM Fuel Cell works has been seldom explored.

Table 2-1 Summary of best performing sample from each presented reference in **Figure 2-6**, all potentials mentioned are vs RHE**.**

Ref	Icon in Figure 2-6	Main precursor	HTC conditions	Pyrolysis temperature/ Activation	Onset potential of catalyst (V)	Onset potential of Pt standard (V)	Limiting current of catalyst at 0.6 V	Limiting current of Pt at -0.6 V	Electron transfer number	Stability (current remaining)	Dopants	Name
[101]	▲	Urea+GO	170 ºC, 12 h	–	0.83* (800 rpm)	0.02*	-2.65* (800 rpm)	-3.3* (800 rpm)	~3	–	N	NG3/GC
[116]	▲	Citric acid, urea, GO	200 ºC, 12 h	–	0.87	00.81 *	-3.42	-4.08	3.2	–	N	N-Cdots/GO
[132]	▲	Glucose, GO, EDA	180 ºC, 12 h	600 ℃	0.91	0.93	-4.2	-4.8	~3.75*	82% after 21600 s	N	NPGC-950
[133]	●	Coal, GO	180 ºC, 14 h	1000 ℃ for 0.5 h under Ar/NH_3, boric acid	~0.91	~0.91	-3.25*	-3.3*	3.93	73% after 20000 s	B,N	BN-GQD/G-30
[134]	●	Coal, GO, ammonia	180 ºC, 12 h	–	~0.85*	~0.88V*	-3.3*	-4.2*	3.6-4.0	90.6% after 20000s	N	N-CDs/G
[135]	■	Ammonia, GO, CNT	180 ℃ for 12 h	–	0.87	0.94V	-2.9*	-3.05*	3.7	88% After 8000 cycle	N	NG-NCNT
[136]	■	Ammonium hydroxide, GO	180 ℃ for 12 h	–	0.92	0.96V	-5.08 (at-0.8V)	-4.76 (at-0.8V)	3.6-4.0	> 93% After 36000s	N	AFHG
[123]	■	Ammonia, GO	200 ℃ for 12 h	–	0.93	0.96V	-2.3	-3.6	3.4-4.0	82%* after 20000s	N	AG
[137]	■	Na_2S, GO	180 ℃ for 6 h	–	0.875	0.895	-2.5	-2.8	3.8	96.3% after 10000s	S	S-RGO-180
[124]	■	NH_4SCN, GO	180 ℃ for 6 h	–	0.845*	0.915*	-3.5* (at 0.165V)	-4* (at 0.165V)	~3*	75.2% after 20000s	N, S	N/S-GF

* Values estimated from LSV graphs (unless otherwise noted at 1600rpm);
/ No information given
Potentials were converted as follows:
$E_{RHE} = E_{Ag/AgCl} + E^0_{Ag/AgCl} + 0.0591 \times pH$; $E_{RHE} = E_{Hg/HgO} + E^0_{Hg/HgO} + 0.0591 \times pH$

2.5 Summary and Conclusions

Overall, it has been demonstrated that hydrothermal carbonization is a powerful process to convert biomass into useful carbon materials as well as to create promising carbon-carbon hybrid materials which can be used as electrocatalysts for the oxygen reduction reaction in fuel cells. Hydrothermal carbonization can be effectively used to achieve the hybridization of graphene-based carbon-carbon nanocomposites. The graphene and CNTs in the composites usually act as a conductive substrate and sometimes also as a template to direct the pyrolysis process during the HTC. Moreover, due to easy aggregation of graphene nanosheets, the introduction of biomass derived HTC nanocarbon structures between the layers is an effective strategy to avoid the nanosheets from aggregating, which helps maintain its superior electrochemical properties. Metal-free carbon-carbon nanocomposites synthesized via HTC demonstrated comparable onset potential (more positive than ~-0.125V vs AgAgCl-sat.) and limiting current density (~3-5 mA cm^{-2}) with commercial platinum standards, and exhibited better long term stability (current retention higher than 70% after 10000 s of test) and methanol tolerance, which proves their promising potential to become an alternative electrocatalysts to commercial Pt-C.

3 Literature review II: Triple-phase boundary/surface optimization to improve oxygen reduction reaction of electrocatalysts

3.1 Key issues to be addressed in the TPB microenvironment.

Surface enriched active sites play a major role in deciding the ORR efficiency by decreasing the energy barrier during the oxygen reduction process. Moreover, wettability and oxygen affinity play decisive roles in the mass transfer and also largely determine the TPB interface reaction on the catalyst surface by improving the utilization of the active sites.[44] Indeed, the engineering of the interfacial chemistry between the active (reactant) components and the catalyst surface can induce strong synergistic effects for accelerated and stable electrocatalysis (**Figure 3-1**). The influence and strategies focused on the optimisation of the above issues will be addressed in following sections.

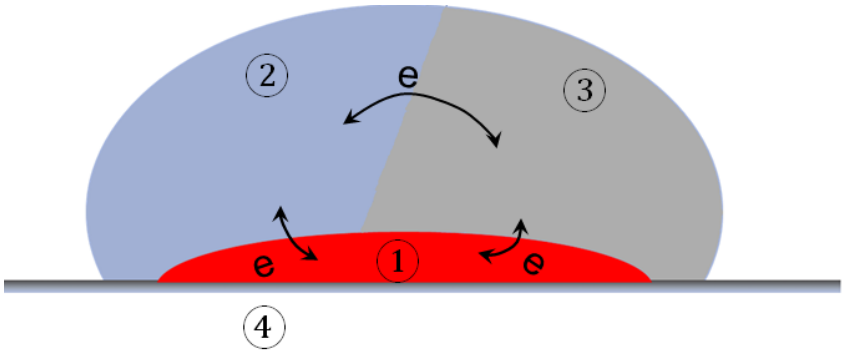

Figure 3-1 A scheme illustrating triple phase boundary, composed by (1) active sites, (2) aqueous electrolyte and (3) oxygen, interacted/connected by electron conductivity between different phases. (4) illustrates the carbon matrix of the electrocatalyst.

3.1.1 Surface enriched active sites

Novel physicochemical properties for nanocarbon catalysts can be largely tuned by surface atomic engineering (e.g. heteroatom-doping). On one hand, the heteroatom constructed functional groups (e.g. oxygen functional groups) have an important influence on the interfacial properties such as wettability and aerophilicity, which will be discussed later. On the other hand, the surface-active sites introduced by heteroatom doping with one or more elements of noticeably different electronegativities/size in comparison with carbon atom can largely tailor the electronic structures of the catalyst, which results in increased electrocatalytic activity through enhanced O_2 adsorption/dissociation. Instead of underlining the progress in the synthesis and reaction mechanisms involved in carbon electrocatalysis and the role of the active sites, this work will focus on reviewing various existing strategies for the surface engineering of carbon electrocatalysts.

3.1.2 Interfacial mass transfer: wettability and oxygen affinity

Wettability

Wettability is the ability of the electrolyte to maintain contact with the solid electrocatalyst surface.[138] Research on either "superhydrophilic" or "superhyrophobic" electrodes have been reported. Traditionally, a hydrophobic electrode surface represented by polytetrafluoroethylene (PTFE) modified active carbon was pursued. The PTFE modified electrode surfaces facilitate the gas diffusion on the electrode, the removal of the water produced at the electrode surface, maximizing and stabilizing the liquid/gas/solid triple-phase interface and therefore promoting the ORR reaction.[139] PTFE,

fluorinated ethylene propylene (FEP), and polyvinylidene fluoride (PVDF) are commonly used to plant on active catalyst and provide a hydrophobic surface.[140] Recently, some researchers claim that an enhanced hydrophilic surface can facilitate electrode wetting by the electrolyte into the micro/nanoscale pores, and this can enable more oxygen contact with the catalytic active sites, and therefore it is very important to investigate the wetting behaviour of solid surfaces. Considering the vast majority of carbon based materials are hydrophobic after the high-temperature treatment process, the intrinsic hydrophobicity of those carbon-based materials hinders aqueous solutions from entering the internal micropores of the nanostructure, preventing sufficient access and contact area between the electrode internal micropore surface and electrolyte which is necessary in an ORR process.[141, 142] The hydrophilic micropore surface contributes to the catalytic activity in two ways. Firstly, it facilitates the micro-pore walls to thoroughly interact with the aqueous solution with active transitional metal species, which can benefit a high facial loading of metal ion based active sites without random aggregation, resulting in high efficient metal-doped catalyst.[143] Secondly, a hydrophilic surface on a nanostructured electrode may also facilitate the transport of protons/electrons and electrolyte-dissolved O_2 towards the internal-micropore located at the electrochemically active sites centre, improving the utilization of active sites, and resulting in improved catalytic efficiency.[29, 144-146]

The superhydrophilicity of the carbon surface can originate from the surface roughness and hydrophilic functional groups on the surface. It can also result from the surface topography such as defects and edges on the carbon matrix.[46] Systematic studies and comparisons between the hydrophobic and hydrophilic are still rare. Wang P. et al.

reported a rational design of the surface texture of the hydrophobic electrode to control the surface wettability. They discovered that the neither super-hydrophobic nor super-hydrophilic surfaces alone are beneficial for the highly efficient ORR reaction. Sufficient surface wettability is critical for maximizing liquid/gas/solid triple-phase interface, and the unbalanced affinity to the aqueous would diminish the triple-phase interface and decrease the ORR reaction efficiency.[139]

Oxygen affinity

As a gas consuming reaction, the ORR electrocatalyst requires a gas diffusion pathway to continuously supply the oxygen reactant to the active centre. The supply of oxygen to the internal pore structure is limited by its low solubility in the electrolyte. It has been proven that the O_2 bubbles exert a significant influence at a high overpotential where the reaction is mostly limited by mass diffusion and transfer.[147] A higher oxygen concentration at catalyst surface improves the interaction of gas reactant with the surface active centre, and thus promotes the ORR reaction. Improving the aerophilic behaviour at the catalyst's surface has been achieved via improving the surface roughness.[148] For example, nanoarray electrodes were reported to demonstrate superaerophilic properties in aqueous electrolyte.[147] The influence of different surface roughness on the bubble behaviour is still arguable since the hierarchical structures that compose the rough surface are prone to degrade during long-term cycling, and therefore lead to descending catalytic activity.[149] This surface strategy has been widely applied to modify the aerophilicity of the catalyst surface via tuning the gas bubbles.

The interfacial modification of catalyst surface by coating a layer of aerophilic media is another efficient way to facilitate oxygen diffusion in the electrochemical process. For example, a series of fluorinated organic liquids have been reported to possess superior oxygen dissolvability.[150] Yet the application of those organic liquids on the carbon based electrocatalyst is still rare. Even though the facilitation of the oxygen diffusion is highly desired for boosting the ORR activity especially at high overpotential, this field is still at its infancy and the research in this field is scattered.

Apart from the above factors, the electron/proton conductivity also plays a major role in ORR. The carbon matrix usually possesses good electronic conductivity. However, the electron transfer between different interfaces, for example, from electrolyte towards catalyst surface, is another key issue which determines the reactant transfer and hence the ionic conductivity needs to be improved as well.

3.2 Nanoengineering the catalyst surface for enhanced ORR

3.2.1 Surface heteroatom doping (SHD)

Advantages of surface heteroatom doping

Heteroatom doping has been proved to be an efficient strategy to improve ORR activity. In a typical synthesis of heteroatom-doped nanocarbon materials, precursors containing the desired heteroatoms along/within a carbon rich precursor are carbonized at high temperatures. This usually results in the heteroatom being distributed both on the surface and within the bulk of the carbon matrix, while those bulk dopants possess little

accessibility towards the reactant (e.g. electrolyte dissolved ions and molecules), and therefore have a minor effect on the overall catalytic activity.[44, 151]

Interfacial engineering of heteroatom doping to create surface-enriched active sites is an efficient method to improve the ORR activity. The active sites formed on the catalyst surface are in direct contact with the three-phrase reactants such as the electrolyte, the oxygen bubbles and the catalyst's active sites.

Surface engineering strategies on active sites have shed light on the origin of electrocatalytic activity improvement. For example, Jiang W. et, al. has investigated the origin of Fe-based active sites (**Figure 3-2**a).[57] Highly active Fe-N-C ORR catalysts (Fe@C-FeNC) which contain graphene-encapsulated Fe/Fe_3C (Fe@C) nanocrystals and Fe-N_x configurations, were prepared using a hydrothermal method. CNTs performed as electron conductive substrate, while glucose, melamine and iron salt were applied to form Fe-N derived active centres on the CNTs surface. The composition of the catalysts was tuned by altering ratio of the precursors. The role of Fe/Fe_3C nanocrystals and Fe-N_x coordination was thereby studied in detail. The results demonstrate that the existence of Fe@C nanoparticles promote the activity of the neighbouring Fe-N_x, whereas the higher content of Fe-N_x sites in the presence of Fe@C nanoparticles leads to the higher ORR activity (**Figure 3-2**b). Several reviews on the synthesis, types and mechanisms of the active sites exist in the literature. [44, 151]

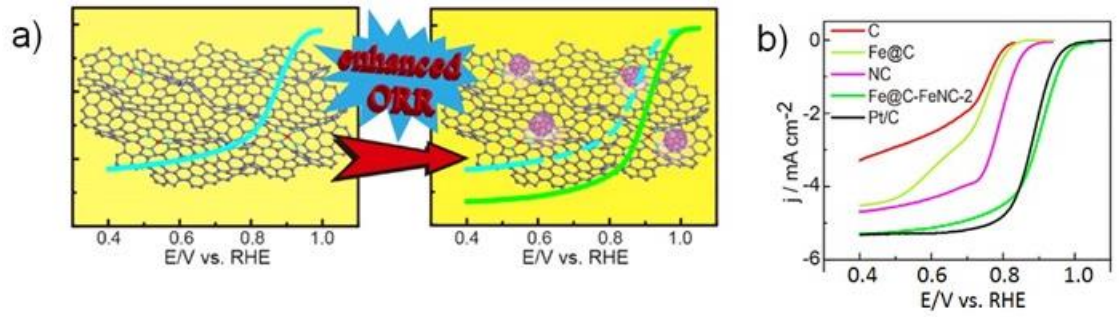

Figure 3-2 (a) Scheme illustration of the surface atom doping on carbon matrix. (b) Steady-state ORR polarization curves obtained in 0.1 M KOH, with the mass loading of 700 μg/cm^2. The curves compared the catalytic activity of carbon-based electrocatalysts with different types of Fe, N derived active sites.[57]

Another main advantage of heteroatom doping is the possibility to tune the surface wettability/hydrophilicity which is another key factor in ORR. N, O contained functional groups with hydrogen bonds strengthen the interaction between catalysts and aqueous electrolytes, and therefore facilitate the in-depth wetting by the electrolyte allowing easy penetration into the nanostructure.[152] Hao G. et. al. succeeded in tuning the surface properties of carbon-based materials, ranging from an ultra-hydrophilic carbon network to an ultra-hydrophobic carbon black.[153] A group of ultra-hydrophilic Fe/N, Fe/Cu/N and Cu/N doped carbon network with different ratios of each dopant was synthesized via an impregnation method followed by subsequent pyrolysis and acid washing treatment. Hydrophobic non-precious electrocatalysts were prepared in parallel under the same principle, using modification with N-containing polymers and $FeCl_3$, while the substrate was based on highly hydrophobic carbon black. The hydrophilicity/hydrophobicity property of the as-produced catalysts was quantified by water adsorption isotherms and water contact angle. The Fe, N content, the surface area and surface hydrophilicity were correlated with mass activity (**Figure 3-3**a). It was shown that an improved wettability

promotes the accessibility of electrolyte to the active sites centres, thus improving the utility of the active sites. The impregnation using Fe/Cu precursors to introduce Fe/Cu based active sites in the porous nanocarbon matrix, in combination with pyrolysis applied

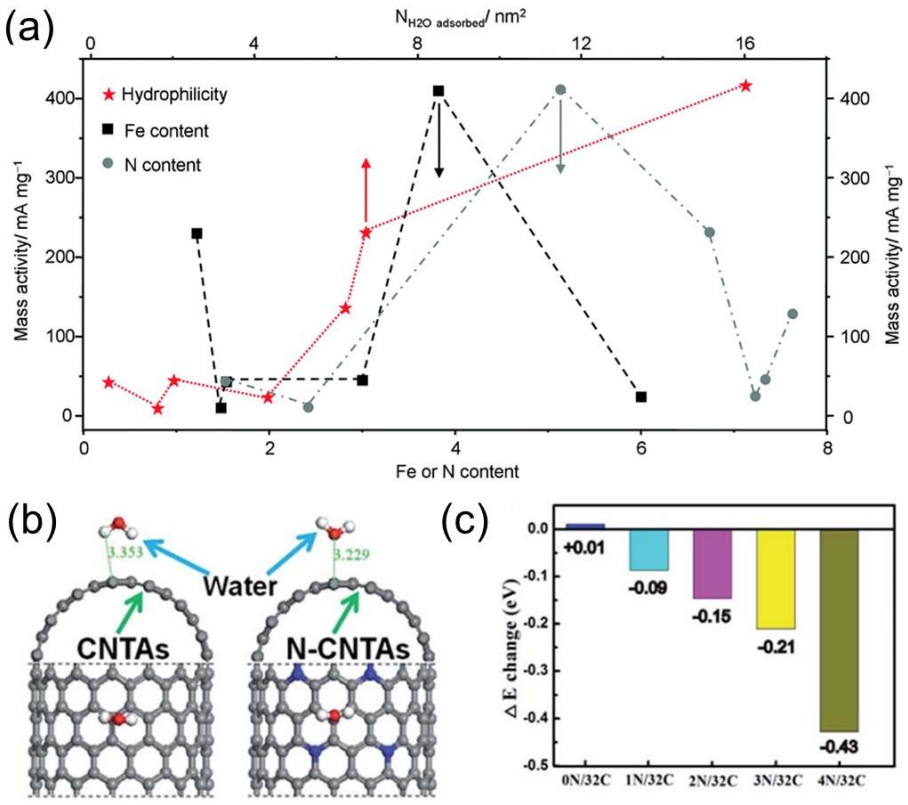

Figure 3-3 (a) Structure–performance comparison including surface hydrophilicity, nitrogen content (atomic%, by XPS) and Fe content (wt%, by ICP) with mass activity in ORR electrocatalysis under identical conditions.[154] (b) Structure diagram for the first principles calculation of the interaction of water and CNTAs or N-CNTAs. Grey spheres stand for C atoms, red for O, white for H and blue for nitrogen. (c) The binding energy of water and CNTAs with N doping degrees: 0.00, 3.13, 6.25, 9.38 and 12.5.[155]

in this work provides an effective method to control the surface parameters of carbon catalyst without dramatically changing the carbon matrix. The improved wettability by N-doping plays a dual role in ORR reaction. On one hand, the N-centre improves the hydrophilicity of the carbon matrix and therefore promote the deep wettability of the

carbon matrix. On the other hand, this improvement in hydrophilicity facilitates the homogeneous distribution of transitional metals on nanocarbon surface and therefore further benefiting the enrichment of active centres.

Sun X.'s group regulated the wettability of a 3D hierarchical CNTAs/graphene composites by changing the amount of the doped nitrogen in the CNTs during the CVD process.[155] First-principles theory was conducted to examine the interaction between water molecules and CNTs/N-doped CNTs(N-CNTs) (**Figure 3-3**b, c), and the result indicated that the interaction between water molecules and N-CNTs increased with increasing the N-content, whilst there was no attraction between water molecules and CNTs without N-doping. This discovery is consistent with the experimental results: the enhanced wettability of CNT surface facilitates the dispersion and uniform anchoring of CoO_4 nanoparticles, thereby resulting in as-obtained Co_3O_4/N-CNTAs nanocomposites showing a comparable ORR performance with commercial Pt-C. The improvement of hydrophilicity of catalysts surface facilitates a high accessibility of electrolytes into the micro/nano-pore structure, which promote the mass transfer by enabling more reactants (oxygen, electrons/protons) and ensuring a good contact between the catalyst and electrolyte, thus improving the active sites' utility. The improvement of hydrophilicity also facilitates the dispersion of solutions containing precursors for the active sites, especially transition metals, and avoids the aggregation of metal nanoparticles and therefore achieves superior active centres and boosts the ORR reaction. However, adjusting wettability also affects other factors. For example, the induction of heteroatoms, especially N and transitional metal (Fe, Co, etc), inevitably generates considerable positive charge density and high spin density that are preferable for the adsorption of O_2

to increase the ORR catalytic activity.[156, 157] Nevertheless, the amount of influence the hydrophilic surface exert on the improvement of catalyst activity remains to be clarified.

The methods to create surface heteroatom doping

Hydrothermal carbonization (HTC) is a powerful technique to control the assembly of surface active sites/heteroatoms with the carbon matrix. For example, graphene or CNTs can be combined with nitrogen containing biomass precursors such as chitosan or urea to create functionalized hybrid materials.[56, 57, 102] The assembly of electrochemically active elements on an electrically conductive carbon matrix is a very powerful and widely applied strategy to produce highly active electrocatalysts. The conductive carbon matrix facilitates the electron transfer through the catalyst, while the surface heteroatom dopant efficiently functions at the TPB interface. Graphene is a promising and widely applied option as a conductive substrate, it is one-atom thick layer of carbon material consisting of sp^2 hybridised carbon atoms which are densely packed into a two-dimensional (2-D) honey comb crystal lattice. This distinctive property makes graphene a very promising candidate to outperform other forms of carbon materials as electrically conductive substrates. The scalability and easy processability of the HTC technique is hereby remarkably favoured over other existing methods to produce carbon-carbon composites such as CVD and chemical or thermal exfoliation. The application of HTC to promote the assembly of heteroatoms onto carbon nanostructures can be extended to the assembly of carbon nanostructures, e.g. the assembly of CNT/graphene with CQDs, C_3N_4 QDs, etc.

Plasma treatment is another efficient method for catalyst's surface atomic modification for both heteroatom dopants and topological edges and defects. Plasma, as a fourth matter

state (ionized gas), is produced by activating the gas with sufficient energy, so that the electrons move independently with high energy.[158] The excited species such as radicals, electrons, and ions thereby intensely interact with the surfaces of carbon matrix, breaking the C-C bonds in the process. Active sites, as well as defects and edges, can be then obtained on the catalyst, playing a synergistic effect in boosting the ORR activity.[159] Plasma treatment is an efficient method for surface etching,[160] functional group incorporation,[161, 162] as well as rapid synthesis of transitional metal nitrides.[163] It is easily scalable, energetically economical, produces no chemical waste and a wide variety of functional groups can be tuned via different gases used, treatment time and pressure. Although it is still challenging to precisely manipulate the atomic structure, this strategy is still promising to account for the role of the edge-sites and defects, and thus for decoupling the contribution of the edges and defects on carbon atom by creating dopant-free ORR electrocatalysis,[24] recognizing the structure and mechanism of the edges and defected-derived sites.[29]

The role of plasma treatment plays a very similar role as that of heteroatom doping. It can be summarized as: i) the defects created improve the hydrophilicity of the carbon surface, therefore enhance ORR reaction. ii) the improvement in hydrophilicity further promotes a homogeneous incorporation of transitional metals within the carbon matrix, and therefore provides enriched surface-active sites. However, the conditions chosen for plasma treatment must be carefully considered, so that the created defects will not severely disturb the conductivity of carbon matrix in order to maintain a good electron transfer.

Other methods have also been applied for the surface modification of carbon catalyst. Those methods include but are not limited to: acid oxidation of nanostructures,[164, 165] chemical oxidization,[166] amine treatment,[165] and mechanochemical and sonochemical chemistry, etc. [167-170] Those methods might be limited by scalability and environmental concerns such as harsh synthesis conditions including extreme high temperature, strong acid/alkaline treatment, etc,.

3.2.2 Preventing the degradation of active site through the addition of a superficial carbon layer

Surface engineering methods induced sufficient exposure of active sites towards interface/TPB, and thus could largely promote the ORR reaction by sufficient accessibility towards active sites. However, the high exposure of active sites to the electrolyte increases the chances of poisoning of surface enriched active sites by toxic by-products. Thus, the active sites can easily degrade due to the by-products produced during the reaction or because of the leaching effect from harsh acid/alkaline electrolyte. It has been recently reported by Bao X.'s group that the catalytically active transition metal nanoparticles containing unsaturated metal sites or low valence state metals, encapsulated within the core-shell structure of carbon capsules, possess normal catalytic functions whilst being physically protected by its shell from harsh chemical environment (acid electrolyte, etc) in order to avoid leaching (**Figure 3-4**a-c).[59, 74, 75] The non-precious metal nanoparticles (Fe, Fe/Co alloy, etc) being encapsulated into the compartments of pea-pod like carbon nanotubes (CNT) are well shielded by the CNT walls against O_2, the acid environment, and the by-products which dramatically reduce the performance of the

catalyst in a PEMFC. This catalyst was even stable in the presence of CN^-, which can strongly coordinate Fe and poison the iron-based active sites for ORR. Meanwhile, such

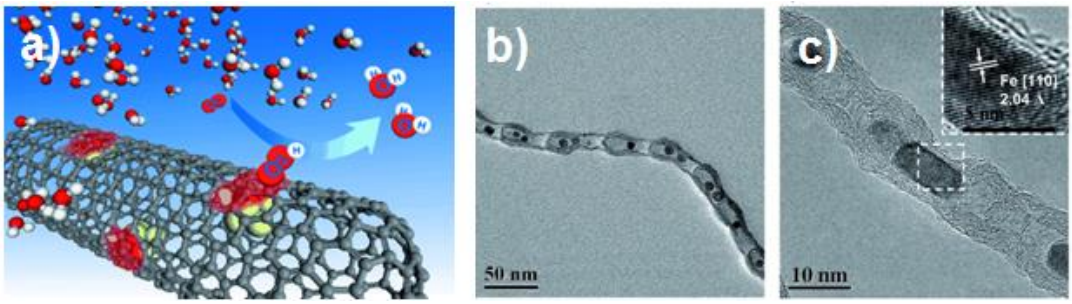

Figure 3-4 (a) A schematic representation of the ORR process at the surface of Fe_4@SWNT. The carbon, oxygen, hydrogen, and iron are presented by grey, red, white and yellow objects, respectively. (b)TEM image of Pod-Fe, (c) HRTEM image of Pod-Fe with the inset showing the [110] crystal plane of the Fe particle.[59]

completely encapsulated Fe nanoparticles within CNT compartment are active towards ORR, even without direct contact with electrolyte. The encapsulated Fe nanoparticles can interact with the CNT shell and affect the properties of the outer wall where O_2 is activated and reduced. Theoretical studies showed that the electron transfer from Fe nanoparticles to the CNTs lead to a decreased local work function on the CNT walls. Doping N into the carbon lattice can further reduce the local work function and therefore promote the ORR activity.[59] The decrease of carbon wall thickness is found to be beneficial in the dissociative adsorption of O_2 and thus in the ORR reaction in acid solution.[74] Similar conclusions have been drawn in different categories of carbon layer encased non-precious metal based electrocatalysts.[21, 171-173]

3.2.3 Polymer-modified gas diffusion layer

As previously introduced in section 3.1.1, the role of surface hydrophobicity and hydrophilicity has been a controversial topic. Although the hydrophilic surface greatly benefits the catalyst-electrolyte interactions, the mass transfer of oxygen is limited by the solubility of oxygen in the aqueous electrolyte, therefore some argue that a hydrophobic interface is desirable to promote the mass diffusion in the ORR reaction.[147]

Teflon-treated carbon fibre paper (TCFP) has been widely used to facilitate the gas diffusion process, because its highly hydrophobic surface and reasonable electron conductivity provides a three-phase contact point for oxygen, electrolyte and catalyst instead of being flooded by the electrolyte.[174] The TCFP facilitates a higher supply of oxygen compared with electrolyte-wetted catalyst surface by providing a higher diffusion rate due to its hydrophobic surface property. It was reported that a low percent of Teflon,also known as PTFE, in the gas diffusion layer, can promote the ORR activity, however further enhancement of PTFE percentage hindered the ORR activity due to limited electron conductivity.[175] Therefore, the improvement of gas diffusion whilst maintaining the electron transport is a critical and challenging issue. Sun X.'s group recently reported a Co, N co-doped carbon nanotube array (CoNCNT) electrode with superaerophilic surface and high electron conductivity.[147] CoCNT arrays were in-situ constructed on the carbon filter paper (CFP) substrate via a solvothermal method followed by pyrolysis treatment. Afterwards, the constructed electrode was modified by a uniform loading of PTFE particles on the CoNCNTs electrode matrix (**Figure 3-5**). The porous structure and PTFE coating layer synergistically constructed a "superhydrophilic" surface,

whereas the intimate connection of the CoNCNT with the CFP substrate ensured the high electron conductivity. The improved gas-adhesion behaviour was demonstrated to benefit the ORR performance by providing a stable current increase and a larger current density at the high overpotential region.

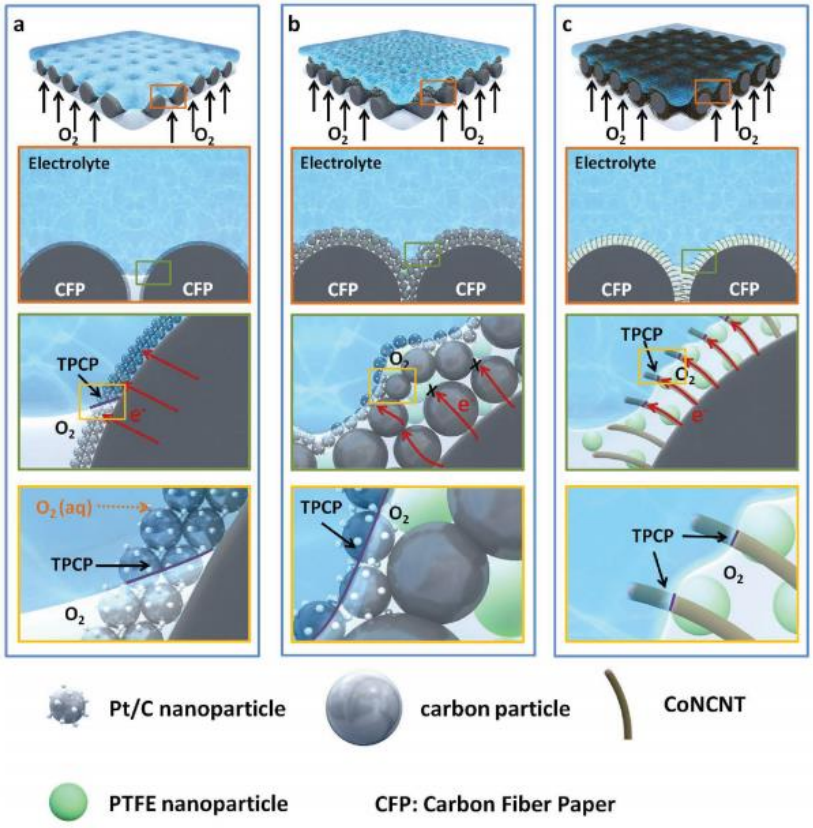

Figure 3-5 (a) Schematic illustration of commercial TCFP with Pt/C catalyst loading (Pt/C-TCFP) under electrolyte, the oxygen-diffusion process is blocked and thereby the interface cannot create enough TPCP for ORR; (b) structural scheme of the commercial air electrode with an additional MPL located between TCFP and Pt/C catalyst (Pt/C-MPL-TCFP), the oxygen-diffusion process is accelerated but the electron transport process is impeded by the thick MPL with insulating materials coating, resulting in inferior ORR performance; (c) schematic illustration of the "superaerophilic" structured electrode by direct growing CoNCNTs on CFP, both electron transport and oxygen-diffusion processes are accelerated, leading to a superior ORR performance. In the model in (a), most of the catalyst particles are immersed by the electrolyte and thus only touch the dissolved oxygen (denoted as "O_2 (aq)"); thereby, the ORR rate is very slow because the concentration is extremely low.[147]

3.2.4 Ionic Liquids modification

Ionic liquids (ILs) refers to liquids composed entirely of ions, which are fluid at around or below 373 K. It has been regarded as promising alternative solvents and electrolytes for electrochemistry, due to its intrinsic ionic conductivity, and high thermal, chemical and electrochemical stability.[176] Ionic liquids (IL) modifications have been reported as a chemical method to tune the oxygen affinity of the catalyst surface. In 2004, ILs with perfluorinated side chains have been reported by Luo et al. to possess a higher oxygen solubility compared with aqueous electrolytes.[150] In 2017, Walsh D.'s group investigated the synthesis of protic ionic liquids with high ion conductivity.[177] When applied as carbon-based electrocatalysts for ORR, the ionic liquid usually plays a role as carbon precursor, sacrificial template, or source of heteroatom-dopant. Yet many advantages of ionic liquids, such as large electrochemical window, good thermal stability, and solubility of a diverse range of organic and inorganic compounds, are rarely fully utilized in this field.[178] In the year 2010, ILs have been first applied to Pt based electrocatalyst and proved to contribute to the oxygen utility on active sites and promote the ORR reaction.[179-183] However the application of ionic liquid onto nanocarbon electrocatalysts is rarely reported.

In contrast to the bottom-up control of the electrocatalyst matrix, the surface modification on IL possesses several advantages: Firstly, the interaction of IL with the carbon surface via π-π conjunction catalyst matrix allows a delicate control of the catalyst surface property without complicated synthesis process. Secondly, the wide variety of anion and cation of ionic liquids provide great options to obtain different surface modifiers with

super flexible alternative chemical properties, such as different water solubility, oxygen affinity, etc. to balance and maximize the TPB. This strategy demonstrates a promising application to other interface reactions, especially in gas-involving electrocatalysis such as OER, CO_2 reduction or in organic electrolytes in metal-air batteries.

Different from the triple-phase control over the whole battery (fuel cell) devices, for example to replace the entire electrolyte with different polymer alternatives, the surface modification of carbon-based catalyst should be more competitive because only a small amount of polymer/ionic liquid is applied, which is more environmentally benign and economical. Moreover, the treatment on the nanostructure can be more targeted and hence more tuneable. The study of ionic liquid modified triple point interface to engineer the electrode nanostructure is a novel concept and is promising to be further studied in the future.

3.3 Conclusion and perspectives

In this chapter, some interfacial modification strategies at the catalyst surface are summarized, aiming at improving the ORR performance of non-precious metal nanocarbons.

These strategies work by improving the accessibility of the electrolytes towards high-efficient active sites, as well as to facilitate the mass transfer, especially proton and oxygen, to maximize the TPB where the ORR happens. These strategies are also powerful and actively applied to address important fundamental issues such as the recognition on configuration of typical active sites, and the validation of mechanisms via decoupling the main factors associated with ORR activity (i.e electronic conductivity, pore structure,

active sites, polarity, ionic conductivity) to understand their individual influence on the catalyst. These involve, for example, sandwich structures, core-shell structure, etc.

Doping heteroatoms at the surface of carbon catalysts can increase the distribution of functional groups at the nanopores' surface of the carbon matrix. These heteroatoms can control the surface wettability and the high accessibility of the electrolyte-dissolved reactants towards the active centres and thereby improve the utilisation of the active centres. However, the active sites highly exposed to the reaction environment are at risk of being deactivated by poisonous by-products, or being leached away by acid/alkaline electrolyte, so that the long-term stability of the electrocatalyst need to be carefully considered. Surface modification by a thin layer of protective carbon has been proved to avoid the active sites from being directly poisoned by the by-products during ORR reaction. However, although carbon-encapsulated iron particles have been reported to exhibit superior catalytic activity, this strategy has not yet been proved to be effective for other active centres, given that the accessibility of the active sites towards electrolyte and reactants is possibly hindered and activity degraded. Surface planting of secondary hydrophobic oxygenophilic layer such as PTFE is an effective strategy to facilitate TPB and protect active centres by improving oxygen affinity and meanwhile expelling the produced water and by-product. Yet the layer thickness needs to be carefully considered and balanced in order to guarantee the electron conductivity. Nanostructure construction, such as the porosity of this secondary layer may be a way to balance the electron conductivity and mass transfer.

From the authors' perspective, the ionic liquids are more promising in the application of facilitating the TPB of gas-involved reaction. Their protic and oxygenophilic properties facilitate the mass and proton transfer in the electrochemistry process. Moreover, although they are hydrophobic, they have a certain solubility of water, which greatly guarantees the balance of the TPB interfaces. The electrochemical stability of ILs and the flexible tunability of their anions and cations make them promising candidates in the application of TPB interface reactions.

4 Experimental section

4.1 Characterization methods

Scanning electron microscope (SEM): The SEM produces images by scanning a sample with a focused beam of electrons. The electrons interact with atoms in the sample and produce various signals (secondary electrons, backscattered electrons, and characteristic X-rays) that are collected by detectors to produce topography information of the samples. When an electron beam strikes the surface of the sample, it penetrates the sample to a depth of few micrometres depending on the acceleration voltage and the density of the sample. **Figure 4-1** demonstrated the schematic of a typical scanning electron microscope and imaging process.[184] In this thesis, an FEI Inspect-F scanning electron microscope is used to detect the morphologies and structures of the samples.

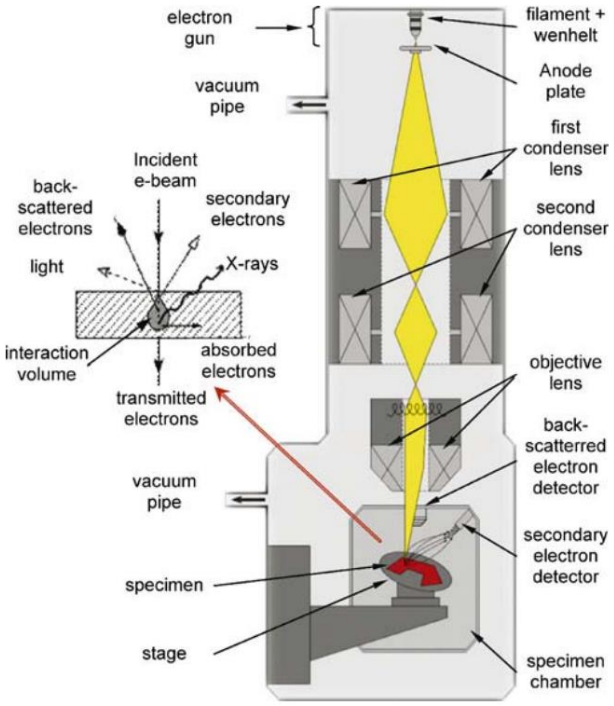

Figure 4-1 Schematic of a typical scanning electron microscope and imaging process[184]

Transmission Electron Microscopy (TEM): In a TEM technique, a beam of electrons is transmitted through an ultrathin sample or a suspension on a grid. The interaction of the electrons with the atoms in the sample gives information on the feature structures such as crystal structures, grain boundaries, etc. **Figure 4-2** demonstrates the schematic of a typical transmission electron microscope and imaging process. Moreover, high resolution TEM (HRTEM) can be used to analyse the qualities, shapes and sizes of quantum dots.

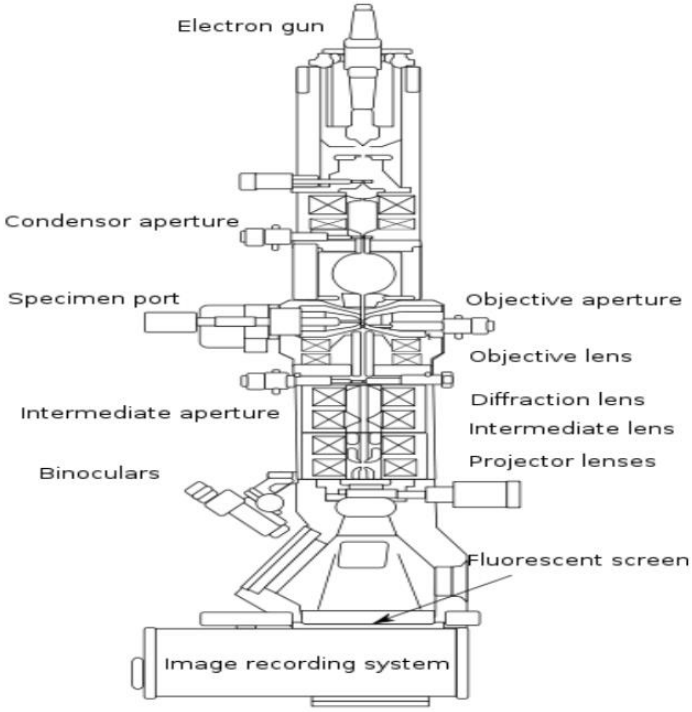

Figure 4-2 Schematic diagram of transmission electron microscopy[185]

Energy Dispersive X-ray Spectroscopy (EDS, EDX or XEDS): As an electron beam is focused on the sample in either a SEM or TEM, the produced X-rays are detected by an energy dispersive detector, which exhibits the signal as a spectrum versus X-ray energy. Those characteristic X-rays allow quantitative and qualitative identification of the

elements, which gives information on the elemental chemical composition in a sample with an atomic number (Z) > 3.

In this thesis, TEM and EDS were obtained on Transmission Electron Microscope (HRTEM, JEOL (JEM 2100-F)) (for samples in Chapter 6), and a JEM 2010 (JEOL Ltd., Tokyo, Japan) transmission electron microscope (TEM) (for samples in Chapter 5, 7). Energy dispersive spectroscopy (EDS) analysis was performed at the acceleration voltage of 120.0 kV using a JEM 2010 (JEOL Ltd., Tokyo, Japan) TEM equipped with an Oxford Instrument energy dispersive spectrometer.

Physical adsorption (N_2 adsorption): Physical adsorption is a powerful technique to measure the specific surface area of a porous sample. It is determined by calculating the amount of adsorbate gas on the surface of a sample. The physical adsorption depends on the van de Waals forces between the adsorbate gas molecules and the absorbent surface of the tested sample. The N_2 adsorption is conducted at the temperature of liquid nitrogen (77.4 K). The amount of gas adsorbed can be measured by a volumetric or continuous flow procedure. The specific surface area is calculated based on the Brunauer–Emmett–Teller (BET) theory and follows the below hypotheses:

(i) gas molecules physically adsorb on a solid in layers infinitely;

(ii) gas molecules only interact with adjacent layers;

(iii) the Langmuir theory can be applied to each layer.

The resulting BET equation is:

$$\frac{1}{V\left(\frac{P}{P_0}-1\right)} = \frac{C-1}{V_m C}\left(\frac{P}{P_0}\right) + \frac{1}{V_m C} \quad \text{Equation 4-1}$$

where V is the adsorbed volume of gas, P is the equilibrium gas pressure, P_0 is the saturation pressure of the adsorbate gas, C is the BET constant related to the enthalpy of adsorption of the adsorbate gas, V_m is the adsorbed volume of gas to produce an apparent monolayer on the sample surface, P is the equilibrium gas pressure, P_0 is the saturated pressure of the gas.

The N_2 adsorption-desorption isotherm in this work was measured at -196 ºC by the an Autosorb-IQ2-MP-C system (Quantachrome Instruments, USA) (for samples in Chapter 5), NOVA 4200 system (Quantachrome Instruments, USA) (for samples in Chapter 6), Autosorb-IQ system (Quantachrome Instruments, USA) (for samples in Chapter 7). The specific surface area was calculated by the multipoint Brunauer–Emmett–Teller (BET) method, and the pore-size distribution was calculated based on Quenched Solid Density Function Theory (QSDFT) using the adsorption branch. Water sorption isotherms were carried out at 20 ºC using a gravimetric water sorption analyser (Aquadyne DVS, Quantachrome Instruments). Before each sorption measurement, the samples were outgassed at 120 ºC overnight.

X-ray photo electron spectroscopy (XPS) is a widely used surface analysis technique to identify the elemental composition of surface of the materials. The fundamental process is based on the photoelectric effect. During the measurement, the sample surface is irradiated with X-rays in vacuum. As the X-ray photoelectron hits and transfers the energy to the core-level electron, it emits from its initial state. The kinetic energy and intensity of the emitted photoelectrons thereby give information on the concentrations of the elements present. The XPS gives surface elemental composition information in an

average depth of 5 nm. In this work, X-ray photoelectron spectroscopic data (XPS) was collected using a Thermo Scientific K-Alpha* instrument (Thermo Fisher Scientific, East Grinstead, UK) equipped with a monochromated aluminium K-alpha X-ray source. The charge compensation system on the instrument was used for the analysis, and the monatomic and gas cluster ion source (MAGCIS) was used in cluster mode for a necessary sample cleaning. The obtained spectrums were calibrated by setting the C1s peak at 284.6 eV. For Fe, the Fe2p peak was used for the assignment of binding states. Peak assignments were conducted by referring the values reported in literatures indicated in the results in Chapter 5-7. The (Full width at half maximum) FWHM was set to between 1.5 eV- 2.0 eV. The reproducibility of the XPS results can be found in Chapter 4.3. During the measurement, the XPS test scans at three different points in the material, where the average results are finally obtained and fitted for analysis. The **Figure 4-3** shows the independent spectra results of the three points, proving the data is reproducible.

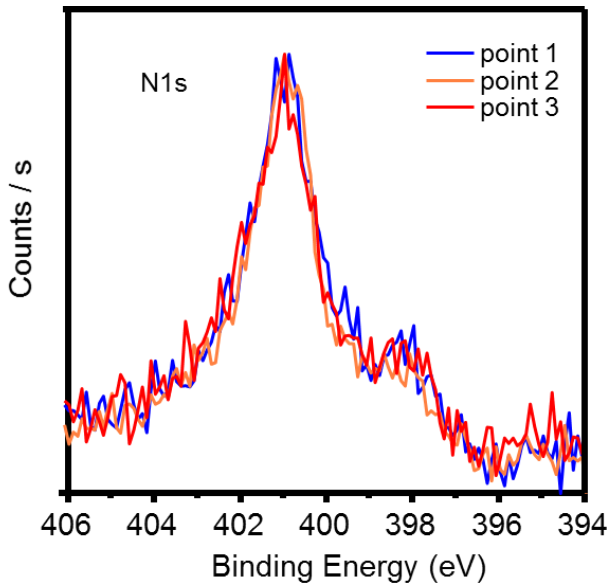

Figure 4-3 N1s spectra of NC-CNT-1000, the spectra were taken from three different points, demonstrated excellent reproducibility of the results.

X-ray powder diffraction (XRD) is a rapid analytical technique applied primarily for the phase identification of crystalline materials and provides information on unit cell dimensions. The fundamental working principle of XRD measurement is based on the constructive interference of monochromatic X-rays and the crystalline samples.[186, 187] In this work, X-Ray diffraction (XRD) was carried out using a Bruker D5000 with *Cu* Kα1 radiation. Scans were performed between 10 and 80 2-θ using a step size of 0.02 2-θ and a count time of 15 seconds per step. The samples were spun during data collection. Bruker 'EVA' software package along with the International Centre for Diffraction Data database were used to analyse the diffractions. XRD patterns were collected on a Siemens D5000 X-Ray powder diffractometer with Cu Kα radiation. The contact angle of electrocatalyst in this contribution was determined on Dataphysics OCA20.

Thermogravimetric analysis (TGA) provides thermal analysis of a sample, it provides information on various properties (thermal stability, oxidative stability, phase transitions, etc) by continuously recording the absolute amount and rate of mass change as a function of time or temperature. The TGA in this work was measured with TGA Q500.

Fourier Transform Infrared Spectroscopy (FTIR) uses infrared light to detect samples. It is widely applied for identifying chemical structure of organic, polymeric and inorganic materials. When the infrared radiation passes through a sample, some radiation is absorbed by the sample, while some is transmitted. The resulting signal at the detector represents the molecular "fingerprint" of the sample, therefore provides information of different chemical structures with unique "fingerprint". In this work, Fourier-transform infrared (FTIR) spectroscopy was measured on Tensor 27.

Nuclear Magnetic Resonance (NMR) spectroscopy is an analytical chemistry technique used in quality control. It is an effective research method for determining the molecular structure and purity of a sample. NMR can quantitatively analyse mixtures containing known compounds. The working principle of NMR is that many nuclei have spin and all nuclei are electrically charged, and an energy transfer is possible when an external magnetic field is applied. The energy transfer takes place at the wavelength which corresponds to the radio frequencies. In this work, ^{1}H NMR spectra were obtained on a Bruker Avance UltraShield AV400 or AV600 (400 MHz, 600 MHz). ^{1}H spectra were obtained in $CDCl_3$ and referenced to the residual solvent peak at 7.26 ppm and solvent peak at 77.2 ppm. Chemical shifts are quoted in parts per million (ppm) to 2 dp for ^{1}H NMR spectra. Spectral data are reported as follows: chemical shift, multiplicity (s = singlet, d = doublet, t = triplet, q = quartet).

4.2 Electrocatalyst fabrication

Chemicals:

Chitosan (CS, medium molecular weight), graphite flakes, acetic acid (HAc, ACS reagent) and all the other chemicals used in this work were purchased from Sigma (UK). Graphene oxide (GO) in this contribution was prepared via a modified Hummer's method.[188, 189] Electrically conductive graphene was offered by Carmery graphene marketing centre, Institute of Coal Chemistry, Chinese Academy of Science. 1-butyl-3-methylimidazolium bis(trifluoromethanesulfonyl) imide ($[C_4C_1im][NTf_2]$) and 1-Ethylimidazolium bis(trifluoromethylsulfonyl) imide ($[C_2im][NTf_2]$) were purchased from IoLiTec. Urea, and $Fe(NO_3)_3{\cdot}9H_2O$ were purchased from Sigma. The chemical

structure of these two IL has been demonstrated in **Figure 7-3**. KOH and $HClO_4$ were bought from VWR. Deionized water was applied for all the experiments.

Fabrication of electrocatalysts in Chapter 5:

The synthesis procedure included two steps: hydrothermal carbonization (HTC) and high temperature carbonation process. During the HTC, CS and GO of different mass ratios were dissolved in 2.0 % (v/v) acetic acid to achieve a homogeneous solution. The mixtures were then sealed into stainless steel autoclaves with a Teflon inlet and heated at 200 °C for 12 h under self-generated pressures of around 10 bars. After cooling to room temperature, the samples were then frozen at -20 °C, then freeze dried for 72 hours. The products obtained from HTC process are denominated as NC, NCG0.05, and NCG0.25, respectively. The number refers to the mass ratio of GO in the mixture of GO/CS. The as-obtained products were then annealed at 1000 °C under the N_2 flow for 2.0 h. The resultant samples were named as NC-1000, NCG0.05-1000, and NCG0.25-1000. Detailed composition of the precursors and products are listed in **Table 4-1**. Pure rGO was synthesized at the same condition for comparison.

Table 4-1 Detailed Composition of the precursors and products

Sample	**Composition (mass ratio)**	**Chitosan (mg mL^{-1})**	**GO (mg mL^{-1})**	**HAc (v/v)**
NC	Pure CS	60.0	0	2 %
NCG0.05	95 % CS + 5 % GO	60.0	3.0	2 %
NCG0.25	75 % CS + 25% GO	9.0	3.0	2 %
NC-1000	--*	60.0	0	2 %
NCG0.05-1000	--*	60.0	3.0	2 %
NCG0.25-1000	--*	9.0	3.0	2 %

* The composition of high-temperature annealed samples is determined by the HTC products.

Fabrication of electrocatalysts in Chapter 6:

The MWCNTs were synthesised using an aerosol-assisted chemical vapour deposition setup as described previously.[190-193] Briefly, the synthesis involved thermocatalytic pyrolysis of a 5 wt.% solution of ferrocene (purified by sublimation) in ethylbenzene (99%). An aerosol was created from this solution using a piezoelectric-ceramic-driven generator. At an Ar flow rate of 1000 sccm this aerosol is introduced into an 800 °C hot quartz reactor over a period of 15 min. The reactor was then cooled down to 300 °C and the MWCNT deposit was collected for further processing of the carbon-carbon composites.

The synthesis of the carbon-carbon composites included two steps a) hydrothermal carbonisation (HTC) and b) high-temperature carbonisation. 24 mg of MWCNTs were milled with 2 ml deionised H_2O for 15 min in order to separate the MWCNTs first. CS and the MWCNTs were then dispersed in 2.0 % v/v acetic acid with a mass ratio of 7.5:1, stirred for 1 h, and sonicated for another hour at room temperature in order to generate a homogeneous suspension. For the HTC process, the MWCNT/CS-in-water suspension was sealed in a stainless-steel autoclave vessel, heated to 200 °C, and kept for 12 h under a self-generated pressure of *ca.* 10 bar. After cooling to room temperature, the samples were filtered and washed with deionised water, then dried in a vacuum oven at 80 °C overnight. (For reference, the as-obtained NC-CNT composites obtained through the HTC process were denominated as NC-CNT-HTC). These HTC products were then annealed at 1000 °C under an N_2 flow of 2 LPM for 2.0 h. The resultant samples were named as NC-CNT-1000. For comparison, raw MWCNTs and chitosan were treated

following the same procedures described above and labelled CNT-HTC, CNT-1000, NC-HTC and NC-1000 respectively.

Fabrication of electrocatalysts in Chapter 7:

The synthesis of graphitic nanocarbon composites:

The nanocarbon electrocatalyst was synthesized *via* a hydrothermal process, followed by a high temperature carbonization treatment. Specifically, 1 g urea was first dissolved in 20 mL deionized water to form a homogeneous solution, then 100 mg of high conductivity graphene was added into this solution. After magnetically stirring for 30 min at room temperature, the mixture was then sealed into stainless steel autoclaves with a Teflon inlet and heated up to 180 ºC for 5.5 h under self-generated pressures of around 10 bars. After cooling to room temperature, the obtained product was then filtered and washed by deionized water several times. The sample was then frozen at -20 °C, followed by a freeze-drying process for 72 hours. The as-obtained powder was then annealed at 1000 °C in a flowing N_2 atmosphere for 2.0 h. The hydrothermal process promotes the self-assembly of urea and graphene, while the high temperature pyrolysis further improves the carbon backbone and converts the nitrogen source into a more favourable form of nitrogen-based active sites (pyridinic-N and quaternary-N). The resulting sample was named as GN. The Fe-containing electrocatalyst was synthesized following the same procedure with the addition of $Fe(NO_3)_3$. Specifically, 1 g urea and 505 mg $Fe(NO_3)_3 \cdot 9H_2O$ were dissolved in 20 mL deionized water to form a homogeneous solution, followed by the same procedure for GN. The resultant product was named as GNFe.

Surface modification of graphitic nanocarbon composites via ionic liquids:

8 mg of electrocatalyst (GN, GNFe) was mixed with 1400 µL H_2O and 528 µL ethanol, respectively. Then 1.1 µL of $[C_4C_1im][NTf_2]$ or $[C_2im][NTf_2]$, which was equivalent to 20 wt% of the catalyst, was carefully added into the solution. The mixture was then ultrasonicated for 10 min to homogeneously disperse the ionic liquids (ILs) into slurry. The mixture was then anchored on a shaker to shake for 60 hours to make the ILs fully interacted with the electrocatalysts. GN and GNFe without any addition of ILs was treated with same process for comparison. For morphology and surface chemistry characterization, the obtained slurry was then frozen in liquid nitrogen at -197 °C, followed by a freeze-drying process for 72 hours. The obtained samples were named as GN, GN-IL1, GN-IL2, GNFe, GNFe-IL1, GNFe-IL2, respectively. Herewith IL1 refers to $[C_4C_1im][NTf_2]$, IL2 refers to $[C_2im][NTf_2]$.

Preparation of amorphous nanocarbon composites:

The FeNC electrocatalyst was synthesized according to a previous report.[194] Briefly, silica particles with a hollow core and a mesoporous shell (SCMS) were synthesized as reported by Unger et al.[195] Afterwards, the SCMS particles were impregnated by the dropwise impregnation technique with a 2 M $FeCl_3$ ethanol solution (around 0.27 g $FeCl_3$/g silica). Then, the impregnated sample was exposed to pyrrole (Aldrich, 99%) vapors at 25 °C for 22 h in a closed vessel. The dark solid thus obtained was heated under N_2 to 850 °C (3 °C min^{-1}) for 1 h. Finally, the carbonized composite was treated with hydrofluoric acid for 4 days to dissolve the silica framework. The carbon capsules with nitrogen functionalities have been designated as FeNC.

The NC electrocatalyst was synthesized according to previous report[196]. To be more specific, 3 g of $(C_6H_5O_7)_2Ca_3 \cdot 4H_2O$ purchased from Sigma Aldrich was heat-treated in a stainless-steel reactor up to 800 ºC at a heating rate of 3 ºC min^{-1} in the presence of nitrogen and held at this temperature for 1 h. The resulting black solid was then washed with diluted HCl (10%). Finally, the carbon particles were collected by filtration, washed with abundant distilled water and dried at 120 ºC for several hours. Afterwards, the mesoporous carbon was mixed with melamine, using a ratio of melamine/carbon as 4:1. Finally, the mixture was heat treated under nitrogen up to 800 ºC (heating rate of 3 ºC min^{-1}) for 1 h. The as-obtained N-doped mesoporous samples are denoted as NC.

Surface modification of amorphous nanocarbon composites via ionic liquids

4 mg of electrocatalysts (FeNC or NC) was mixed with 300 μL ethanol. Then 1.1 μL of IL was carefully added into the solution. The mixture was then ultrasonicated for 10 mins to homogeneously disperse the ionic liquids (ILs) into a slurry, the mixture was then anchored on a shaker to shake for 60 hours to make the ILs fully interacted with the electrocatalysts. FeNC and NC without addition of ILs were treated following the same process for comparison. The obtained slurry was then frozen at -20 °C, followed by a freeze dry process for 72 h. The obtained samples were named as FeNC, FeNC-IL, NC, NC-IL, respectively. To study the influence of different IL ratio in FeNC, FeNC-IL0.5 and FeNC-IL1.5 were synthsized using the same procedure, but the volume of IL added was 0.55 μL and 2.2 μL, respectively.

4.3 Electrical conductivity test

Four-probe electrical conductivity test: each sample was first pressed onto an adhesive and insulating substrate with 9 tons for 5 min to obtain a circular tablet with a diameter of 13 mm. The as-prepared tablet was then measured in a four-point probe apparatus at room temperature.

4.4 Electrocatalytic performance measurements

The fundamental principle of electrocatalytic measurements has been introduced in 1.1.4, therefore in this part we focus on introduce the experimental details applied in this thesis (Chapter 5-7).

In an ORR test, the electrode loading materials were prepared by mixing 1.8 mg catalyst (for catalysts in Chapter 5) or 4 mg catalyst (for samples in Chapter 6 and 7), 264 μL ethanol, 700 μL H_2O, and 36 μL nafion solution (5 % w/w). The mixture was then sonicated for 40 min to obtain a homogeneous slurry, then 5 μL and 14 μL of the slurry was deposited onto the glassy carbon (GC) disk of rotating disk electrode (RDE) and rotating ring-disk electrode (RRDE), respectively, followed by drying for 40 mins under room temperature in air to obtain the working electrode. The diameters of glassy carbon disks of RDE and RRDE are 3 mm and 5 mm respectively, so that the RDE and RRDE are working with the same mass loading of electrocatalyst per unit area.

All tests were performed on electrochemical workstation (Metrohm Autolab PGSTAT204), using a standard three-electrode cell, where an Ag/AgCl in 3M KCl solution was served as the reference electrode, and platinum wire as the counter electrode.

The catalyst loading was *ca.* 0.127 mg cm^{-2} (for electrodes in Chapter 5) and *ca.* 0.284 mg cm^{-2} catalyst (for samples in Chapter 6 and 7). Pt/C (20 wt %, Sigma-Aldrich, 738549) was prepared as electrodes for comparison with the same loading.

For the ORR tests undertaken in 0.10 M KOH solution, cyclic voltammetry (CV) was performed in nitrogen or oxygen-saturated electrolytes as noted in each figure, at a scan rate of 100 mV s^{-1}. For the ORR tests undertaken in 0.10 M $HClO_4$ solution, CV was performed in nitrogen and oxygen-saturated electrolytes, at a scan rate of 50 mV s^{-1}. In both KOH and $HClO_4$ electrolyte, linear sweep voltammograms (LSV) were obtained a rotation rate of 1600 rpm and a scan rate of 10 mV s^{-1}. The onset potential is determined as the potential required for a current density of -0.1 mA cm^{-2} (vs. RHE).

For the RRDE test, same scan rate and potential range were applied as that of RDE. In addition, the ring potential was held at 1.5 V vs. RHE to oxidize any H_2O_2 produced during the reaction. The working electrode is composed of a 5 mm GC disk electrode with a Pt ring electrode (375 μm gap). The following equation was used to calculate the percentage of H_2O_2 released during the reaction:

$$\% H_2O_2 = 100 \frac{2I_R/N}{I_D + (I_R/N)} \quad \text{Equation 4-2}$$

Where I_R refers to the faradaic current at the ring, I_D is the faradaic current at the disk, N is the H_2O_2 collection coefficient at the ring, which was provided by the manufacturer, N is 0.249 for this RRDE working electrode.

Stability test

In order to investigate whether the electrode can generate stable currents during the long-term working, stability of the catalyst was obtained by current−time chronoamperometric responses measured on RDE electrode at the potential under which the current density reaches 3 mA cm^{-2} for each sample, at rotating speed of 800 rpm.

Methanol tolerance

As has been introduced in Chapter 1.1, DMFCs is a promising power source for mobile applications. However, due to the fact that methanol goes easily to the cathode through membrane, its poisonous effect on the electrocatalysts is a key issue reducing the efficiency and power density of the device. Therefore, the methanol tolerance of the electrocatalyst is significantly required.[197] In this work, methanol tolerance was tested by chronoamperometric responses, during which 2M methanol was injected into the electrolyte at 200s.

Electrochemical impedance spectroscopy measurements were conducted under 1600 rpm in O_2 saturated electrolyte and at the potential under which the current density reaches 3 mA cm^{-2} for each sample. The frequency range is 0.01 Hz-10^6 Hz.

4.5 Demonstration of the reproducibility

Hereby, two batches of NC-1000 sample in Chapter 5 was picked as an example to present the repeatability of the work. Mass records in **Table 4-2** demonstrated the consistent yield between two batches. Typical characterizations were picked to demonstrate in to show the consistent morphology and ORR activity of the two batches of the NC-1000. N_2 sorption isotherms in **Figure 4-4**(a) are similar between the two batches, which proved

the reproducibility of the micro-structure of the samples. The CV curve in **Figure 4-4**(b) demonstrated very close peak potential and intensity. The slightly difference of the ORR activity in **Figure 4-4**(b, c) resulted from different room temperature, which was uncontrollable under the experimental conditions at the time. In order to avoid temperature-induced errors that lead to different sample-to-sample relationships, each set of samples (eg. NC, NC0.05, NC0.25, NC-1000, NC0.05-1000, NC0.25-1000) were operated at the same room temperature.

Table 4-2 Mass record of two batches of NC-1000 in Chapter 5 to demonstrate the reproducibility of the samples.

Sample	Mass record				
NC-1000	CS (mg)	CS-HTC (mg)	CS-1000 (mg)	HTC yield (%)	Annealing yield (%)
Batch-1	180	56	27	31	48
Batch-2	180	54	26	30	48

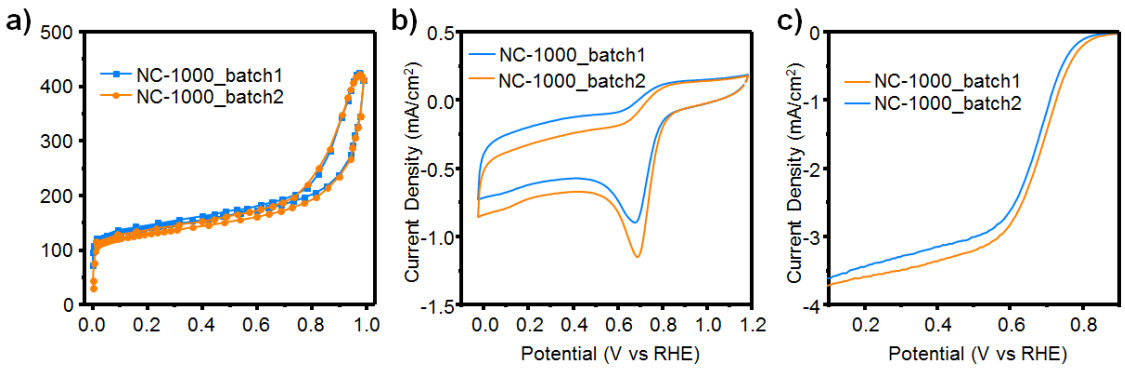

Figure 4-4 Two batches of NC-1000 samples in Chapter 4 is picked to prove the reproducibility of the samples: (a) The N_2 sorption isotherms, (b) CV curves of NC-1000 in O_2-saturated 0.10 M KOH solution. The scan rate was 100 mV s^{-1}. (c) LSV curves of different samples in O_2-saturated 0.10 M KOH solution with a rotating rate of 1600 rpm. The scan rate was 10 mV s^{-1}. Note that the difference of ORR CV and LSV curves in figure (b) and (c) resulted from different room temperature, which is uncontrollable under the experimental conditions at the time.

5 Graphene/nitrogen-doped porous carbon sandwiches for metal-free oxygen reduction reaction: conductivity versus active sites

5.1 Introduction

The ideal electrocatalyst for ORR requires a conductive and porous framework to facilitate electron transfer and mass/gas diffusion at the interface between the electrolyte, active sites, and gas phase. In addition, effective and fully accessible active sites are required for superior catalytic activity. The nature and the amount of the active N-containing site plays a significant role in the ORR performance.[8, 198, 199] The effect of the carbon matrix is also very important, influencing the electrical conductivity,[200] length-to-width ratio,[201] topological defects,[202, 203] surface roughness,[204] particle size, etc.[205] However, the synergistic role of the carbon framework coupled with heteroatom (nitrogen) doping effects in ORR has thus far not been investigated. The major obstacle is the difficulty of simultaneously controlling both the structural features of the carbon matrix and the characteristics of the nitrogen dopants.

5.2 Results and discussion

Herein, a carbon-carbon hybrid structure was proposed to demonstrate the different roles of the active sites and the carbon matrix. These composites are based on chitosan-derived NC shells hybridized with conductive graphene frameworks (**Figure 5-1**). Chitosan, an abundant and renewable biomass material, is employed to generate N-containing active sites via the hydrothermal carbonization (HTC) process.[204, 206] Graphene oxide (GO) with an ultra-thin lamellar structure and rich in functional surface groups is introduced as a

multi-functional substrate firstly to anchor the chitosan precursors, direct their carbonization, and help the resultant NC shells to adhere onto the graphene sheets (**Figure 5-1**a). A series of nanocomposites with tuneable electrical conductivity and nitrogen-containing active sites are thus produced by carefully adjusting the mass ratio between chitosan and GO. The addition of graphene improves the conductivity, but simultaneously decreases the net number of active sites derived from the nitrogen precursor.

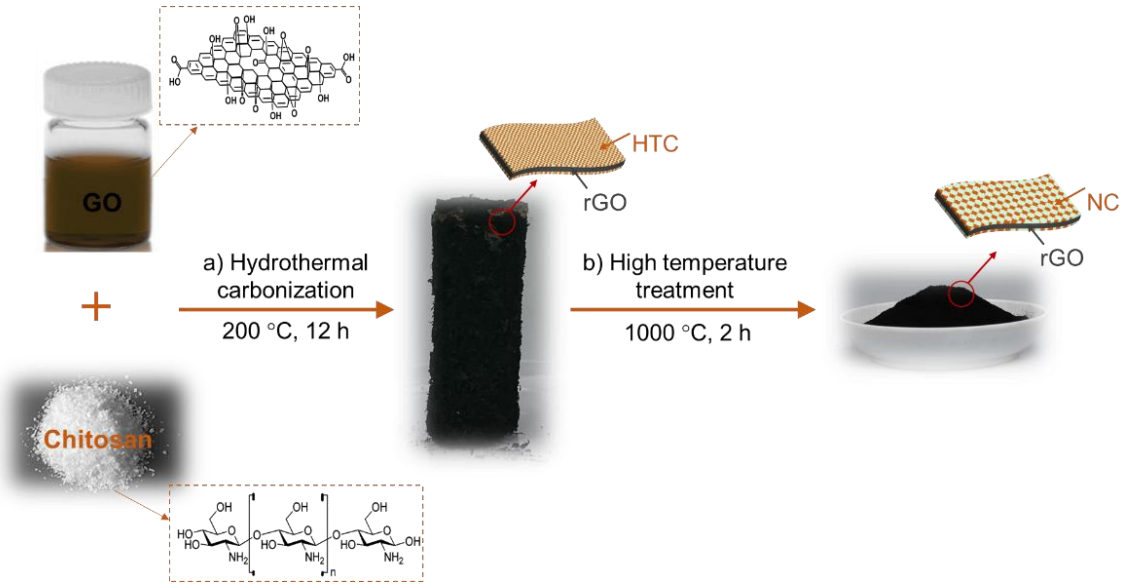

Figure 5-1 A scheme of the preparation of NC/rGO composites. (a) Hydrothermal carbonization of the mixture of GO and chitosan at 200 ºC for 12 h. (b) After washing and freeze drying, the as-obtained material was annealed at 1000 ºC for 2 h.

5.2.1 Structure and surface chemistry of electrocatalysts

A family of NC/rGO composite electrocatalysts were thus fabricated with a GO mass content ranging from 0 to 25 % (**Table 4-1**). The as-obtained products are denoted as NC/graphene composites (NCG): NC, NCG0.05, and NCG0.25, respectively. During the hydrothermal process, under subcritical conditions at 200 °C, the GO is converted to

reduced graphene oxide (rGO) with high electrical conductivity while the chitosan is hydrothermally carbonised to NC. The HTC process of chitosan ends up obtaining nitrogen-derived particles with oxygen-containing hydrophilic functional groups, which make it very accessible for hybridization process.[92, 207, 208] The sequential high-temperature treatment under inert atmosphere improves the graphitization degree of NC leading to different types of hybrid carbon-carbon materials with distinctive surface chemistries and properties (**Figure 5-1**).

Figure 5-2 shows the morphology and microstructure of the samples characterized by scanning and transmission electron microscopy (SEM and TEM). The pristine NC obtained through the hydrothermal carbonization of chitosan exhibits irregular spherical particles, in good agreement with previous reports (**Figure 5-2**a).[209] With the addition of GO, the composites show completely different morphologies (**Figure 5-2**b, c). The introduction of 5 % GO leads to a large flat agglomerate around 10 µm whereby the NC particles are uniformly anchored on both sides of the GO sheets (**Figure 5-2**b). The size of NC particles in NCG0.05 is smaller than those in pristine samples (**Figure 5-2**a), indicating that the GO also act as stabilisers during the HTC process. The polar functional groups in the GO surface interact with the chitosan precursors and subsequently carbonize on the resulting rGO structure, consequently there are very few free NC particles in NCG0.05 (**Figure 5-2**b). When the GO amount was increased to 25 %, the resultant sample exhibits a similar morphology as pristine rGO, without any obvious NC particles (**Figure 5-2**c, **Figure 5-3**). In this case, a thin layer of nitrogen-doped carbon was coated onto GO. This has been previously observed during the hydrothermal carbonisation of

carbohydrates in the presence of inorganic particles when the concentration of the carbohydrate is low compared with that of the inorganic material to be carbon coated.[11]

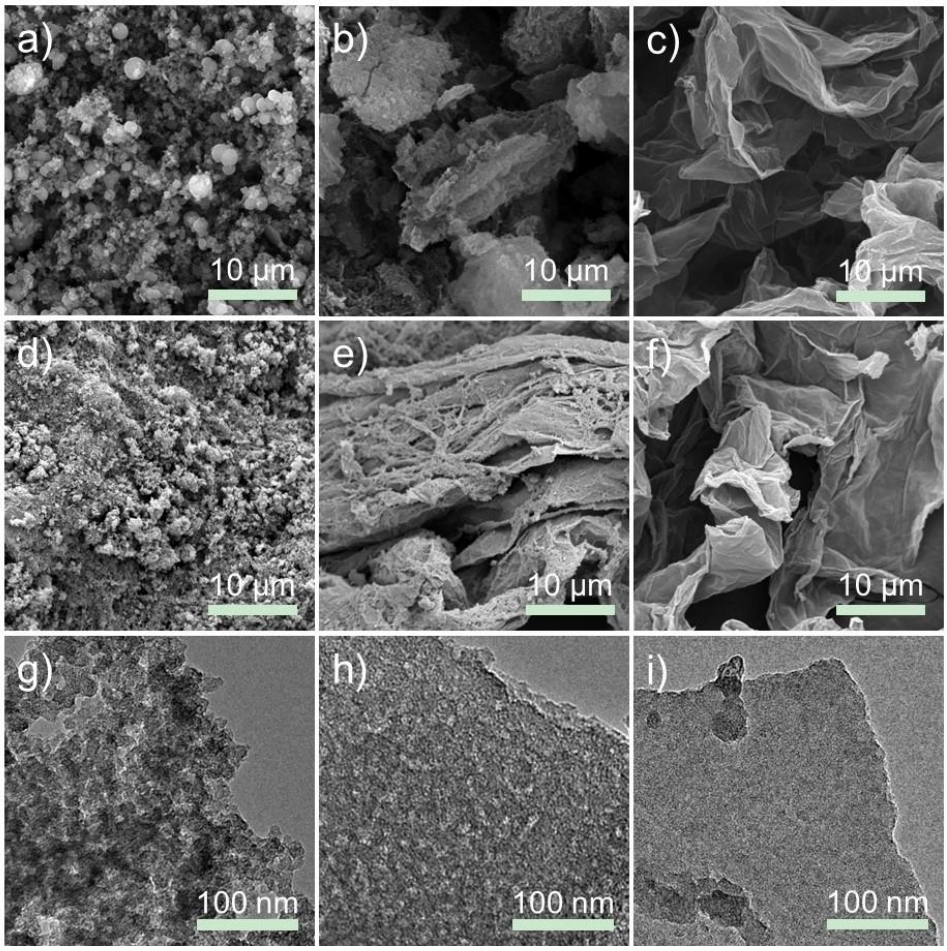

Figure 5-2 SEM images of (a) NC, (b) NCG0.05, and (c) NCG0.25 obtained after HTC process with different chitosan/GO ratios. SEM images of (d) NC-1000, (e) NCG0.05-1000, and (f) NCG0.25-1000 obtained after high-temperature treatment. TEM images of (g) NC-1000, (h) NCG0.05-1000, and (i) NCG0.25-1000 sample.

After further high-temperature annealing under N_2 atmosphere at 1000 °C, all samples maintain their overall morphologies however the NC particles in NC and NCG0.05 are visibly shrunk (**Figure 5-2**d-f).[210, 211] The corresponding products are denoted as NC-1000, NCG0.05-1000, and NCG0.25-1000, respectively. The TEM images further reveal

their hierarchical structures (**Figure 5-2**g-i). NC particles with a size of ca. 20 nm are interconnected into a porous framework (**Figure 5-2**g). With the presence of graphene sheets, however, porous NC shells are coated on GO and exhibit the laminar structure like rGO (**Figure 5-2**h, i, **Figure 5-3**b).

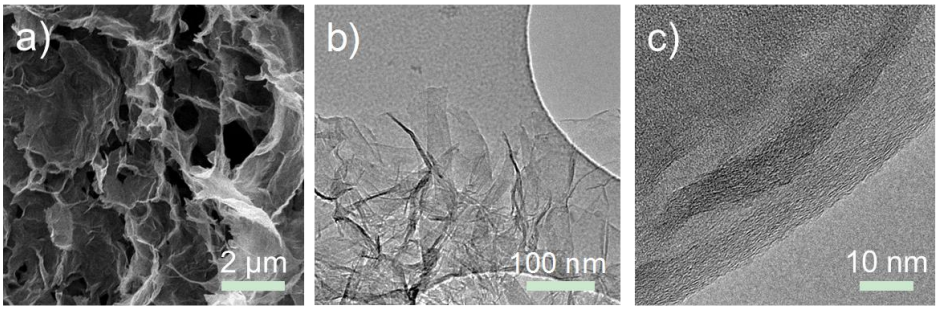

Figure 5-3 (a) SEM image and (b, c) TEM images of rGO obtained after HTC and high-temperature annealing.

The final yields support the fact that a strong interaction occurs between the two components during the hydrothermal treatment. As shown in **Table 5-1**, the yield of NCG from GO and chitosan mixed system is higher, compared with the result summed up from monocomponent systems of GO and chitosan. This suggests that there is interaction between the GO and chitosan during the HTC process, that the laminar structure and surface functionalities of the GO facilitate the transformation of chitosan during this process. FTIR spectra reveals no obvious shifts of band position (**Figure 5-4**), demonstrating similar chemical bond composition in NC, NCG0.05 and NCG0.25. However, the relative strength of the band varies at around 800 and 1250-1600 cm^{-1} as indicated in shaded area in **Figure 5-4**, which corresponds to the triazine ring vibration and stretching modes of the heterocyclic CN,[212-214] respectively. This indicates that the

induction of GO directs the assembly process of NC shell, resulting in a varied proportion of C-N bonds, but did not change the type of chemical bonds.

Table 5-1 Mass record of pure GO, pure NC, NCG0.25, NCG0.05 during fabrication process.

	GO (mg)	**Chitosan (mg)**	**Monocomponent-calculated yield (mg)[a]**				**Experimental yield (mg)**	
			rGO	HTC-chitosan	Product			
GO	60	0	25.9	0	25.9	43%	25.9	43%
NC	0	1200	0	372.0	372.0	31%	372.0	31%
NCG0.25	60	180	25.9	55.8	81.7	34%	122.6	51%
NCG0.05	60	1200	25.9	372.0	397.9	32%	672.4	53%

a) The monocomponent-calculated yield was calculated based on the yield of chitosan and GO in monocomponent HTC systems. Experimental yield refers to the mass of product obtained in the actual experiment.

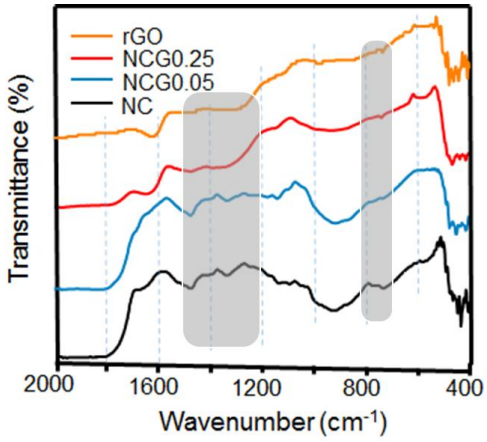

Figure 5-4 FTIR spectra of NC, NCG0.05, NCG0.25 and rGO. The shaded area at around 800 cm^{-1} and 1250-1600 cm^{-1} indicates the different relative strength of the signal, which corresponds to the triazine ring vibration and stretching modes of the heterocyclic CN, respectively.

The introduction of graphene improves the electrical conductivity (**Table 5-2**). For the pristine NC sample, the electrical conductivity is too low to be determined by the four-probe method. With the addition of GO, the conductivity increases to 0.05 S m^{-1} for NCG0.05 and 29.2 S m^{-1} for NCG0.25. GO has been partially reduced into rGO during HTC treatment, which provides a conductive skeleton for the composites. After high-

temperature treatment, all samples display improved electrical conductivity due to the "graphitization" of the hydrothermal carbons. Similar tendency can be obtained in impedance testing for high temperature treated samples (**Figure 5-5**).

Table 5-2 Electrical conductivity of different samples measured by the four-probe method.

Sample	NC	NCG 0.05	NCG 0.25	NC-1000	NCG0.05-1000	NCG0.25-1000
Conductivity ($S\ m^{-1}$)	N/A	0.05	29.2	6.5	12.0	57.6

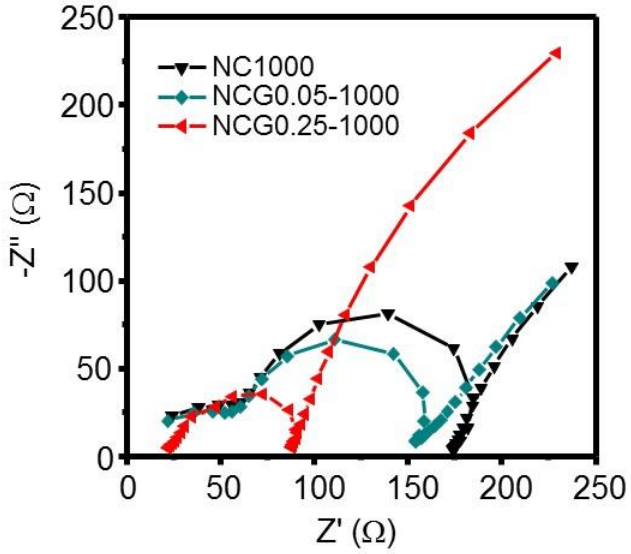

Figure 5-5 Nyquist plots of NC1000, NC0.05-1000, NC0.25-1000 in oxygen-saturated of 0.1M KOH at 1600 rpm. The frequency of measurement is started from 10^6 Hz and decreases until the semicircle is fully displayed.

Energy dispersive spectroscopy (EDS) mapping of NCG0.25-1000 demonstrates a uniform distribution of nitrogen and carbon elements, demonstrating indeed that rGO sheets are covered by the NC shells (**Figure 5-6**a-c). X–ray photoelectron spectroscopy (XPS) analysis was performed to further investigate the nitrogen incorporation in NCG composites (**Table 5-3**). High-resolution XPS spectra of N1s peaks are presented in

Figure 5-6 (d, e). For HTC products, the total nitrogen contents are 4.50 ± 1.00 at. %, and the bonding states can be assigned to three dominant configurations: pyridinic-N (ca. 398 eV), pyrrolic-N (ca. 400 eV) and quaternary-N (ca. 401 eV), respectively.[215, 216] It is notable that the contents of both total nitrogen, quaternary-N and pyrrolic-N are increased after the introduction of GO (NCG0.05), which demonstrates that indeed the GO influences the hydrothermal carbonization of chitosan and the nitrogen incorporation into the carbon matrix (**Table 5-3**, **Figure 5-7**). Further addition of GO (NCG0.25) decreases

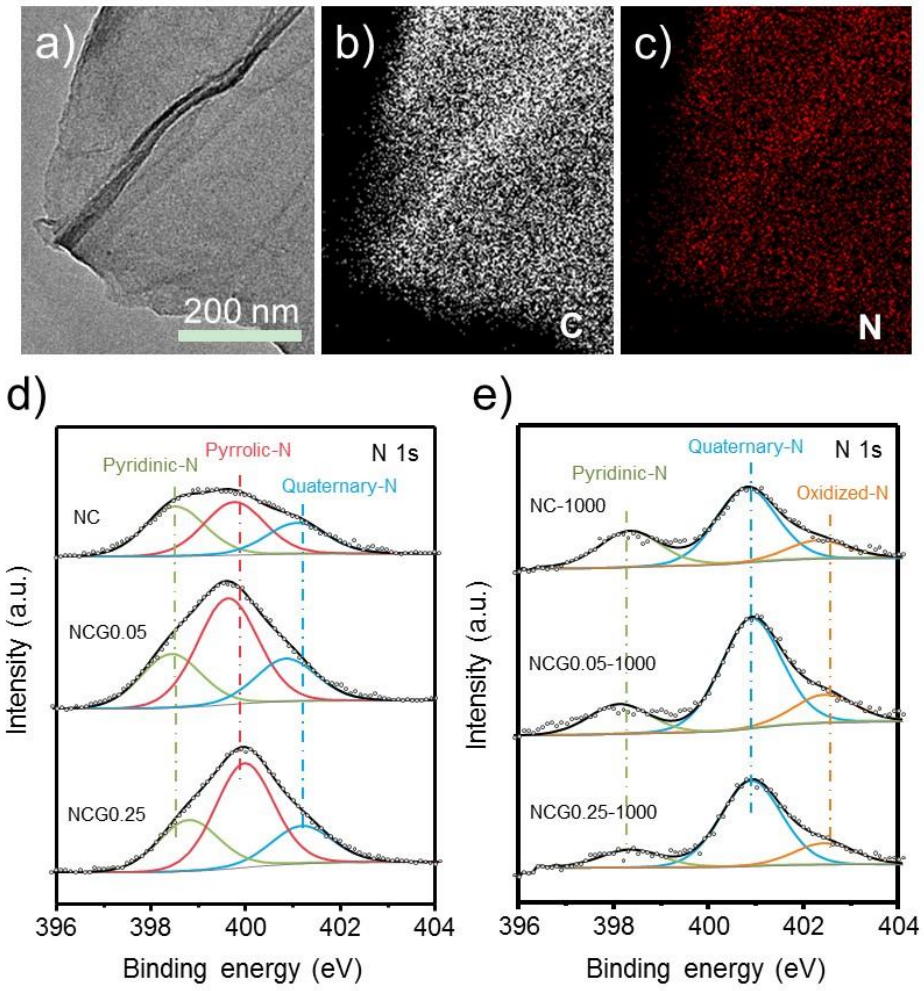

Figure 5-6 (a) TEM image of NCG0.25-1000 and the corresponding EDS mapping, showing the uniform distribution of (b) C and (c) N elements. The high-resolution N 1s spectra of samples obtained (d) after HTC or (e) after high-temperature annealing.

the amount of nitrogen dopants due to the net reduction of nitrogen precursors. After the high-temperature annealing, the nitrogen contents decreased to 1.45 ± 0.20 at. %, with an obvious decrease of pyridinic N, disappearance of pyrrolic N and generation of oxidized-N (> 402 eV). It has been reported that both pyrrolic and pyridinic structures are unstable under high temperature and tend to transform into more stable quaternary nitrogen configuration.[217, 218] Besides, the oxidized-N, such as pyridinic-N^{+}-O^{-} is considered as a stable configuration,[218] which is ascribed from the reaction between nitrogen dopants and oxygen-containing functional groups of GO during annealing.

Table 5-3 XPS results of different samples.

Sample	Atom Species (at. %)						
	C	O	N	Pyridinic-N	Pyrrolic-N	Quaternary-N	Oxidized-N
NC	75.16	21.39	3.45	1.27	1.38	0.79	-
NCG0.05	76.13	18.22	5.65	1.49	2.97	1.19	-
NCG0.25	80.97	15.01	4.02	1.08	2.15	0.79	-
NC-1000	90.87	7.45	1.68	0.47	-	0.97	0.24
NCG0.05-1000	96.48	2.04	1.48	0.26	-	0.98	0.23
NCG0.25-1000	94.39	4.39	1.22	0.17	-	0.84	0.21

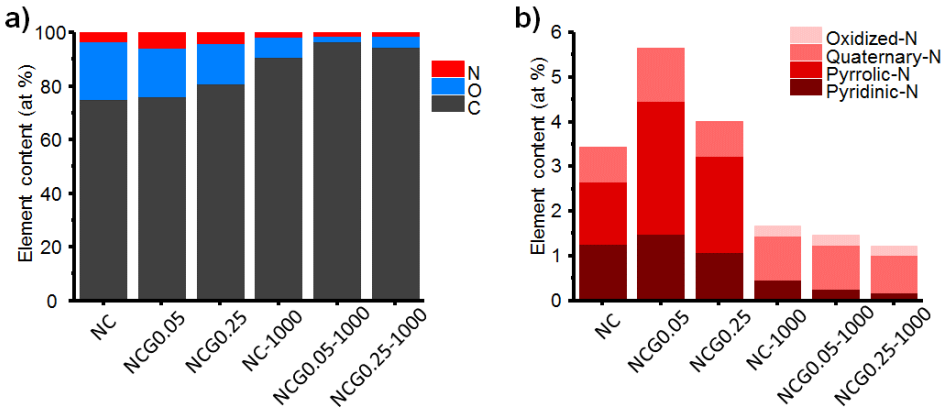

Figure 5-7 Content of (a) C, N, O, and (b) different N configuration, respectively, obtained from XPS results in Table 5-3.

High-temperature treatment not only regulates the configuration of nitrogen, but also modulates the graphitization degree and porosity. High-resolution TEM (HRTEM) images of the NC particles in NC-1000 are presented in **Figure 5-8**(a) indicating the amorphous carbon structure. However, after annealing for 2 h, distinct graphitic layers or graphene rings with diameter of several nanometers are observed (**Figure 5-8**b), which are remarkably different from the HTC products. Functional groups are mostly removed during the high temperature carbonization step, while the amorphous structure is transformed into a more graphitized structure. Porosity and BET surface areas of different samples were evaluated using nitrogen sorption at -196 °C with Density Function Theory (DFT) method (**Figure 5-8**c-f). The specific surface area (SSA) of HTC products significantly increases after annealing along with the total pore volume (**Table 5-4**). Upon further carbonization at high temperature, mesopores of around 6 nm demonstrate a peak distribution (**Figure 5-8**e, f), which is consistent with the HRTEM results (**Figure 5-8**a, b). The BET surface area and pore volume values of NC or NCG0.25 are increased more than ten-fold after annealing. This change is ascribed to the structural transformation of NC shells derived from chitosan, as supported by TEM. NCG0.05-1000 exhibits the highest BET surface area, 338 $m^2 g^{-1}$ and a high pore volume of 0.9 $cm^3 g^{-1}$. The BET surface area and pore volume of NCG0.05 is about ten and five times higher than both NC and NCG0.25, respectively. This is most likely due to the fact that GO sheets help disperse of NC particles leading to a smaller particle size during the hydrothermal reaction (**Figure 5-2**b). Additionally, the NC shells anchored on GO can effectively restrain the restacking of graphene sheets, resulting in a higher BET area and pore volume after pyrolysis. In the case of NCG0.25, since the NC deposited on graphene is very thin, there

is little effect on the BET surface area and pore volume in comparison with NCG0.05 (**Figure 5-2**c).

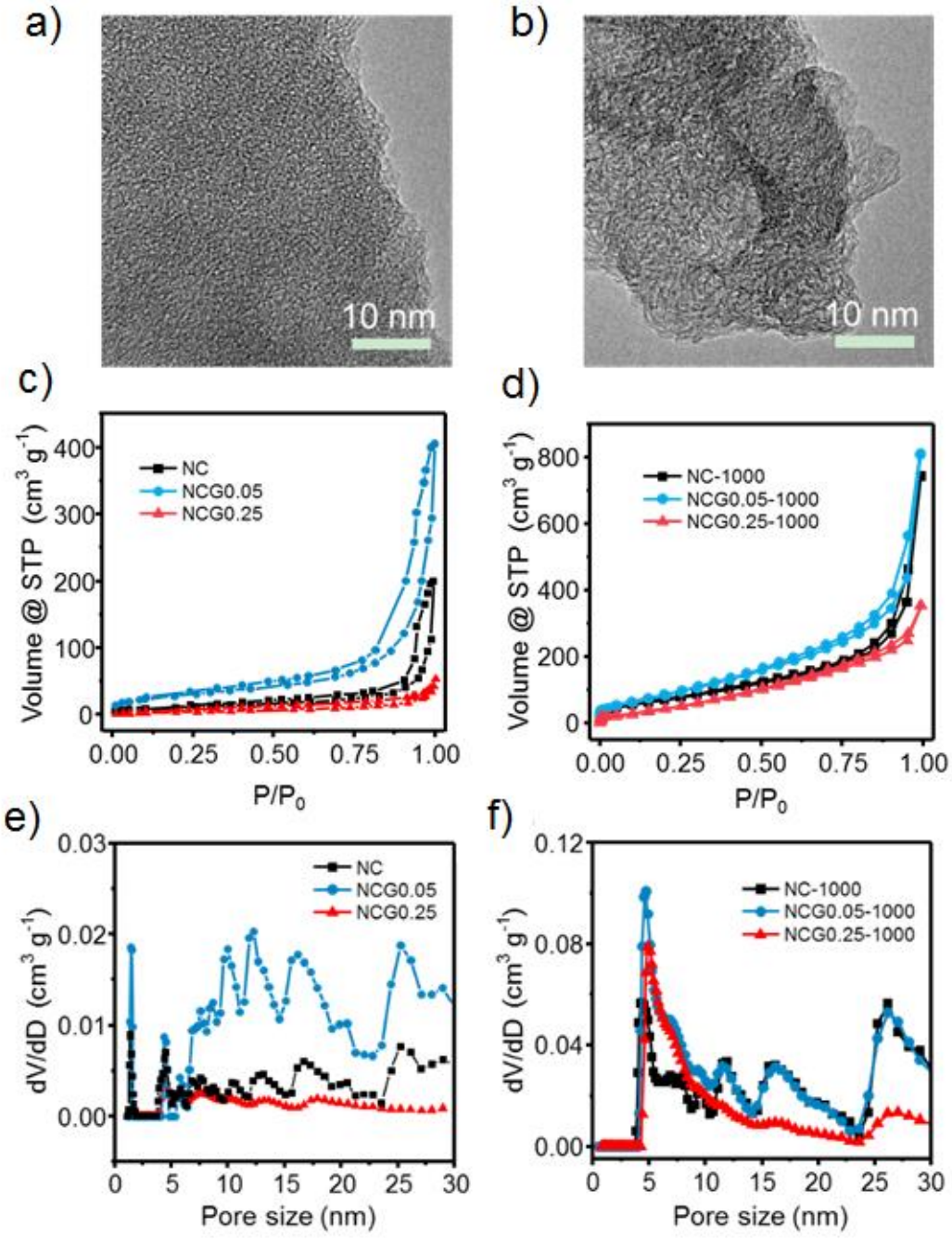

Figure 5-8 HRTEM image of (a) NC sample and (b) NC-1000 sample. The N_2 sorption isotherms of samples obtained after (c) HTC and (d) high-temperature annealing. The pore size distribution of different samples obtained after (e) HTC and (f) after annealing.

Table 5-4 Specific surface area and total pore volume of different samples.

Sample	NC	NCG0.05	NCG0.25	NC-1000	NCG0.05 -1000	NCG0.25 -1000
SSA (m^2 g^{-1})	36	99	25	278.9	339	223
Pore volume (cm^3 g^{-1})	0.1	0.34	0.06	0.81	0.91	0.43

5.2.2 ORR performance

The ORR electrocatalytic activities of various NC/rGO composites were measured in an alkaline solution (0.10 M KOH). A commercial Pt/C catalyst (20 wt% loading, Sigma) was also measured under the same conditions for comparison (**Figure 5-9**). The cyclic voltammetry (CV) curves conducted in both O_2 and N_2 saturated electrolytes is shown in **Figure 5-10**(a). In the presence of O_2, distinct ORR responses were observed on all samples in contrast to the quasi-rectangular voltammograms for N_2-saturated solution, suggesting their good reactivity for ORR. It is notable that the peak potential of NCG0.25 is positively shifted by 65 mV, compared with NC. After high-temperature annealing, however, the NC-1000 sample exhibits the lowest overpotential and highest peak current density, clearly indicating its excellent catalytic activity even without any graphene addition (**Table 5-6**).

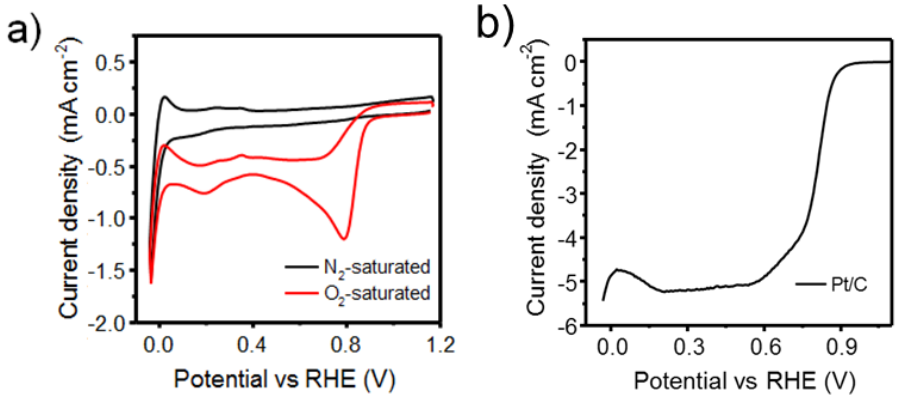

Figure 5-9 (a) CV curves of commercial Pt-C catalyst in N_2 or O_2-saturated 0.10 M KOH solution. The scan rate was 100 mV s^{-1}. (b) LSV curves of commercial Pt-C catalyst in O_2-saturated 0.10 M KOH solution with a rotating rate of 1600 rpm. The scan rate was 10 mV s^{-1}.

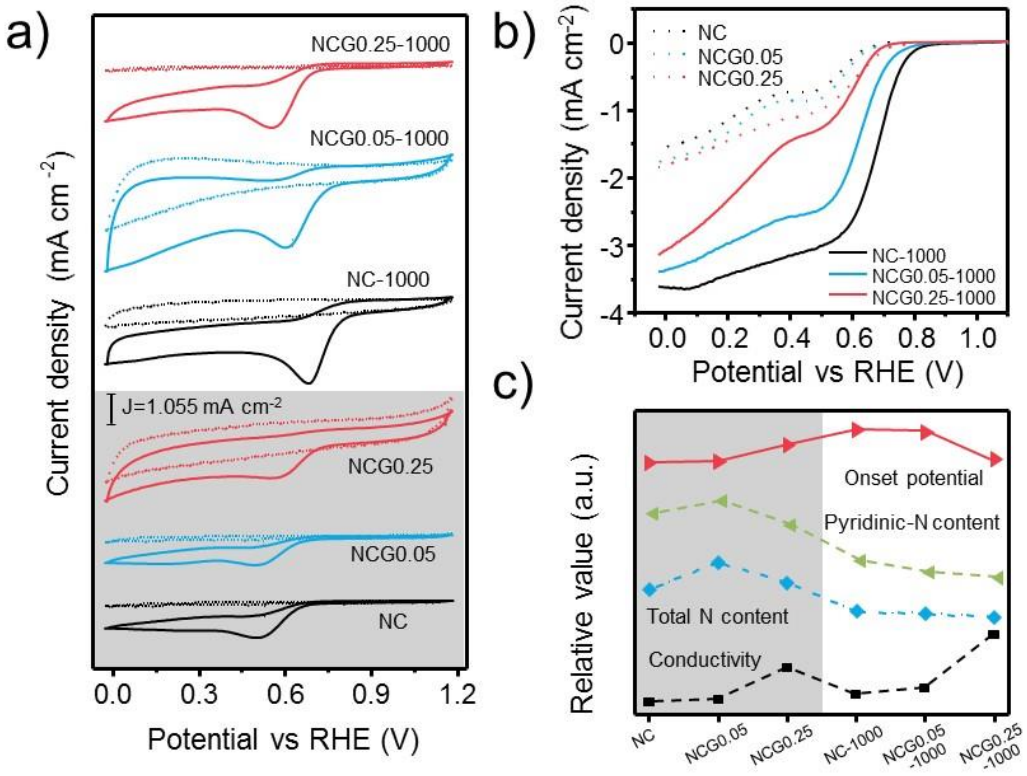

Figure 5-10 (a) CV curves of different samples in N_2 (dot) or O_2-saturated (line) 0.10 M KOH solution. The scan rate was 100.0 mV s^{-1}. (b) LSV curves of different samples in O_2-saturated 0.10 M KOH solution with a rotating rate of 1600 rpm. The scan rate was 10.0 mV s^{-1}. (c) The comparison between performance and material properties, such as conductivity, total N content, and pyridinic-N content. The catalyst loading was ca. 0.127 mg cm^{-2} for all measurements.

To further investigate the ORR activity and underlying mechanism, linear sweep voltammetry (LSVs) was performed using a rotating disk electrode (RDE) with a rotation rate of 1600 rpm. As shown in **Figure 5-10**(b), all the annealed samples substantially outperform the HTC samples in respect to both overpotential and current density. Increasing GO addition resulted in more positive onset potential and higher diffusion-limited current density (J_D) relative to the HTC products. The onset potential of NCG0.25 is *ca.* 70 mV higher than NC, while the current density (J_D) gradually increased from 1.57, 1.75 to 1.85 mA cm^{-2}, for NC, NCG0.05 and NCG0.25, respectively. In the case of

annealed samples, however, the ORR performance shows negative correlation with the graphene content. Unexpectedly, the NC-1000 exhibits the best ORR activity with an onset potential of *ca.* 794 mV, which is dramatically shifted from 627 mV of the NC sample. Besides, the J_D is more than twice that of NC. The LSV curve of NCG0.25-1000 still exhibits an obvious two-plateau peroxide pathway, with a slight increased current density but even lower onset potential. It indicates a small role of the high-temperature treatment for NCG0.25, in contrast to NC. Current−time chronoamperometric responses **(Figure 5-11**) were measured at peak potential in CV curves as shown in **Figure 5-10**(a). The NC-1000 shows improved stability compared with NC, both demonstrates better stability than commercial Pt-C catalyst.

Table 5-5 The summary of ORR peak potential and peak current density in CV curves as shown in **Figure 5-10**.

Sample	Peak potential vs RHE (mV)	Peak current density (mA cm^{-2})
NC	510	0.517
NCG0.05	506	0.384
NCG0.25	575	0.362
NC-1000	690	1.055
NCG0.05-1000	609	0.935
NCG0.25-1000	563	0.899

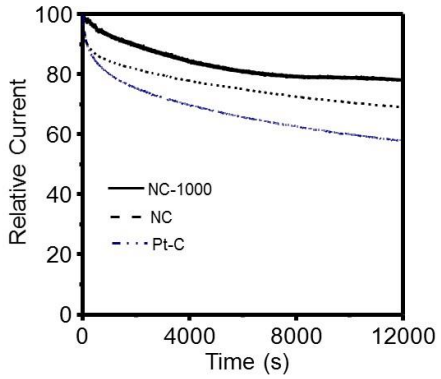

Figure 5-11 Current−time chronoamperometric responses of NC-1000, NC and Pt-C measured at peak potential in CV curves in O_2 saturated 0.1 M KOH electrolyte as shown in Figure 5-10a.

The peroxide yield was calculated using RRDE to evaluate the amount of H_2O_2 generated during the ORR reaction to compare ORR mechanism (**Figure 5-12**). All samples show H_2O_2 yield higher than 20%, while NCG0.25 shows a lowest H_2O_2 yield of around 29%, which is superior than NCG0.05 and NC at the H_2O_2 yield of around 47% and 40%, respectively. For annealed samples, NCG0.25-1000 exhibited a distinctive increase in H_2O_2 yield of around 61%.

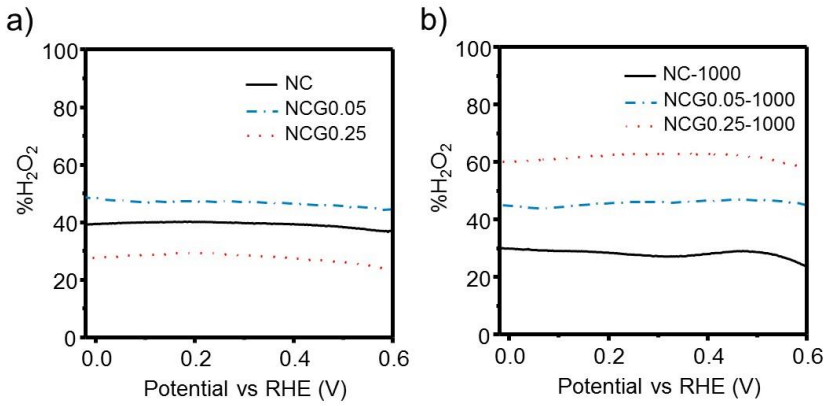

Figure 5-12 Peroxide yields of (a) NC, NCG0.05, NCG0.25 and (b) NC-1000, NCG0.05-1000, NCG0.25-1000 in O_2-saturated 0.1M KOH at rotating speed of 1600 rpm.

5.2.3 The relationship between the ORR performance and electrocatalyst

Detailed structure-performance investigations are carried out to rationalize this observation (Figure 5-10c, Figure 5-13 and Table 5-6). Both electrical conductivity and catalytically active sites are two critical parameters for metal-free carbon based electrocatalysis.[200] Nitrogen-induced active sites are responsible for the ORR activity of NC materials, although the exact mechanism of how this occurs is still debated. The increase in graphene content enhances the electrical conductivity, while the net amount of NC derived from chitosan is reduced.

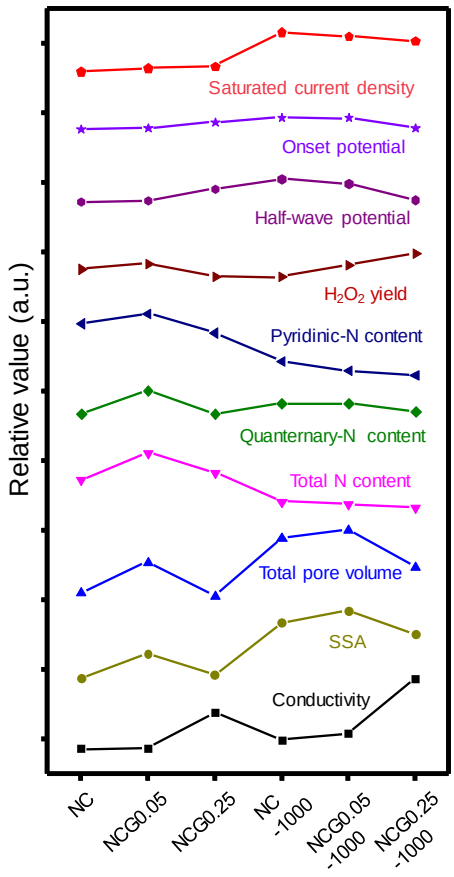

Figure 5-13 Detailed comparison between ORR performance and material properties.

Table 5-6 ORR activity observed from the LSV curves in **Figure 5-10**b.

	NC	NCG0.05	NCG0.25	NC-1000	NCG0.05 -1000	NCG0.25 -1000
Onset potential* (mV)	627	642	697	794	759	678
Saturated current density (mA cm^{-2})	1.57	1.75	1.85	3.61	3.39	3.15
Half wave potential (mV)	340	357	524	666	600	363

* The onset potential is determined as the potential required for the current density of -0.1 mA cm^{-2} (vs. RHE)

The electrical conductivity of the hydrothermal carbons is so low that it largely limits the electron transport during catalysis, inhibiting the contribution from nitrogen-doped active sites and restricting the overall ORR activity. NCG0.05 is clearly inferior to NCG0.25 in ORR performance, although it has more nitrogen heteroatom dopants, higher SSA and

larger pore volumes (**Table 5-6**). On the other hand, once the electrical conductivity reaches a certain threshold, after additional high-temperature treatment, the active nitrogenated sites become the key factor indicating the material's ORR performance. The current density, onset potential and half-wave potential are considerably increased as now the electronic conductivity facilitates the transport to the active sites for electron transfer. In the case of the annealed samples, the variation of J_D, onset potential and half-wave potential follows the exact trend dictated by the nitrogen content, independent of conductivity. The NC-1000 with no GO but highest nitrogen performs better than NCG0.05-1000 and NCG0.25-1000. Notably, the amount of pyridinic-N content can be nicely correlated with onset potential and half-wave potential (Figure 5-10c, **Figure 5-13**), indicating the intrinsic activity of pyridinic-type nitrogen heteroatoms in good agreement with previous reports.[219, 220] Although the influence of active sites and electricity to H_2O_2 yield is still under debate, it is surprising to see that the H_2O_2 yield of both hydrothermal and annealed samples follow very similar tendency with that of J_D, onset potential and half-wave potential: H_2O_2 yield of NCG 0.25 is less than NC and NCG0.05, while in annealed case, NC-1000 shows substantially reduced H_2O_2 yield than NCG0.05-1000 and NCG0.25-1000, which is nicely correlated with the variation of electrical conductivity.

5.3 Conclusion

A series of NC/rGO hybrids were fabricated and demonstrated the different roles of both the active sites and the conductivity of the carbon matrix towards ORR performance. The chitosan-derived NC shells induced the formation of abundant active sites while reduced

graphene oxide sheets prompt electrical conductivity. After high-temperature treatment the nitrogen dopants were partly removed while the remaining ones transformed into more stable structures (pyridinic-N and oxidized-N), and the conductivity of composites is enhanced above a critical value. Low electrical conductivity limits access to the active sites. However, the amount and type of active sites are the main contributors to ORR activity when conductivity is no longer a limitation. The main conclusion of the study is that conductive additives, such as graphene, can improve some of the properties and performance of nitrogen doped carbons derived from biomass precursors, but they can also bring about side effects such as reducing net amount active sites, which should be carefully investigated.

6 Low-cost chitosan-derived N-doped carbons boost electrocatalytic activity of multi-wall carbon nanotubes

6.1 Introduction

Simple and low-cost methods in conjunction with new Fe-N-C electrocatalyst design strategies are needed in order to exploit their impressive ORR activity. In addition, the low catalytic activity of active sites in acid electrolytes remains a severe issue limiting their application in devices operating under those conditions.[221,222] In Chapter 5, a carbon-carbon hybrid sandwich structure was proposed to reveal the roles of catalytically active sites and the electrical conductivity in ORR. It has been demonstrated that good electrical conductivity was a very important prerequisite for electrocatalysts with ideal ORR activity.[223]

Here in this chapter, hydrothermal carbonisation of chitosan was used to introduce N-doped active sites in MWCNTs to enhance their ORR activity and stability in both alkaline and acid electrolytes. The resulting hybrid carbon-carbon nanocomposites exhibited synergistic effects between the conductive MWCNTs framework and their N-doped hydrothermal carbon (NC) coating. Chitosan, a renewable biomass-derived low-cost N precursor can be used to introduce N-active sites within the MWCNT framework. The iron carbide residues encapsulated inside the MWCNTs from their synthesis interact with the graphite carbon wall, activate the surrounding graphitic layers and hence provide active sites [224, 225], whilst the iron on the MWCNT surface complexes with chitosan and therefore generates highly efficient Fe-N-C-based active sites towards ORR. In addition, during the hydrothermal carbonisation (HTC) assembly process, chitosan forms a NC

carbon layer on the MWCNTs structure promoting the formation of a 3D network-like structure favouring mass and electron transfer. The results show that these hierarchical carbon nanotube networks exhibit enhanced ORR activity. Moreover, the active sites provide by MWCNTs are stabilised through the N-doped hydrothermal carbon coating acting as a protecting layer. Furthermore, this layer also hinders the H_2O_2 ORR by-product from poisoning the Fe-active sites present on the surface of CVD MWCNTs.

6.2 Results and discussion

6.2.1 Structure and surface chemistry of electrocatalysts

CVD-grown MWCNTs were used as a multi-functional substrate to provide the electric conductivity and iron resources of the resulting electrocatalyst, whilst, hydrothermal carbonisation of chitosan resulted in a nitrogen-doped carbon (NC) shell adhered to the MWCNTs.[20, 21] Subsequent high-temperature treatment under a N_2 atmosphere promoted the formation of N-active sites (**Figure 6-1**a-c).

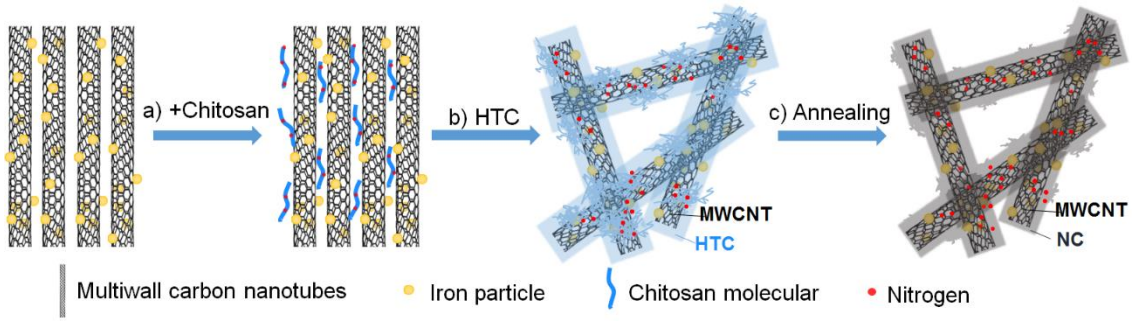

Figure 6-1 Preparation steps of NC-CNT-1000. (a) Addition of chitosan to MWCNTs; (b) hydrothermal carbonisation of the MWCNT and chitosan mixture at 200 °C for 12 h; (c) as-obtained material annealed at 1000 ºC for 2 h after washing and drying obtained carbon nanocomposites.

Scanning and transmission electron micrographs (**Figure 6-2, Figure 6-3**a-d) revealed the morphology and microstructure of the MWCNTs and NC-CNT after the hydrothermal carbonisation and annealing process, respectively. The MWCNT carpets were not evidently altered after the hydrothermal treatment, while the NC-CNT-HTC sample exhibited a pronounced 3D network structure compared to CNT-HTC (**Figure 6-2**a, b).

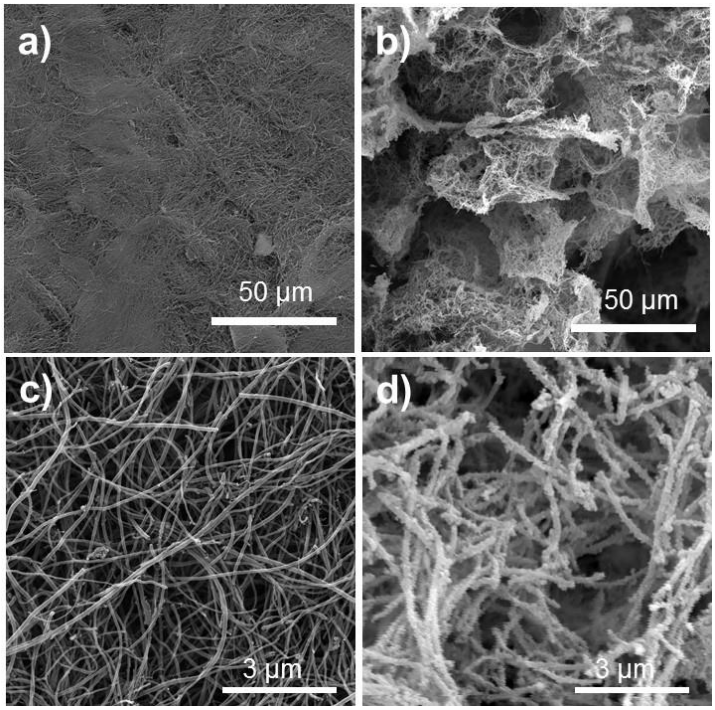

Figure 6-2 SEM images of samples after HTC process at 200 °C for 12 h: (a, c) pure MWCNTs after HTC process, and (b, d) chitosan-MWCNT hybrids (NC-CNT) synthesized via hydrothermal carbonization (HTC) process of MWCNT and chitosan mixture. Compared with pure MWCNT, the NC-CNT hybrids demonstrated similar tubular structure with larger diameter and more distinct 3-D network structure.

This change in the microstructure was promoted by the HTC process, during which the polar functional groups of hydrothermal carbon and the topological structure with unpaired electrons of MWCNTs interacted and consequently resulted in a layer of NC on the surface of MWCNTs. The NC-CNT-1000 demonstrated a similar 1-dimensional (1-

D) tubular morphology to that of the original MWCNTs (**Figure 6-3**a, b). HRTEM clearly demonstrated the existence of an amorphous layer of ca. 10 nm on the surface of the graphitic nanotube structure (**Figure 6-3**c, d). Yields obtained during processing of the NC-CNT-1000 samples indicated a calculated mass ratio of 1:1 of amorphous carbon to MWCNTs (**Table 6-1**).

Table 6-1 Mass record of the samples during synthesis process.

	Precursor (mg)	After HTC (mg)	After Annealing (mg)
CNT+NC	408	163	98
NC	360	115[a]	50[a]
CNT	48	48[b]	48[b]

[a] The mass is estimated by subtracting the mass of CNT from that of CNT+NC.

[b] The mass is estimated due to the inert property of CNT, assuming that the mass of CNT does not change during the reaction.

Porosity and BET surface areas of different samples were evaluated (**Figure 6-3**e, f). NC-1000 was also tested and listed for reference. The specific surface area (SSA) of the composites NC-CNT-1000 along with the total pore volume significantly increased compared with CNT-1000. (**Table 6-2**, **Figure 6-3**f). The addition of NC layer introduced mesopores of diameter smaller than 4nm, those mesopore structure didn't exist in absence of either MWCNT or chitosan. This further prove that the MWCNTs directed the assemble process of NC. The BET surface area of NC-CNT-1000 was more than five-fold higher compared to CNT-1000. The pore volume was doubled and an obvious increase of micropores was observed (**Figure 6-3**f, **Table 6-2**). This change is ascribed to the formation of N-doped carbon from chitosan.

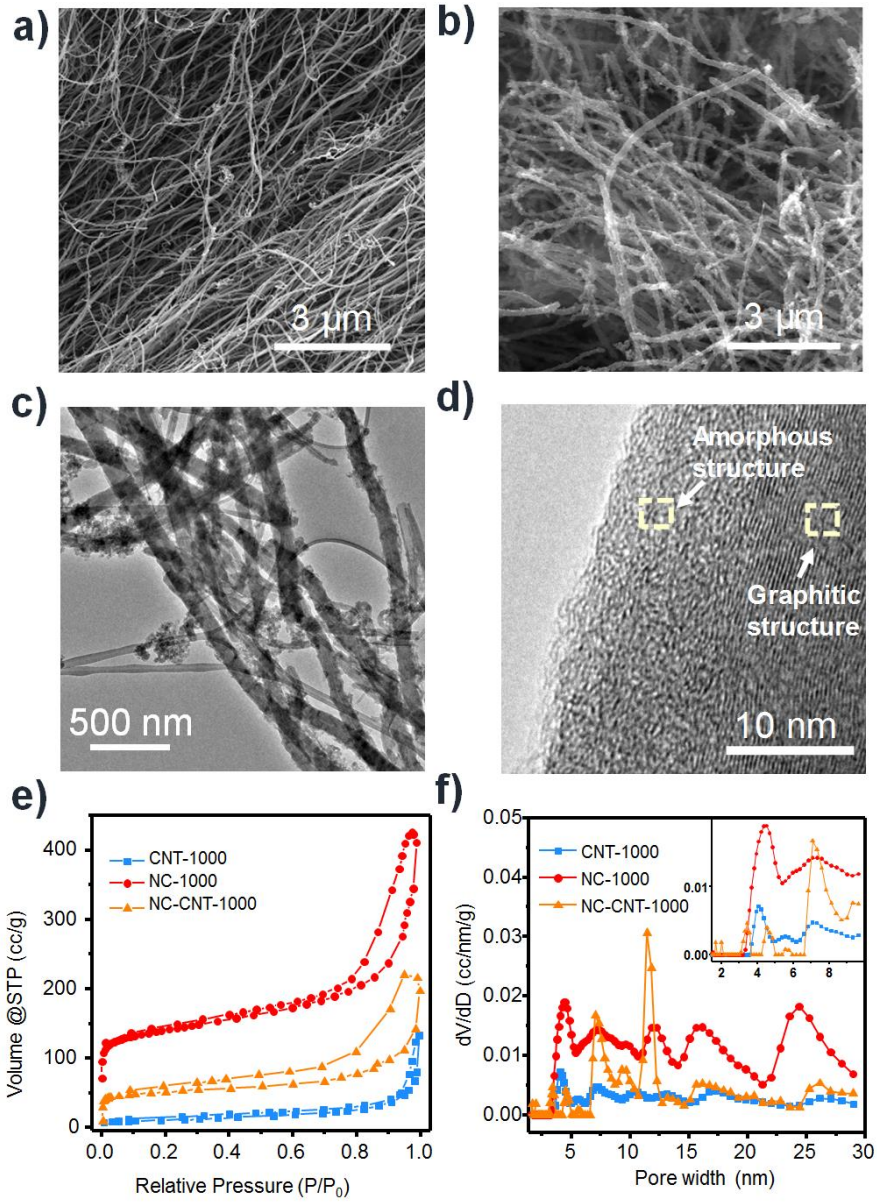

Figure 6-3 SEM images of (a) CNT-1000, (b) NC-CNT-1000. (c) Low resolution and (d) high resolution of TEM images of NC-CNT-1000. (e) The N_2 sorption isotherms of samples and (f) the pore size distribution calculated from QSDFT of the samples obtained after annealing.

Table 6-2 Summary of specific surface area and pore volume of different samples based on N_2 adsorption measurement at -196 ºC.

Sample	CNT-1000	NC-CNT-1000	NC-1000
SSA (m^2 g^{-1})	36	187	523
Pore volume (cm^3 g^{-1})	0.11	0.19	0.49
Micropore volume (cm^3 g^{-1})	0	0.06	0.16

The functional groups on the catalysts were investigated in order to understand the composition of the active sites. The existence of Fe was supported by XRD (**Figure 6-4**a). Both CNT-1000 and NC-CNT-1000 demonstrated a sharp (002) peak at around 26°, suggesting a high degree of graphitisation. The full width at half maximum (FWHM) of CNT-1000 and NC-CNT-1000 are 0.86° and 1.14°, respectively. Compared with CNT-1000, the obvious decrease in the (002) peak intensity and widened FWHM in NC-CNT-1000 indicated an interruption of the amorphous NC layer[190, 226, 227]. The peaks observed between 40–60º revealed the presence of iron carbide and iron oxide[28, 226, 227]. XPS spectra demonstrated the presence of 0.08 at% and 0.04 at% of Fe on the surface of CNT-1000

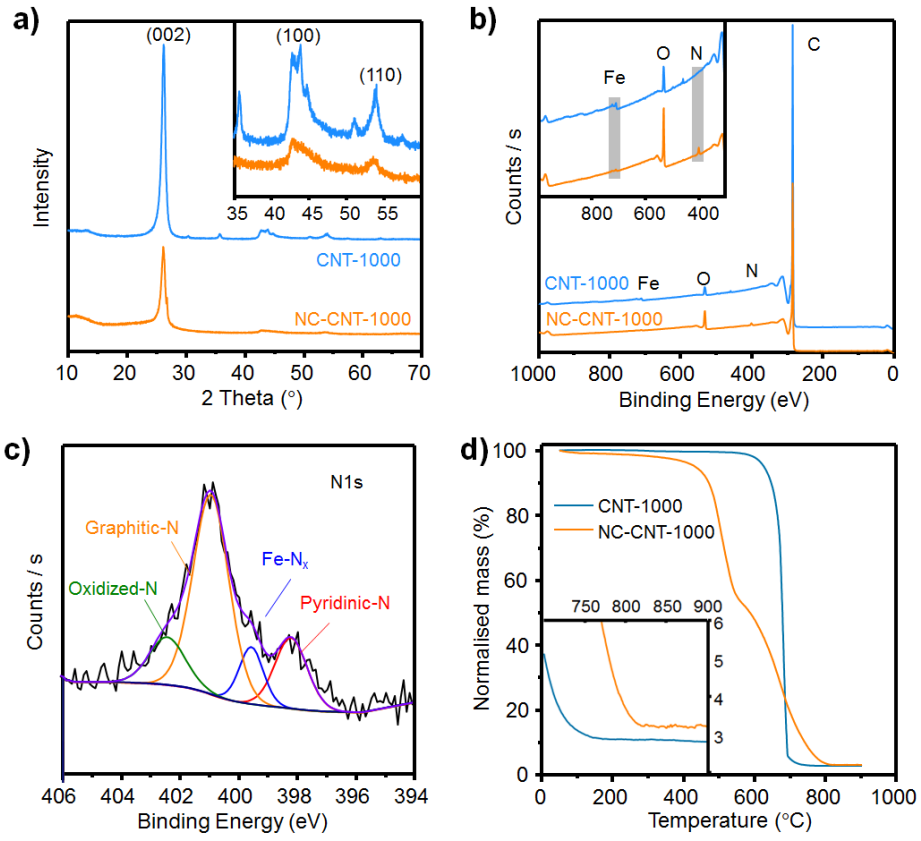

Figure 6-4 (a) X-ray diffraction patterns and (b) XPS survey spectra of CNT-1000 and NC-CNT-1000 respectively. c) The XPS N 1s spectra of NC-CNT-1000, and d) The TGA result of CNT-1000 and NC-CNT-1000.

Table 6-3 Summary of XPS survey spectra of different samples.

Sample	Atom Species (at. %)					
	C	O	N	Fe	N/C	Fe/C
CNT-1000	98.08	1.84	0	0.08	0	0.0008
NC-CNT-1000	93.61	5.15	1.20	0.04	0.01	0.0004

and NC-CNT-1000, respectively, and 1.2 at% of N on that of the NC-CNT-1000 (**Figure 6-4**b, c, **Table 6-3**). The reduction of the Fe content in NC-CNT-1000 was due to the introduction of amorphous nitrogen doped carbon layer. After the addition of the NC layer, four types of nitrogen sites could be observed: The peak at 399.6 eV demonstrated the N coordinated with Fe (Fe-N_x), indicating the formation of highly electrocatalytically active Fe-N-C based active sites. Peaks at 398.2 eV and 400.9 eV refer to the pyridinic-N and graphitic-N, respectively, both of which were effective active sites contributing towards ORR (**Figure 6-4**c, **Table 6-4**)[57]. According to TGA, the temperature at which the CNT-1000 loses 50 % of its mass is nearly 680 ºC (**Figure 6-4**d). This is very high for CVD MWCNTs and is typically observed in MWCNTs with low concentration of residual catalyst particles and high degree of crystallinity, both of which result from annealing. The NC-CNT-1000 showed two distinct drops which describes the amorphous/graphitic dual nature of the hybrid structure. TGA in air ended up with hematite demonstrated mass residual of 2.8 wt% and 3.2 wt% for CNT-1000 and NC-CNT-1000, respectively, which indicated the iron content of 2.0 wt% in CNT-1000 and 2.3 wt% in NC-CNT-1000. Elemental analysis demonstrated the N, C mass ratio of 4.45 wt%, and 78.45 wt%, respectively. The resultant calculated atom ratio of N/C and Fe/C based on TGA and EA in NC-CNT-1000 are 0.05, and 0.006, respectively, both of which are much higher than that calculated from XPS, which is 0.01 and 0.0004, respectively (Table 6-3). The

difference in atom ratio proves that the distribution of N, Fe elements in the surface and bulk phase is different. During the assembly processes, most iron remains inside or on the surface of the MWCNTs, resulting in iron distributed inside the MWCNTs and/or at the interface of amorphous/graphitic layer. Meanwhile, Fe anchored part of N, led to a higher N ratio in the bulk phase than outer surface. This is further proved by the formation of Fe-N based active sites and was protected by the NC-layer. TEM (**Figure 6-5**) showed that the coating carbon layer had a much higher distribution of N, while Fe was located mainly inside the MWCNT, or at the interface between of the MWCNT surface and the NC layer, which is consistent with the above analysis.

Table 6-4 Summary of XPS N1s spetra from **Figure 6-4**c

Sample	N Species (at. %)			
	Pyridinic-N	Fe-N_x	Graphitic-N	Oxidized-N
NC-CNT-1000	18.26	10.96	57.16	13.62

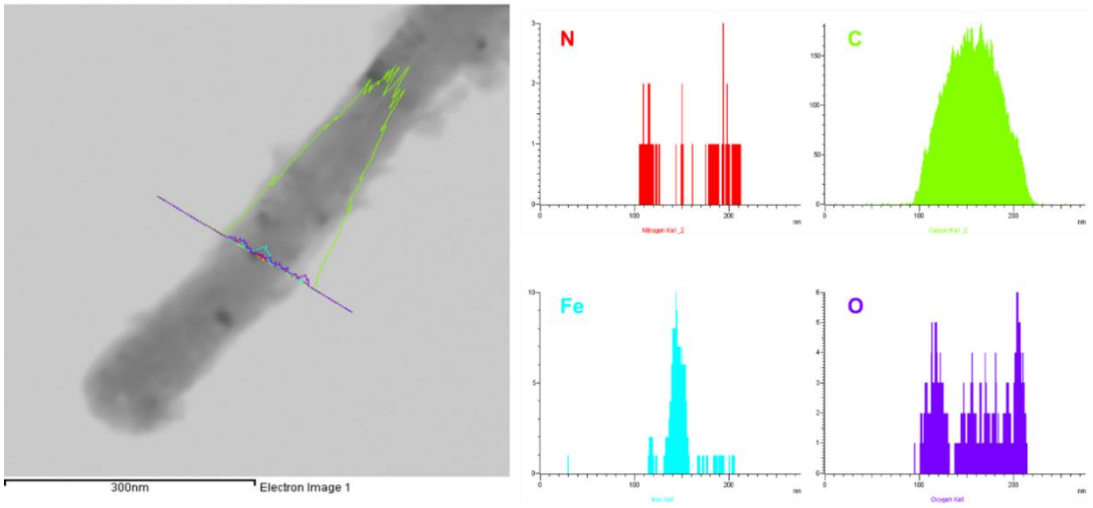

Figure 6-5 TEM image of the NC-CNT-1000 and its corresponding line profile concentration for N, C, Fe and O. The intensive distribution of N, O on the edge, and the peak distribution of Fe and C on center axis of the tubular structure was resulted from the N-doped carbon coating layer on surface of the MWCNTs, and the residual Fe particle in the MWCNTs, respectively.

6.2.2 ORR performance

The ORR activity and stability of CNT-1000 and NC-CNT-1000 was firstly investigated in O_2-saturated alkaline solution. The obtained linear sweep voltammetry (LSV) curves are plotted in **Figure 6-6**(a). LSV curves of NC-1000 are shown for reference. The NC-1000 derived from pure chitosan exhibits the limited current density of less than 5 mA cm^{-2} and onset potential *ca.* 130 mV more negative compared with that of commercial Pt-C. CNT-1000 catalyst exhibits a better reactivity with a diffusion-limiting current density around 6.5 mA cm^{-2}, which is comparable to that of commercial Pt/C. However, the onset potential of CNT-1000 was even more negative than that of the NC-1000 samples, which in turn was more negative than the commercial Pt-C by 200 mV. This behaviour is due to the limited conductivity of NC-1000 and the lack of effective active sites on the CNT-1000 samples. After coating the NC, the as obtained NC-CNT-1000 exhibited a clear improvement in the onset potential showing an obvious diffusion-limiting region below 0.6 V, and a saturated current density ca. 0.2 mA cm^{-2} higher compared with commercial Pt-C. Further inspection reveals that the half-wave potential ($E_{1/2}$) of NC-CNT-1000 has positively shifted by *ca.* 100 mV compared to CNT-1000 catalyst, suggesting a significant decrease in overpotential. The Tafel plots for CNT-1000, NC-CNT-1000 and Pt-C electrodes derived from the LSV results are presented at the potential regions slightly lower than onset potential (**Figure 6-6**b). The Tafel slope of NC-CNT-1000 catalysts visibly decreased from *ca.* 147.2 mV dec^{-1} for CNT-1000 to 85.2 mV dec^{-1} which is much closer to that of Pt/C (79.5 mV dec^{-1}), indicating accelerated ORR kinetics.

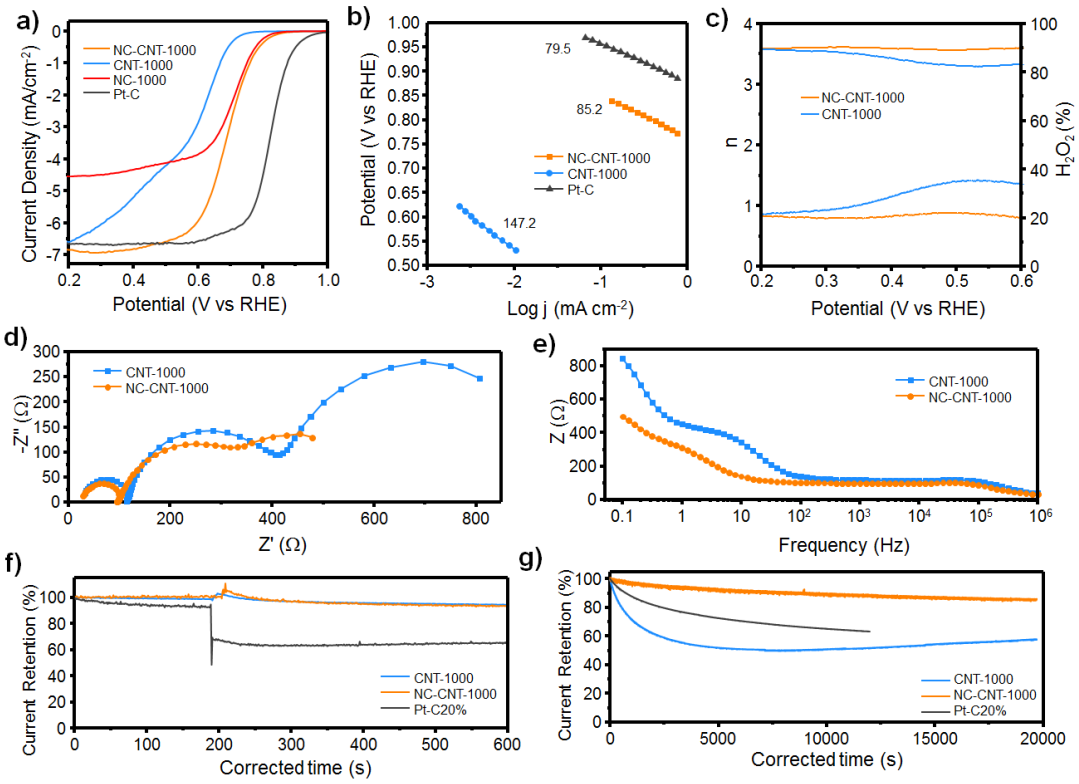

Figure 6-6 ORR performance of the electrocatalysts in KOH electrolyte: (a) LSV curves of different samples in O_2-saturated 0.10 M KOH solution at a rotation rate of 1600 rpm. The scan rate was 10 mV s^{-1}. The result of NC-1000 is also displayed for reference; (b) the corresponding Tafel plots of CNT-1000, NC-CNT-1000 and Pt-C; (c) peroxide yields and electron transfer numbers (n) of the catalysts calculated from the RRDE measurement results in 0.1 M KOH at a rotation rate of 1600 rpm; (d) Nyquist plots and; e) the Bode plots of the samples obtained at voltage near the half-wave potential at the frequency range of 0.01 Hz-10^6 Hz, in O_2-saturated 0.1 M KOH solution at a rotation rate of 1600 rpm. Chronoamperometric response of samples: (f) tolerance against methanol and (g) long-term stability.

Rotating ring-disk electrode (RRDE) was introduced to detect the H_2O_2 yield and calculate the electron transfer number of the catalysts. NC-CNT-1000 has an electron transfer number of *ca.*3.6, which is close to an ideal 4-electron reaction pathway, while the amount of H_2O_2 produced was *ca.* 20%. This is much lower than the CNT-1000 whose yield is close to 30% especially at a high potential range (**Figure 6-6**c). Electrochemical

impedance spectroscopy (EIS) on CNT-1000 and CS-CNT-1000 was carried out at the mixed diffusion region near the half-wave potential to further investigate electrode processes (**Figure 6-6**d, e). At high frequency, despite the less-conductive NC layer on the surface, the NC-CNT-1000 samples showed comparable or even slightly lower charge transfer resistance (*ca.* 20 Ω) compared with CNT-1000. At lower frequency, governed by a mix of charge-transfer and mass-transfer process, however, the difference in resistance was more than 100 Ω. The lower resistance of NC-CNT-1000 at high frequency is probably due to the formation of N-containing active sites promoting electron transfer. At the lower frequency, the decrease of resistance is probably due to the 3D hierarchical structure formed upon hybridising MWCNTs with NC via HTC which remarkably improved the mass transfer.

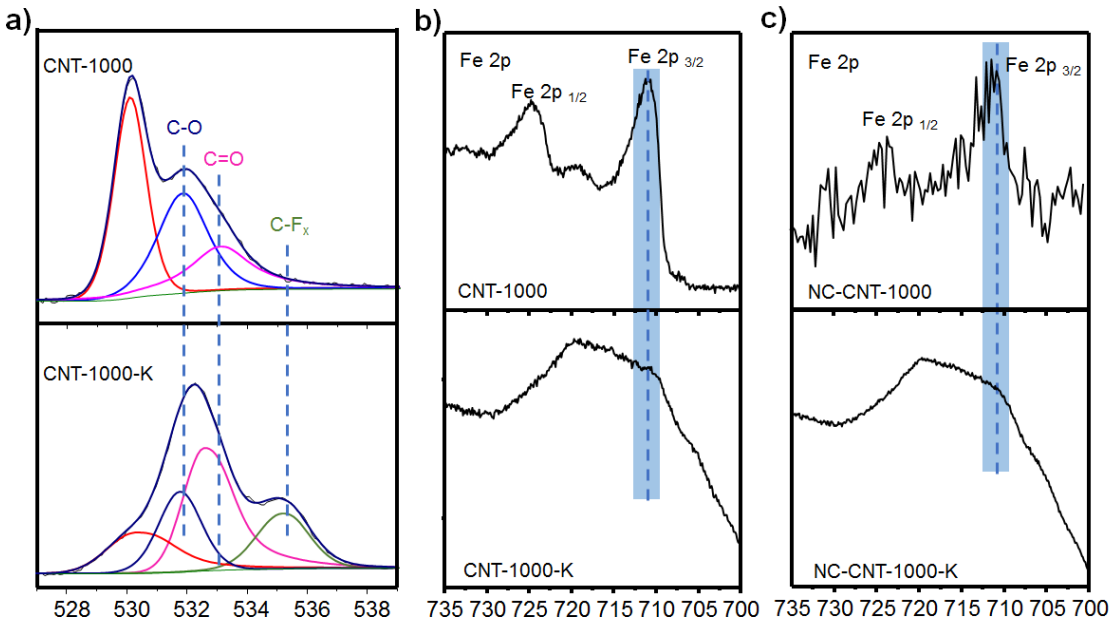

Figure 6-7 (a) The XPS O 1s spectra of CNT-1000 and CNT-1000-K and the high-resolution XPS Fe 2p spectra of (b) CNT-1000 and (c) NC-CNT-1000 before and after long term stability test in 0.1 M KOH. The CNT-1000-K refers to the sample obtained after the stability test.

The superior MeOH tolerance of catalysts were maintained after the NC coating was applied (**Figure 6-6**f). Current-time chronoamperometric responses (**Figure 6-6** g) clearly demonstrate the remarkable improvement in stability after coating MWCNTs with the NC-layer. The potential was set at the mixed diffusion region near half-wave potential. After 15000 s tests, the current retention of the catalysts improved from 60% in the CNT-1000 to 90 % in NC-CNT-1000. The current retention of CNT-1000 decreased dramatically during the first 1000 s, which is probably attributed to the deactivation of Fe-derived active sites on MWCNTs alone. After 5000s, the current retention increased slightly, most probably due to the presence of some oxygen-containing functional groups on the catalyst during the electrochemistry process. This observation is consistent with the XPS results comparing the chemical environment of oxygen in CNT-1000 before and after the stability test (**Figure 6-7**a), the obviously increased ratio of C=O in CNT-1000 after stability test is evidence of the oxygen-containing functional groups on the surface of CNT-1000.

Theoretical and experimental studies showed that the pure MWCNTs possess catalytic activity due to altered charge or spin distribution of the sp^2 panel, in which the flowing free electrons favour the O_2 adsorption and subsequently weakens the O-O bond. Edges and topological defects (pentagonal, zigzag edge, *etc*.) with unpaired electrons and carboxylic groups also facilitate the O_2 trapping and electron transport, and results in an improved catalytic activity.[25, 80-84, 86, 87, 228] In this work, the Fe sites located either inside the tubular structure or at the outer wall further contribute to the ORR activity.

In NC-CNT-1000, the N-derived active sites had a synergistic effect along with Fe on the MWCNTs and remarkably improved the catalytic activity. To demonstrate the effect of Fe on the ORR activity, NC-CNT-1000 was also evaluated in 0.1 M KOH containing 10 mM KCN, in which iron strongly coordinates with CN- ions resulting in loss of catalytic activity.[194] The observed decrease in the catalytic activity revealed the contribution of Fe to the performance of NC-CNT-1000 catalysts in combination with the nitrogen-doped carbon layer. (**Figure 6-8**).

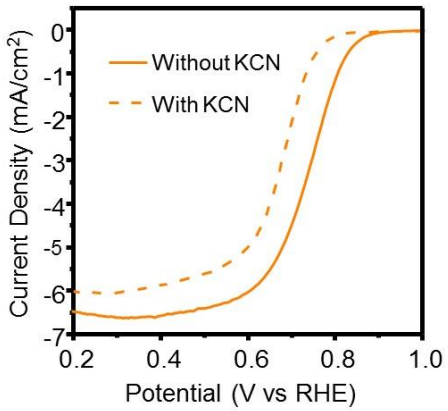

Figure 6-8 Linear sweep voltammetry of NC-CNT-1000 at 10 mV s^{-1} in the presence of oxygen at 1600 rpm in 0.1 M KOH with and without cyanide ions (10 mM KCN). The reduction of saturated current density and half-wave potential with existing KCN illustrated the contribution of Fe-derived active sites to the ORR activity of the sample.

Long-term stability test demonstrated that CNT-1000 can be easily degraded in comparison with NC-CNT-1000. This means that the ORR active sites on the pure MWCNTs surface which are composed of iron carbide, oxygen-contained functional groups and topological defects are more stable in conjunction with the grafted layer of the nitrogen doped carbon (**Figure 6-6**g). There are two possible reasons for the degradation of the active sites on pure MWCNTs: (i) the oxidation of the carbon matrix leading to the loss of defects and edges; (ii) deactivation of the active sites, resulting from

the poisoning effect due to H_2O_2 formation during the ORR process. It has been reported that the oxidation of carbon nanotube side walls usually happens at high voltage potential, therefore it is unlikely to happen at the working voltage of ORR.[229] The most probable reason should be the poisoning effect that the produced H_2O_2 has on the Fe-derived active sites on the surface of the MWCNTs. The interaction of the active sites with H_2O_2 was indeed proved to deactivate the active sites.[230] The introduction of NC layer protects the Fe-derived active sites from direct contact with H_2O_2 and thus the electrocatalyst maintains its activity and exhibits an improved long-term stability.

XPS performed on the catalysts before and after the long-term stability test supported the fact that indeed a more stable chemical Fe environment exists in the NC-CNT-1000 than that in CNT-1000. After the long-term stability test, the peak position of Fe2p $_{3/2}$ in CNT-1000 showed a positive shift of *ca.* 0.7 V, while NC-CNT-1000 hardly exhibited any obvious shift in Fe2p $_{3/2}$ peak position (**Figure 6-7**b, c). The shift in CNT-1000 is due to the change of surrounding bonds of Fe, such as local strain.[231] Although it is difficult to subtract the exact content of each atom due to the interference of Nafion added during electrode preparation, and that the interference of the F peak in Nafion which is close to the Fe2p peak, the shift of the peak position indicates the corrosion of the chemical bond during the process[231]. These results confirm that indeed the NC layer protects the function of Fe-derived active sites while protecting them from being poisoned/deactivated.

The ORR performance was also investigated in acid electrolyte, where normally carbon-derived materials fail to perform[55]. In an acid electrolyte, the NC-1000 derived from pure chitosan exhibits a limited current density of less than 2.5 $mAcm^{-2}$ and onset potential

lower than 0.6 V. On the other hand, CNT-1000 hardly demonstrated any catalytic activity at tested voltage range (**Figure 6-9**a). However, the NC-CNT-1000 demonstrated a remarkable improvement in both onset potential and saturated current density. The onset potential of NC-CNT-1000 is *ca.* 200 mV more positive than NC-1000, while the current density at 0.1 V is comparable with commercial Pt-C. Thus, the synergistic effect between

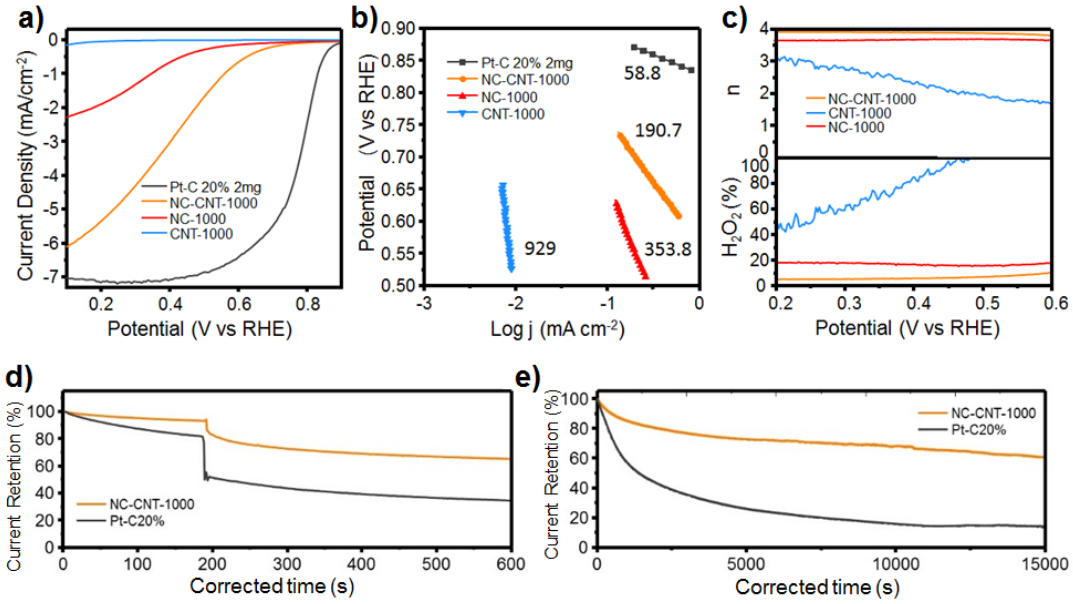

Figure 6-9 ORR performance of the electrocatalysts in 0.1 M $HClO_4$ electrolyte: (a) LSV curves of different samples in O_2-saturated 0.10 M $HClO_4$ solution at a rotation rate of 1600 rpm. The scan rate was 10.0 mV s^{-1}. The result of NC-1000 is also displayed for reference; (b) the corresponding Tafel plots; (c) peroxide yields and electron transfer numbers of the catalysts calculated from the RRDE measurement results in 0.1 M $HClO_4$ at a rotation rate of 1600 rpm. Chronoamperometric response of samples: (d) tolerance against methanol and (e) long-term stability in 0.1 M $HClO_4$.

NC and MWCNT is clearly demonstrated. This has remarkably improved the catalytic activity of the composite (NC-CNT-1000) in an acid medium. This synergistic effect is confirmed by the Tafel plot (**Figure 6-9**b). At the same potential range, slightly lower than onset potential, the Tafel slope of NC-CNT-1000 catalysts decreased from *ca.* 353.8 mV dec^{-1} in NC-1000 to 190.7 mV dec^{-1} which is much closer to that of Pt/C, indicating

accelerated ORR kinetics. The Tafel plots for CNT-1000, however, is almost vertical to the X axis, demonstrating its inert activity towards ORR in acid. The electron transfer number of NC-CNT-100 is close to 4, while the H_2O_2 yield is lower than 5%. (**Figure 6-9**c). MeOH tolerance in **Figure 6-9**(d) proved the superior tolerance of NC-CNT-1000 compared with commercial Pt-C in acid. Current-time chronoamperometric responses (**Figure 6-9**e) tested at the mixed diffusion region clearly demonstrated the superior stability of NC-CNT-1000 compared with commercial Pt-C. After 15000 s tests, the current retention of the NC-CNT-1000 maintained more than 60%, much higher than that of commercial Pt-C which is lower than 20%. The MeOH tolerance and long-term stability of CNT-1000 was not recorded due to its inert activity towards ORR.

6.2.3 Conclusion

In this chapter, an effective strategy has been developed to improve the ORR activity and durability of the MWCNTs by introducing a layer of amorphous nitrogen doped carbon using an abundant and renewable precursor, chitosan. The NC coating layer remarkably enhanced the ORR catalytic activity in terms of both catalytic activity and long-term stability. The catalytic activity was improved because: (i) the NC introduced N-derived active sites, which promote electron transfer. (ii) the NC layer protects the Fe-derived active sites from being poisoned by by-products during the ORR process, such as H_2O_2; (iii) the 3-D structure formed during the hydrothermal treatment promotes mass and electron transfer to the benefit of the ORR reaction. Further advantages of this approach are the use of chitosan which is sustainable and has a much lower cost compared with

other complicated carbon precursors and noble metals. In addition, this process is easy to scale-up in an either batch or continuous process.

7 Oxygenophilic ionic liquids promote the oxygen reduction reaction in Pt-free carbon electrocatalysts

7.1 Introduction

In addition to engineering the carbon catalyst's physicochemical properties, optimizing the interface where the oxygen reduction reaction takes place represents another, yet unexplored, opportunity to boost its electrocatalytic activity, as this is where phenomena such as fast electron transport, high O_2 solubility and interaction with the electrolyte occur.

ILs have gained remarkable attention as relative low-cost green media for energy conversion reactions compared with currently commercialized Pt. The IL layer can favour O_2 transport towards the catalyst's surface, preserve the active sites from water covering and protect the Pt from oxygenated species or poisoning, leading to an impressive activity enhancement. [147, 180, 182, 232, 233]

Here, a new concept of interfacial control was presented for such key processes governing the ORR at the triple point between the electrocatalyst, electrolyte and gas phase. In the first part of this study, a novel concept of microenvironment manipulation into metal-free graphite nanocarbon catalysts was introduced to boost the ORR performance and achieve an improved ORR stability. This concept is based on using hydrophobic ILs to modify the surface of nanocarbon electrocatalysts *via* a uniform and thin layer. The ILs possess several advantages, including a high O_2 solubility while having a hydrophobic nature to allow an interconnected water pathway, and sufficient $H^+/H_3O^+/OH^-$ conductivity. Consequently, the IL layer formed at the triple-phase interface between solid-liquid and

gas will induce more favourable three-phase contact points at the active sites, as illustrated in **Figure 7-1**. It was demonstrated how such a facile strategy can lead to significant improvements in the ORR performance and stability in both alkaline and acid electrolytes. In the second part of this study, this concept was further extended to prove its general character towards porous Fe-N-C and N-C amorphous carbon catalysts, and conduct in-depth investigations for a better understanding of the underlying mechanisms.

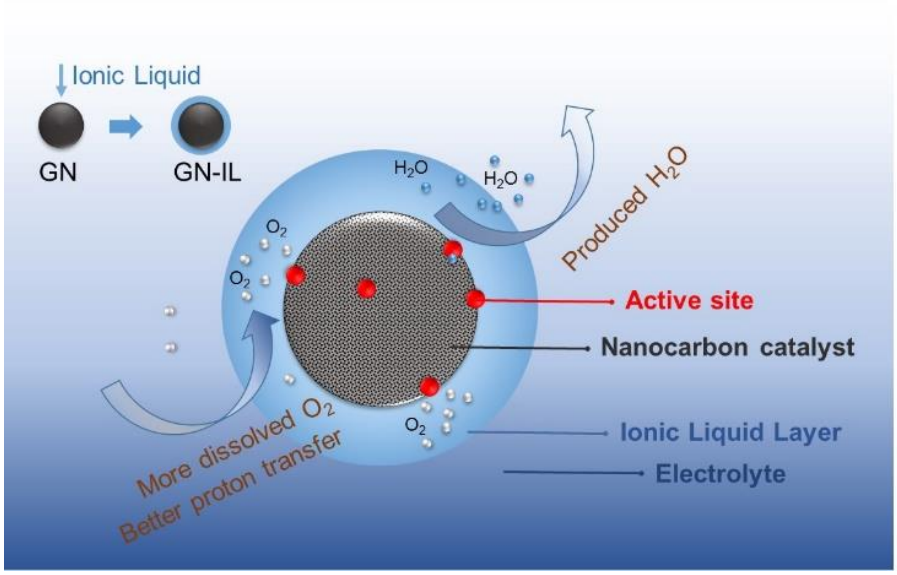

Figure 7-1 Schematic diagram of the synthesis process and the triple-phase interface between solid-liquid and gas.

7.2 Results and discussion

7.2.1 IL modification on graphitic nanocarbon based electrocatalysts

1-butyl-3-methylimidazolium bis(trifluoromethanesulfonyl) imide (IL1), a hydrophobic but aprotic IL, has been selected to modify the catalyst's interfacial microenvironment of a nitrogen doped graphene (GN) electrocatalyst prepared via a simple hydrothermal treatment of graphene and urea as described in detail in the experiment details. This

composite was denoted GN-IL1. The TEM micrographs of the graphene flakes before and after IL modification are shown in **Figure 7-2**(a, b). The micrographs are similar, indicating a uniform deposition of an ultra-thin IL layer onto the surface of the GN. The interaction between the IL and GN can take place via static-assisted CH-π hydrogen bond interaction as previously reported in the literature.[234-237]

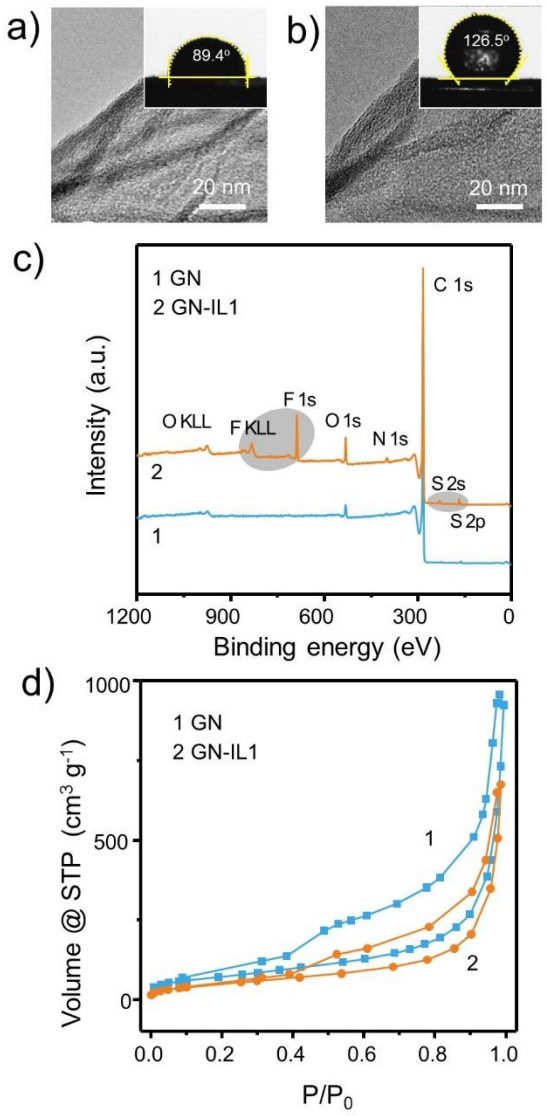

Figure 7-2 TEM images of (a) GN and (b) GN-IL1. The inset images show the static water contact angle measurements, respectively. (c) The XPS surveys and (d) N_2 sorption isotherms of GN and GN-IL1.

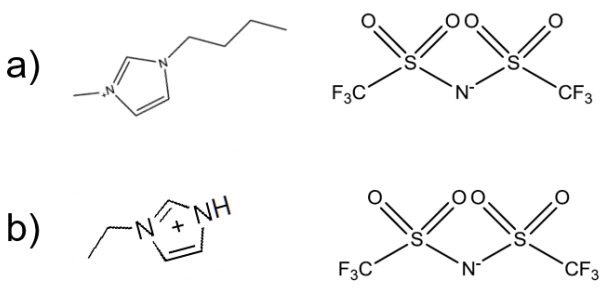

Figure 7-3 Chemical structure of (a) 1-butyl-3-methylimidazolium bis(trifluoromethanesulfonyl) imide ($[C_4C_1im][NTf_2]$), and (b) 1-Ethylimidazolium bis(trifluoromethylsulfonyl) imide ($[C_2im][NTf_2]$).

Table 7-1 XPS results of GN, GN-IL1, and GN-IL2**.**

Sample	Atom Species (at. %)			
	N	N1 (Pyridinic-N)	N2 (Quaternary-N)	N3 (Oxidized-N)
GN	0.6	398.55 eV 42	400.43 eV 24	401.7 eV 34
GN-IL1	1.2	398.15 eV 12	399.29 eV 26	402 eV 62
GN-IL2	0.9	398.83 eV 46	400.17 eV 12	401.62 eV 42

Water contact angle measurements showed a clear increase from 89.4º to 126.5º after the introduction of hydrophobic ILs (insets in **Figure 7-2**a, b). In addition, XPS measurements reveal a substantial amount of F (3.5 at%) and S (0.7 at%), as well as a higher O (3.6 at%) and N (1.2 at%) amounts after the IL modification, arising from the anions of IL1 (**Figure 7-2**c, **Figure 7-3**a). The total nitrogen content of GN-IL1(1.2 at. %) is higher than that of GN (0.6 at. %), while both can be assigned to three dominant configurations: pyridinic-N (ca. 398.55 eV), quaternary-N (ca. 400.43 eV) and oxidized- N (ca. 401.70 eV), respectively (**Table 7-1**).[10] The porosity and specific surface area (SSA) of GN before

and after IL modification were evaluated using nitrogen sorption (**Figure 7-2**d, **pristine** GN, while the

Table 7-2). The SSA of GN-IL1 decreased by 67.8% compared to the pristine GN, while the

Table 7-2 Specific surface area and total pore volume of different samples.

Sample	GN	GN-IL1	GN-IL2
SSA (m^2 g^{-1})	258	175	159
Pore volume (cm^3 g^{-1})	0.797	0.675	0.671

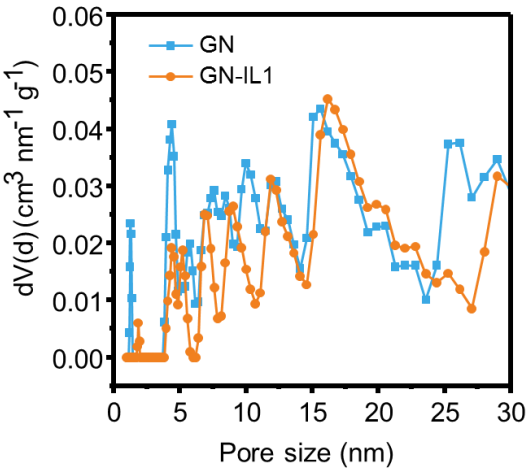

Figure 7-4 Pore size distribution of GN and GN-IL1.

pore volume in GN-IL1 decreased by 84.7% of GN. The decrease in surface area and pore volume from the pristine catalyst to the IL composite further confirms the presence of a thin IL coating onto the surface of porous graphene flakes. In addition, compared with GN, the pore width distribution of GN-IL1 showed a negative shift of 1-2 nm between pore size range of 5-10 nm, which corresponds to the thickness of the ionic liquid layer coated at the electrocatalysts's surface (**Figure 7-4**). The TGA of GN-IL1 under air shows a pronounced mass reduction at a temperature of ca. 460 ºC corresponding to the

decomposition of the IL and another mass loss component at 502 ºC corresponding to the decomposition of the pristine catalyst (**Figure 7-5**a, b). The FT-IR spectrum of the composite material shows additional absorption bands between 1000~1300 cm^{-1} ascribed to SO_2, CF_3 vibration (**Figure 7-5**c, d).

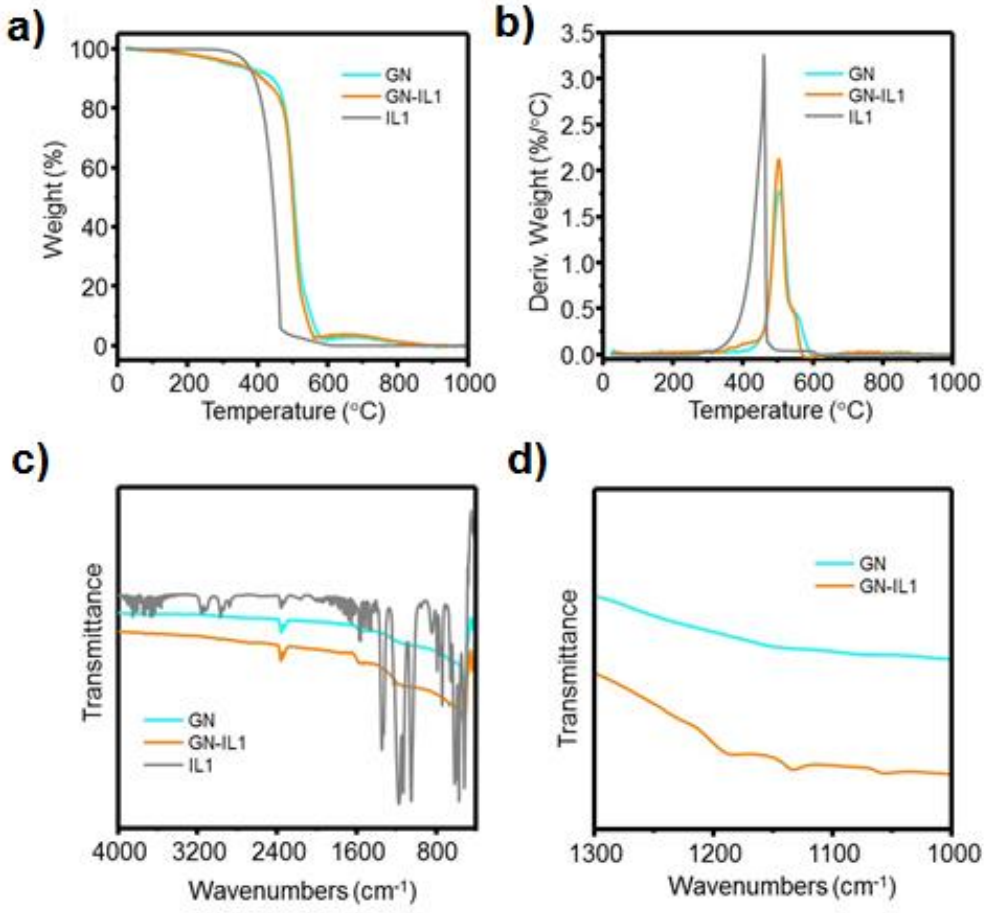

Figure 7-5 (a) TGA and (b) DSC curves of GN, GN-IL1 and IL1. (c) FT-IR spectra of GN, GN-IL1 and IL, and (d) zoomed-in view of FT-IR spectra of GN and GN-IL1 in (c).

The results above confirm a successful and uniform coating of a thin IL layer onto the porous surface of nanocarbon catalysts which can: i) serve as a hydrophobic phase to facilitate the expulsion of water produced during ORR; ii) provide a higher O_2 solubility

and diffusivity to improve the utilisation of active sites; iii) protect the catalyst from oxidation or degradation.

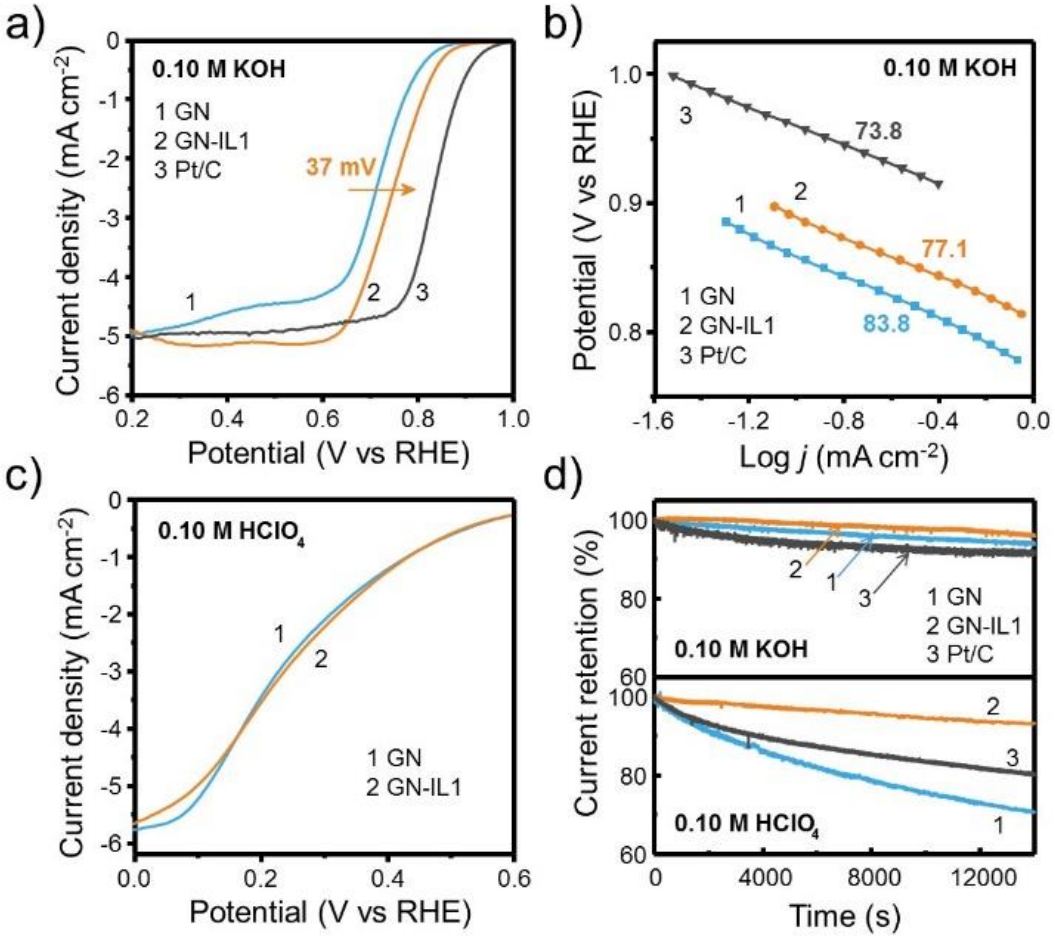

Figure 7-6 ORR performances of the IL-modified GN catalyst. (a) LSV curves obtained in O_2-saturated 0.10 M KOH solution, (b) corresponding Tafel plots derived from the LSV results. (c) LSV curves obtained in O_2-saturated 0.10 M $HClO_4$ solution. The rotating rate was 1600 rpm, with a scan rate of 10 mV s^{-1}. (d) Current−time chronoamperometric responses of different samples in alkaline or acidic conditions. The catalyst loading for all tests was ca. 0.285 mg cm^{-2} (IL was not included).

The ORR activity was firstly investigated in O_2-saturated alkaline solution (0.10 M KOH) using a rotating-ring disk electrode (RRDE) with a rotation rate of 1600 rpm and a scan rate of 10.0 mV s^{-1}. A commercial Pt/C catalyst (20 wt %, Sigma) was also measured under the same conditions for comparison. The obtained linear sweep voltammetry (LSV)

curves are plotted in **Figure 7-6**a. The pristine GN catalyst exhibits good reactivity with a diffusion-limiting current density of about 5.0 mA cm^{-2}, which is comparable to that of commercial Pt/C. This is due to the nitrogen-doping effect and to other topological defective sites on GN.[238, 239] Following modification with IL, the current density has significantly increased from 4.6 mA cm^{-2} to 5.1 mA cm^{-2} at 0.4 V vs RHE, exhibiting a more obvious diffusion-limiting region below 0.65 V. Further inspection of the LSV curve reveals that the half-wave potential ($E_{1/2}$) of the composite GN-IL1 after the IL modification was positively shifted by ca. 37 mV compared to the pristine GN catalyst, suggesting a significantly decrease in overpotential. The Tafel plots for GN, GN-IL1, and Pt/C electrodes derived from the LSV results are presented in **Figure 7-6**b. The Tafel slope has also clearly decreased from ca. 83.8 in the pristine catalyst to 77.1 mV dec^{-1} after IL modification, which is much closer to that of Pt/C, indicating fast ORR kinetics.

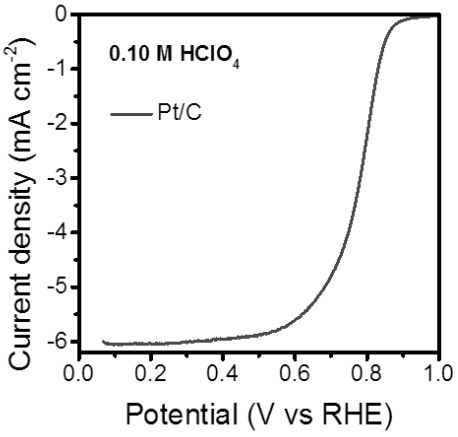

Figure 7-7 LSV curve of commercial Pt/C catalyst in O_2-saturated 0.10 M $HClO_4$ solution with a rotating rate of 1600 rpm. The scan rate was 10 mV s^{-1}.

We have also investigated the ORR performance under acidic conditions (0.10 M $HClO_4$). As shown in **Figure 7-6**c, at high overpotentials, the current densities of GN-IL1 and GN

both approach 6 mA cm^{-2}, which is comparable with Pt/C, showing also a good performance in acid. However, the overpotential is much higher than Pt/C (**Figure 7-7**), while the modification of ILs hardly brings about any improvements. This may be due to the inactivity of nitrogen/defected sites as active sites in acidic condition.[238] IL1 is a typical aprotic IL with a limited H^+ conductivity.[240] Its aprotic character can justify the contrasting ORR performance in alkaline and acidic media obtained otherwise under identical conditions. This hypothesis is supported by a further investigation in a protic IL as presented below. Nevertheless, it can be clearly stated that an improvement in stability in both base and acid can be achieved after the IL modification, as demonstrated *via* current-time chronoamperometric responses (**Figure 7-6**d). The potential was set for the beginning of the diffusion-control region. After 14000 s tests, the current retention of the GN-IL1 composite after the IL modification improved from 94.2% in the pristine GN to 96.2 % in alkaline medium, and from 70.7% to 93.2 % in acid medium, respectively.

The perfluorinated side chains of $[NTf_2]^-$ anions induce hydrophobicity into the catalyst as confirmed by the contact angle measurements shown in **Figure 7-2**(a, b). Besides, it also provides a high affinity to O_2. The O_2 solubility in $[C_4C_1im][NTf_2]$ was reported to be ≈ 2.3 mM,[240] which is much higher compared to aqueous electrolytes (0.10 M KOH ≈1.1 mM,[241] in 0.10 M $HClO_4$; ≈1.2 mM).[183] Consequently, the IL layer on N-doped graphene's surface provides a hydrophobic and oxygenophilic secondary-phase between the solid catalyst and the liquid electrolyte as shown in **Figure 7-1**. The higher oxygen solubility in the IL layer compared to the exterior electrolyte improves the oxygen diffusion towards the catalyst's active sites, increases the residence time, and improves the utilization of active sites, by facilitating a good interaction with its surface.[180]

Furthermore, its hydrophobic nature can expel the formed water from the catalyst's surface, restricting the formation of oxygenated species, thereby freeing up active sites which become highly accessible. Additionally, the IL phase partially replaces the electrolyte as a reaction media and thus can protect the nanocarbon catalysts from external oxidation or poisoning and prevent the catalyst particles from peeling off.[240] All these advantages can optimise the microenvironment between catalysts and aqueous electrolyte, leading to substantially improved activity and stability for ORR catalysis.

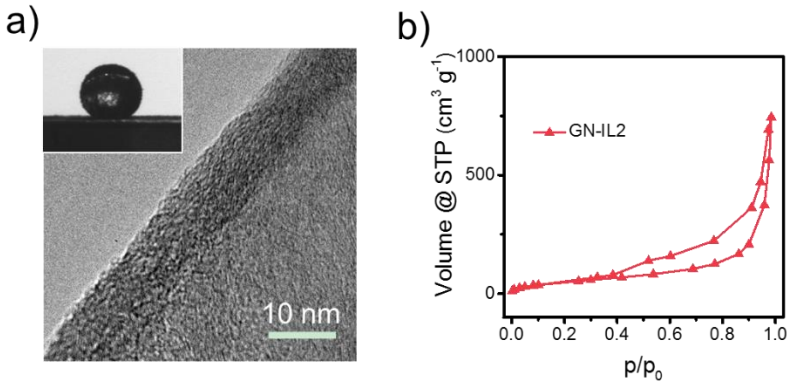

Figure 7-8 (a) TEM image of GN-IL2 and the static water contact angle measurement (inset). (b) N_2 sorption isotherm of GN-IL2.

To further elucidate the role of ILs in metal free ORR electrocatalysis, the $[C_4C_1im][NTf_2]$ has been replaced with another similar IL, 1-ethylimidazolium bis(trifluoromethylsulfonyl) imide ($[C_2im][NTf_2]$) (IL2) (**Figure 7-3**b). This IL is also hydrophobic with a high O_2 solubility, but this time a protic IL, meaning it can facilitate protonic transport via hydronium (H_3O^+) diffusion or proton hopping.[180] The nanocarbon catalyst modified by $[C_2im][NTf_2]$ (GN-IL2) shares a similar morphology, porosity, hydrophobicity, and composition with GN-IL1 (**Figure 7-8**, **Table 7-1**, **pristine** GN, while the

Table 7-2). However, the LSV curves obtained in 0.10 M $HClO_4$ distinctly suggest an enhanced ORR performance of GN-IL2 compared with GN-IL1 with a positive shift in $E_{1/2}$ by ca. 31 mV (**Figure 7-9**a). The improvement of protonic conductivity in IL2 layer near the catalyst surface is in this case critical for such nanocarbon catalysts with a low intrinsic electrocatalytic activity in acid media.

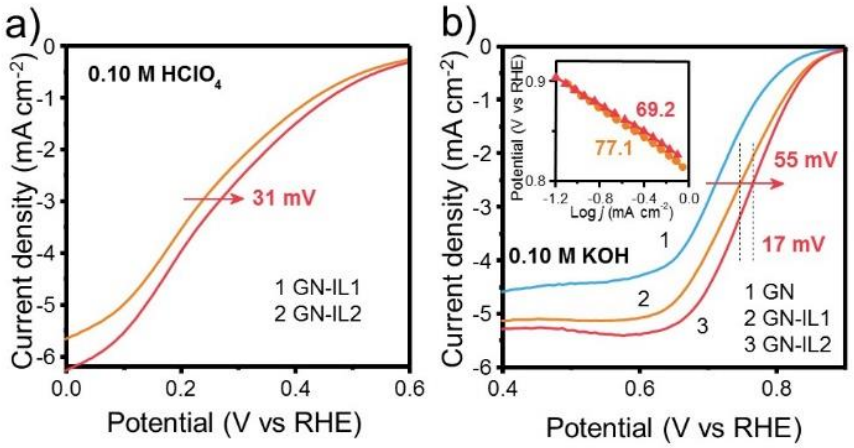

Figure 7-9 Further insights on the IL modification strategy for enhanced ORR catalysis: (a) ORR LSV curves obtained in O_2-saturated 0.10 M $HClO_4$ solution for GN-IL1 and GN-IL2. (b) ORR LSV curves obtained in O_2-saturated 0.10 M KOH solution, and corresponding Tafel plots (inset). The catalyst loading for all tests was ca. 0.285 mg cm^{-2} (IL was not included).

The protic IL modified GN (GN-IL2) also delivers a significantly improved activity and accelerated kinetics in alkaline medium. Its activity is superior to the aprotic IL modified GN, GN-IL1 (**Figure 7-9**b). In this case, the $E_{1/2}$ of GN-IL2 has further increased by ca. 17 mV compared with GN-IL1, and was positively shifted by ca. 55 mV compared with the pristine GN. The Tafel slope further decreased to 69.2 mV dec^{-1}, which is even lower than that of commercial Pt/C catalyst (77.1 mV dec^{-1}). Despite the hydrophobic character of the ILs ascribed to the $[NTf_2]^-$ anions, they can also dissolve a significant amount of water.[180, 240, 242] The water molecules form an interconnected water network in the IL

phase, promoting the H_3O^+/OH^- transport[180, 240] in acid medium, while providing sufficient H_2O reactants for the ORR in alkaline medium. The "N−H" acidic site of the imidazolium cation in $[C_2im]^+$ in IL2 compared with $[C_4C_1im]^+$ in IL1 almost triples the

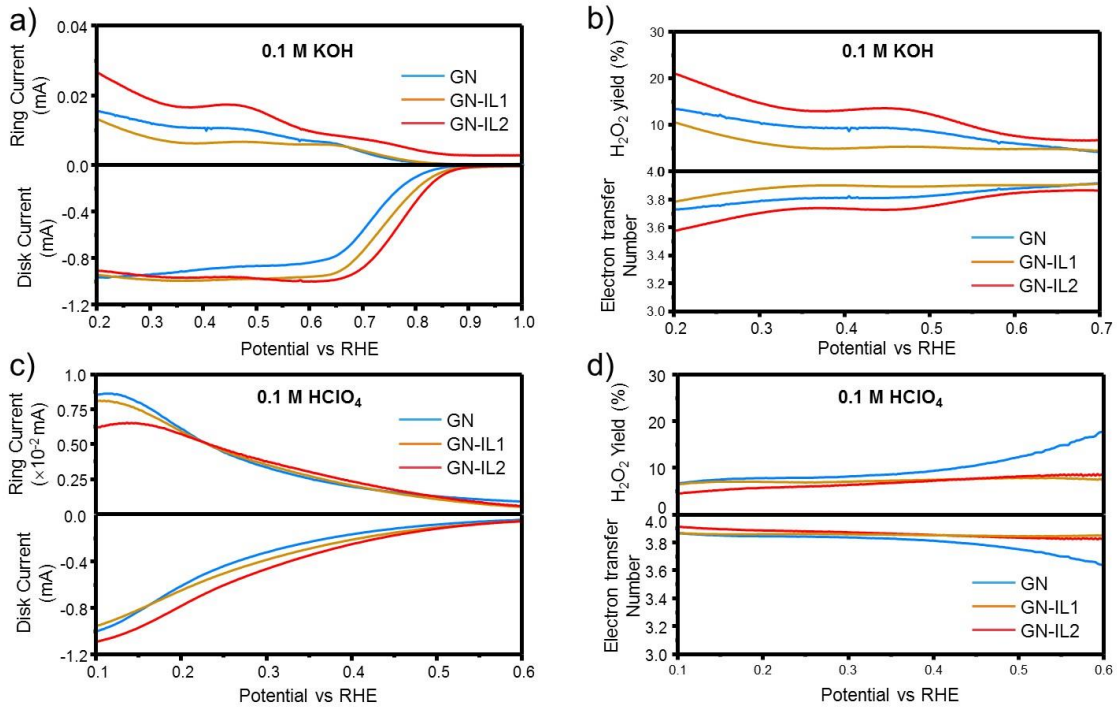

Figure 7-10 (a) RRDE measurement results and (b) peroxide yields and electron transfer numbers of the catalysts calculated from the RRDE measurement results in 0.1 M KOH at a rotation rate of 1600 rpm. (c) RRDE measurement results and (d) peroxide yields and electron transfer numbers of the catalysts calculated from the RRDE measurement results in 0.1 M $HClO_4$ at a rotation rate of 1600 rpm.

mole fraction solubility of water (with large dipole moment) from ca. 0.2 to 0.6, due to hydrogen bonding.[242] The anion is determining the solubility of nonpolar O_2 in ILs, while the cation makes little difference.[243] Therefore, in this case, it is believed that the OH^- transportation is the rate-limiting step. The protic IL2 with a much higher water solubility is more beneficial than the aprotic IL1 with limited water solubility. Rotating ring disk electrode (RRDE) test demonstrated an in-depth study of the reaction pathway (**Figure**

7-10a, c), in which electron transfer number(n) and H_2O_2 yield was calculated and compared (**Figure 7-10**b, d). GN, GN-IL1, GN-IL2 show similar n values of ca. 3.8 in basic medium, and HO_2^- formation lower than 20% for all the samples. In acidic medium, the H_2O_2 yield is even lower than 10%, while the n values keep close to 3.8.

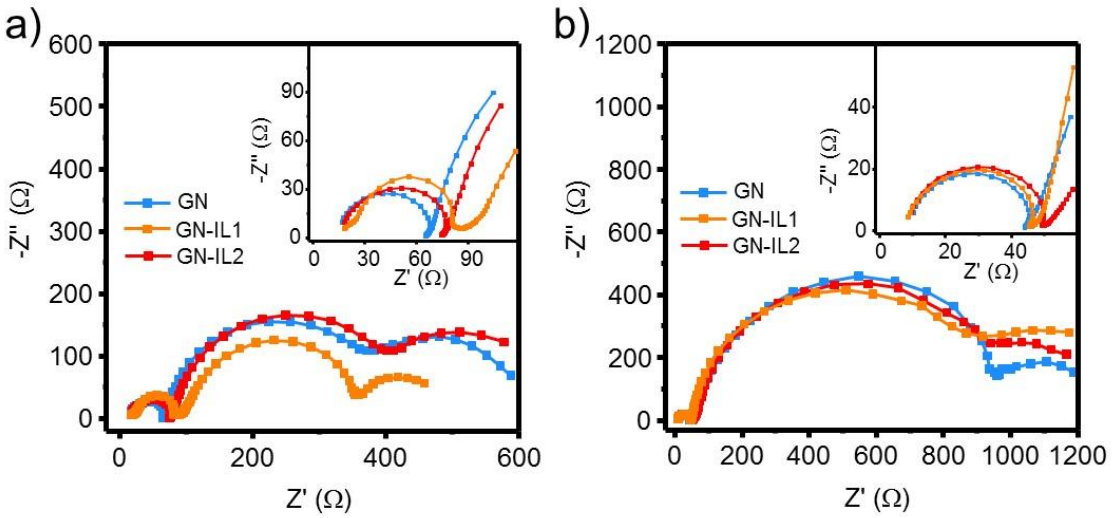

Figure 7-11 Nyquist plots recorded with samples GN, GN-IL1 and GN-IL2 in oxygen-saturated of (a) 0.1M KOH and (b) 0.1M $HClO_4$ at 1600rpm. The frequency range is 0.01 Hz-10^6 Hz.

Electrochemical impedance spectroscopy (EIS) was recorded at the mixed diffusion-controlled region near half-wave potential to further conducted to investigate electrode-electrolyte interface. **Figure 7-11** shows the Nyquist plots of GN, GN-IL1 and GN-IL2. In both electrolytes, GN-IL1 and GN-IL2 showed similar charge transfer resistance at high frequency. However, at lower frequency controlled by a mix of charge-transfer and mass-transfer process, the resistance of ILs coated catalysts appear to be similar or slightly lower compared with the pristine catalyst. This might because that the ionic liquid layer is less electron-conductive compared with pristine catalyst, but is balanced by improved

mass diffusion of oxygen and proton. In order to prove that this strategy can be employed as a general and universal method for improving the electrocatalytic activity of any Pt-

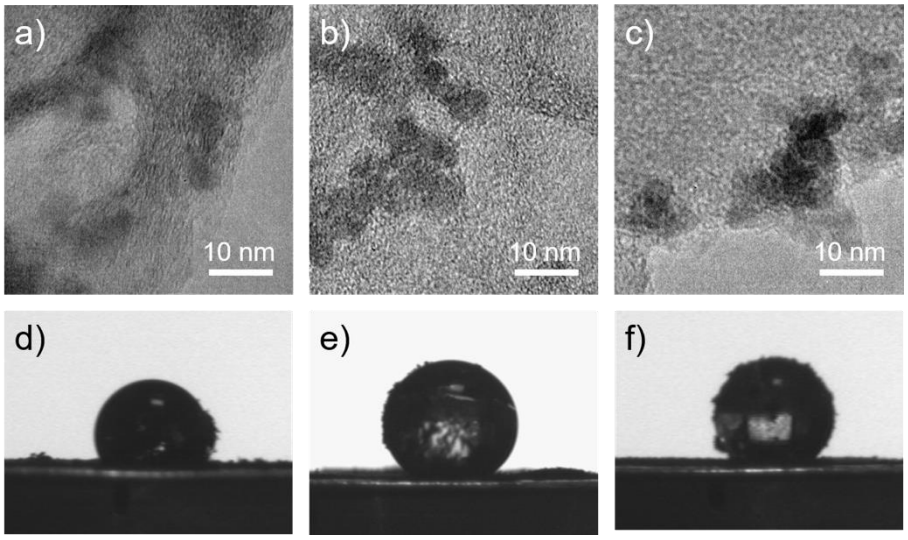

Figure 7-12 TEM images of (a) GNFe, (b) GNFe-IL1, and (c) GNFe-IL2. The static water contact angle measurements of (d) GNFe, (e) GNFe-IL1, and (f) GNFe-IL2.

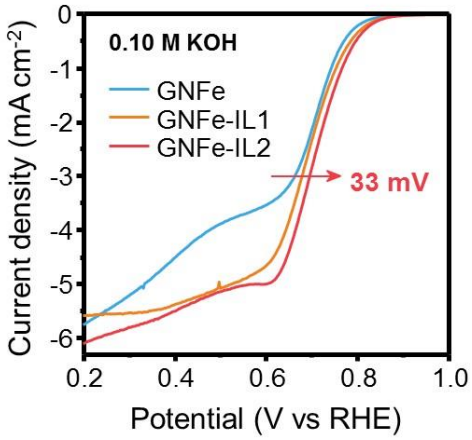

Figure 7-13 ORR LSV curves obtained in O_2-saturated 0.10 M KOH solution for metal-containing samples. The rotating rate was 1600 rpm, with a scan rate of 10 mV s^{-1}. The catalyst loading for all tests was ca. 0.285 mg cm^{-2} (IL was not included).

free elecrocatalysts, an iron/nitrogen-doped graphene (GNFe) was employed instead of GN (**Figure 7-12**). As shown in **Figure 7-13**, the diffusion-limiting current density is

increased above 6 mA cm^{-2} and the $E_{1/2}$ is positively shifted by ca. 33 mV after IL2 modification (GNFe-IL2), indicating similar performance improvement in both metal-free and precious-metal-free nanocarbon catalysts.

7.2.2 IL modification on amorphous nanocarbon based electrocatalysts

1-ethylimidazolium bis(trifluoromethylsulfonyl) imide was selected in this study to modify the TPB microenvironment between electrocatalyst, electrolyte and O_2 molecule. Its chemical structure is depicted in **Figure 7-3**(b). The schematic diagram in **Figure 7-14** shows the TPB interface between solid, liquid and gas phases. The ionic liquid forms a water-equilibrated secondary layer that promotes the mass transfer towards and from the catalyst surface.

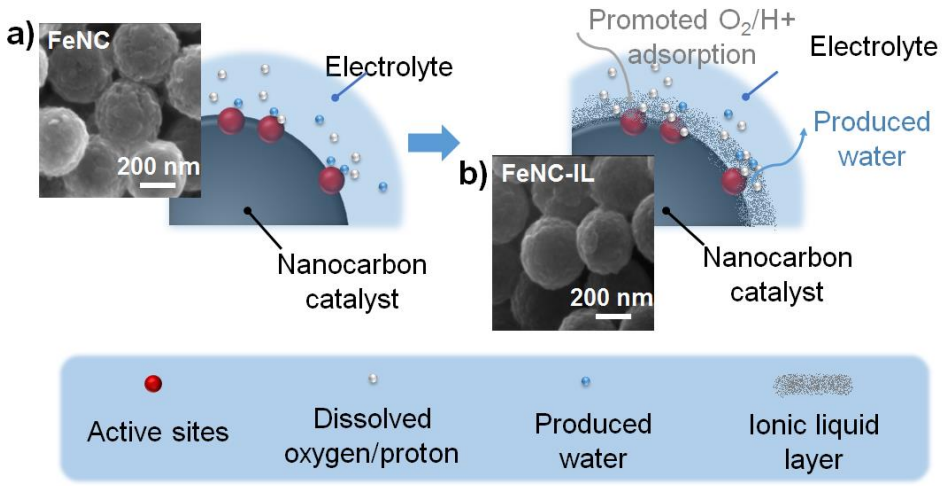

Figure 7-14 (a) Schematic diagram of the triple-phase interface between solid, liquid and gas phases. The inset SEM images correspond to the a) pristine FeNC electrocatalyst and (b) FeNC electrocatalyst after coating with IL layer.

A comparison between the SEM images in Figure 7-14 and the TEM images in **Figure 7-15** before and after the IL coating shows similar carbon spheres with a diameter of ca.

300 nm. However, the surface of the spheres in the inset in **Figure 7-14(**b) is visibly smoother than the rough surface in **Figure 7-14**(a), which provides some evidence of the existence of the coating layer of IL. In fact, in the case of the FeNC catalyst with IL layer (FeNC-IL), it is more difficult to obtain a sharp focus during the SEM characterization operation, which is mainly attributed to the relative low electronic conductivity of the IL layer. This observation directly demonstrates the existence of a thin and homogeneous organic layer on the surface of the carbon electrocatalyst. The presence of the IL layer is further supported by a slight decrease in the mesopore volume, as shown by N_2 physisorption (**Figure 7-16**(a, b)). The specific surface area (SSA, calculated based on the mass of carbon) and pore volume are summarized in Table 7-3. After coating with IL, the negative shift of the peak from pore widths of ca. 7.6 nm to ca. 4.2 nm (**Figure 7-16**(b)), indicate the presence of a thin IL layer of ca. 3 nm, which was consistent with

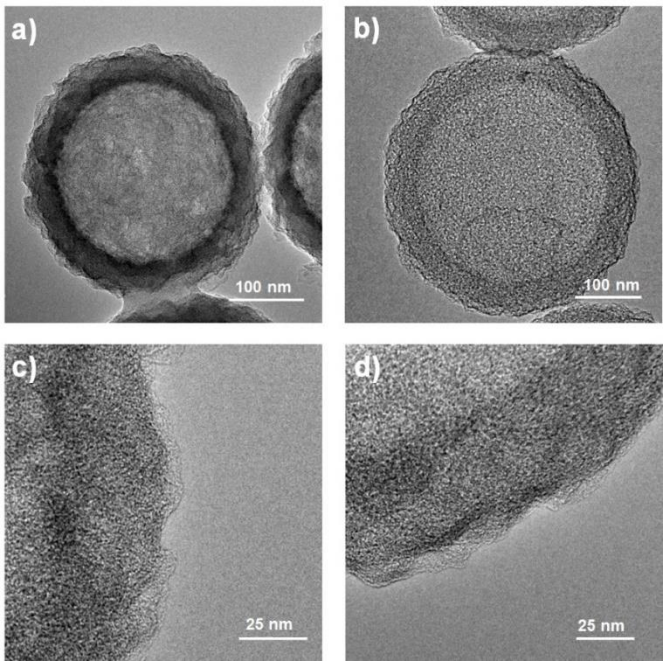

Figure 7-15 TEM images of (a) FeNC, (b) FeNC-IL, and high resolution TEM images of (c) FeNC and (d) FeNC-IL.

the reduction of mesopore volume and consistent with that on the metal free graphite catalysts previous reported in this chapter.[244] On the other hand, as can be seen in **Figure 7-19**, the water contact angle increased from 127º for pristine carbon to 143º for the IL-coated carbon surface, indicating improved hydrophobicity. This result is further quantitatively confirmed by the water adsorption isotherms in **Figure 7-16**(c). The upswing in the water adsorption isotherm of FeNC-IL is displaced by 10% to the higher relative humidity compared to FeNC, demonstrating the increased hydrophobicity introduced by the IL layer, and there is a reduction in the total water uptake from 135% (FeNC) to 122% (FeNC-IL) due to the changes induced in both the textural and surface properties of the catalyst surface after the incorporation of the IL. Both materials show negligible water uptake in the low relative humidity (RH) region, which shows their hydrophobic character.[245, 246]

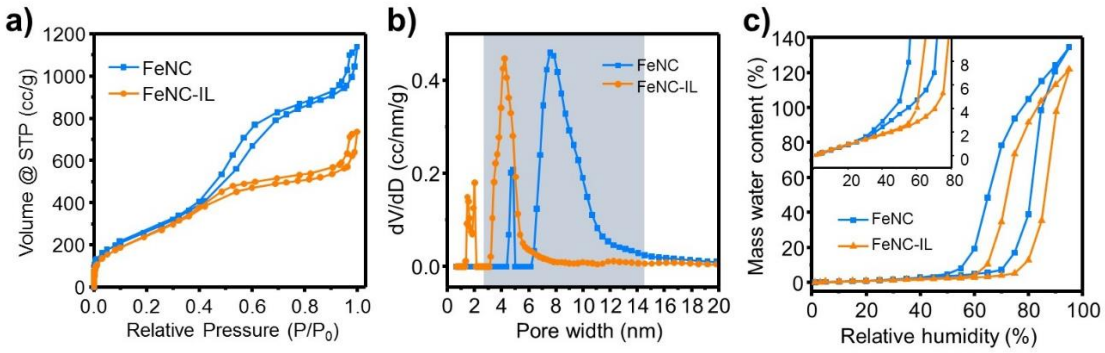

Figure 7-16 (a) N_2 sorption isotherms and (b) QSDFT pore size distributions of FeNC and FeNC-IL from N_2 adsorption isotherms. (c) H_2O vapour sorption isotherm at 20 ºC for samples FeNC and FeNC-IL.

FT-IR was conducted to investigate the surface chemistry of the electrocatalyst (**Figure 7-17** (a)). After incorporation of the IL, additional absorption bands are observed between 1000~1300 cm^{-1}, which can be ascribed to SO_2 and CF_3 vibrations. Strengthened

absorption peaks at 3139, 3075 and 2979 cm^{-1} result from the C-H stretching vibration mode of the imidazole ring and the alkyl chains.[115] The surface composition of the different elements was investigated by means of XPS measurements and is given in **Figure 7-17**b and **Table 7-4**. The N 1s spectra can be deconvoluted into pyridinic-N, Fe-N_x, graphitic-N and oxidized-N at the binding energies of 398.3, 399.6, 400.8 and 403.6 eV, respectively (**Figure 7-20**, **Table 7-5**). Fe-N_x, pyridinic- and quaternary-N are usually considered as effective active sites.[76, 102] Compared to FeNC, the incorporation of IL

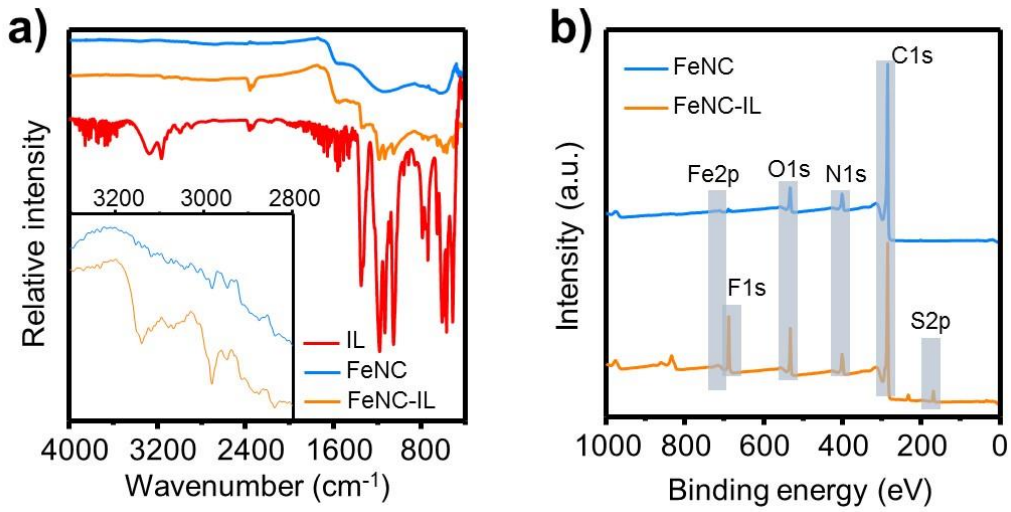

Figure 7-17 (a) FT-IR spectra of the samples. The insets show zoomed spectra in the region 2800~3300 cm^{-1}. The labels of inset X-axis and Y-axis are wavenumber (cm^{-1}) and relative intensity, respectively. (b) XPS surveys of FeNC and FeNC-IL.

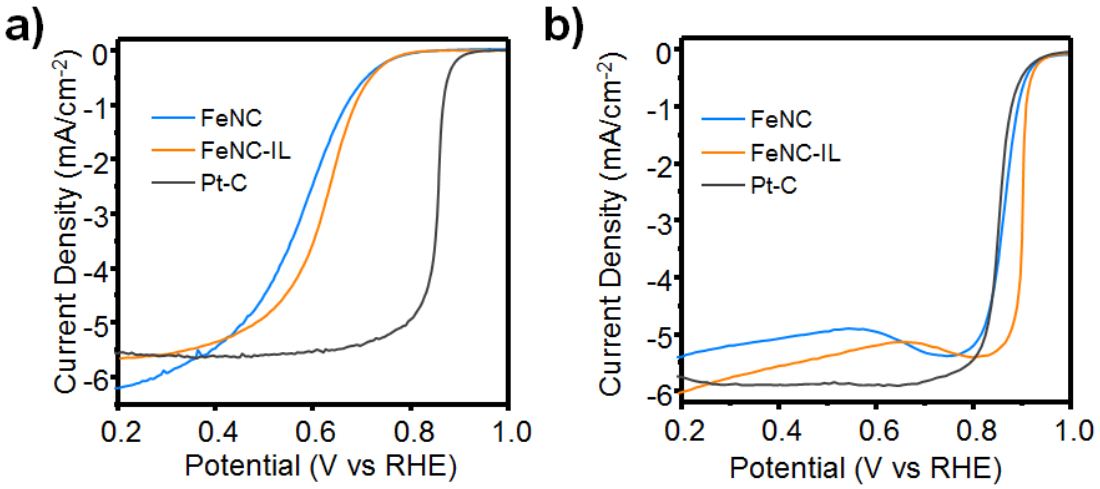

Figure 7-18 (a) LSV curves obtained in O_2-saturated 0.10 M $HClO_4$ solution. (b) LSV curves obtained in O_2-saturated 0.10 M KOH solution. Figures e and f show the ORR performance of the IL-modified FeNC catalyst after iR compensation, the rotating rate was 1600 rpm, with a scan rate of 10 mV s^{-1}.

Table 7-3 Summary of specific surface area and QSDFT calculated total pore volume applied to the N_2 adsorption branch of FeNC before and after ionic liquid coating.

Sample	BET	
	S_{BET}(m^2/g)	V_{total}(cc/g)
FeNC	1114	1.4
FeNC-IL (mass corrected) *	902	0.9

* The specific surface area and pore volume of FeNC-IL are calculated based on the mass of carbon component

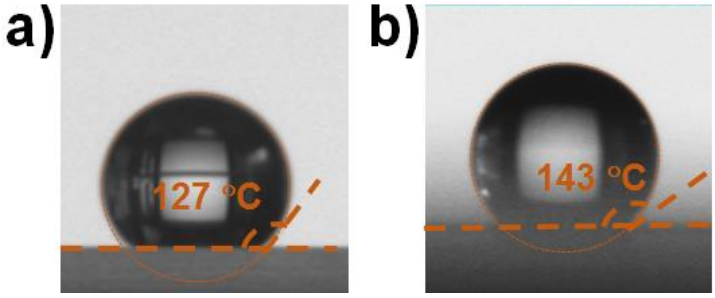

Figure 7-19 Water contact angle of (a) FeNC and (b) FeNC-IL. The decreased water contact angle demonstrated the improvement of hydrophobic surface.

introduces N, S, F and the imidazole ring, which results in the shift of the binding energies of C, O and N components in FeNC-IL (**Table 7-4**). Moreover, new signals have been detected for S, F and an increased ratio of N has been detected in FeNC-IL, which is consistent with the results from FT-IR. This evidence further proves that the IL interacts with the catalyst surface and alters its surface properties.

Table 7-4. Summary of XPS results of the FeNC and FeNC-IL.

	FeNC Binding energy (eV)	**Atom ratio (at%)**		**FeNC-IL Binding energy (eV)**	**Atom ratio (at%)**
C1s	285.37	86.9	C1s	285.28	75.5
O1s	532.52	6.5	O1s	532.20	8.9
N1s	400.70	6.5	N1s	400.59	8.2
Fe2p	711.13	0.1	Fe2p	713.04	0.5
F1s	-	0	F1s	688.32	6.1
S2p	-	0	S2p	168.27	0.8

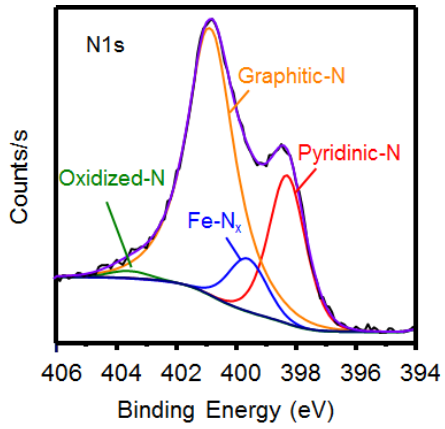

Figure 7-20 The XPS N 1s spectra of FeNC: distributions of pyridinic-N, Fe-Nx, graphitic-N and oxidized-N were illustrated at the binding energy of 398.3 eV, 399.6 eV, 400.8 eV, and 403.6 eV, respectively.

Table 7-5 Summary of XPS N1s spectra from **Figure 7-20**

Sample	N Species (at. %)			
	Pyridinic-N	Fe-N_x	Graphitic-N	Oxidized-N
FeNC	24.7	9.1	64.8	1.4

Oxygen reduction reaction was first measured in 0.1 M $HClO_4$ solution, in which carbon-based electrocatalysts usually fail to perform.[247] iR correction calculated from the EIS results (**Figure 7-21**a) was applied to compensate for the ohmnic potential drop caused by the system resistance.[248, 249] As shown in **Figure 7-18**a, all the electrocatalysts demonstrate comparable limiting current density to that of commercial Pt-C of the same mass loading. Remarkably, the half-wave potential improves with the IL incorporation, from 574 mV for FeNC to 620 mV for FeNC-IL. This value of half-wave potential is comparable to the best Fe, N-doped carbon catalysts reported so far in the literature (**Table 7-6**). Furthermore, the Tafel slope decreases from 87.1 mV dec^{-1} for FeNC to 66.3 mV dec^{-1} for FeNC-IL, which is much closer to Pt-C (56.6 mV dec^{-1}), demonstrating faster ORR kinetics (**Figure 7-22**a). It is worth noting that so far only a few carbon-based materials have provided a comparable ORR performance with Pt-C in acid

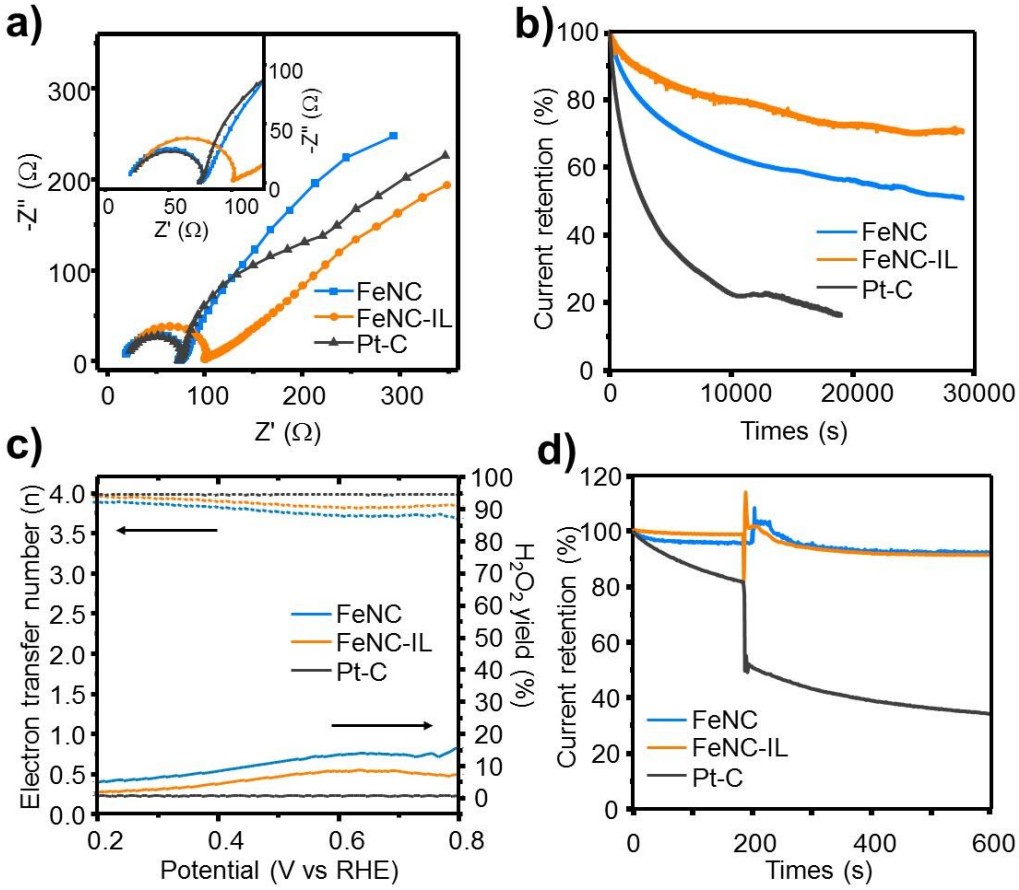

Figure 7-21 ORR performance of the FeNC, FeNC-IL and Pt-C catalysts (same mass loading) in O_2-saturated 0.10 M $HClO_4$ solution. (a) Nyquist plots of the samples obtained at a voltage near the half-wave potential at the frequency range of 0.01 Hz-10^6 Hz. The rotating rate was 1600 rpm. (b) Chronoamperometric response of samples. (c) Peroxide yields and electron transfer numbers of the catalysts calculated from the RRDE measurements. (d) Chronoamperometric response of the catalysts in the presence of methanol.

electrolyte.[247] Long-term stability is another critical issue for metal-based highly-active catalysts due to the acid etching effect and poisonous by-products during the reaction.[250] Herewith chronoamperometric experiments have been performed to test the long-term durability of both FeNC and FeNC-IL. After 25000 s, the FeNC-IL exhibits a current retention of 70%, which is higher than that of FeNC (*i.e.*, 53%), and remarkably superior to that of commercial Pt-C (~ 20 %, **Figure 7-21**b). This improvement can be ascribed to

the hydrophobic properties of the IL layer which impede the produced H_2O and H_2O_2 from building up locally and therefore oxygenate or poison the active sites. RRDE was employed to accurately measure the electron transfer number during the ORR process. As shown in **Figure 7-21**(c), at 0.8 V which is close to the kinetic control region, FeNC-IL exhibits an increase in the electron transfer number from 3.7 (for pristine FeNC catalyst) to 3.9. Meanwhile, the H_2O_2 yield decreases from 15.7 % to 7.3 %. The differences in electron transfer number and H_2O_2 yield between FeNC and FeNC-IL exist through the whole voltage range. At 0.2 V, which is close to the diffusion control region, the electron transfer number of FeNC-IL increases to 3.96, while the H_2O_2 yield decreases to 2 %, which is proof for a typical 4 electron reaction pathway. Moreover, MeOH tolerance of FeNC-IL was demonstrated to be comparable with the pristine FeNC catalysts, and superior to Pt-C (**Figure 7-21**d).

Table 7-6 Comparison of ORR activity of some reported high-performance Fe-N-C catalysts in acid electrolyte (0.1 M $HClO_4$ or 0.05 M H_2SO_4).

Sample	Mass loading (mg cm^{-2})	$E_{1/2}$ of catalyst (V vs. RHE) [#]	$E_{1/2}$ of Pt-C (V vs. RHE)	Electrolyte	Ref
FeNC-IL	0.285	0.620	0.797	0.1 M $HClO_4$	This work
NDC-875_Fe	0.290	0.76	N/A	0.05 M H_2SO_4	[251]
Fe-NMCSs	0.255	~0.73	~0.78	0.1 M $HClO_4$	[252]
Fe2-Z8-C	0.400	0.805	0.822	0.5 M H_2SO_4	[253]
Fe-TA-800	0.200	~0.61	~0.74	0.1 M $HClO_4$	[36]
5% Fe-N/C	0.255	0.735	0.774	0.5 M H_2SO_4	[254]
NDCN-22-900	0.600	0.560	N/A	0.5 M H_2SO_4	[255]
Fe@Fe_3C/C-N	0.250	~0.62	~0.77	0.5 M H_2SO_4	[256]
NG/$Fe_{5.0}$	0.050	~0.454	~0.60	0.5 M H_2SO_4	[257]
pCNT@Fe1.5@GL	0.6	0.820	0.845/0.906*	0.1 M $HClO_4$	[258]

* different values derived from different mass loading of Pt-C
[#] $E_{1/2}$ refers to the half-wave potential of catalyst (V vs. RHE).

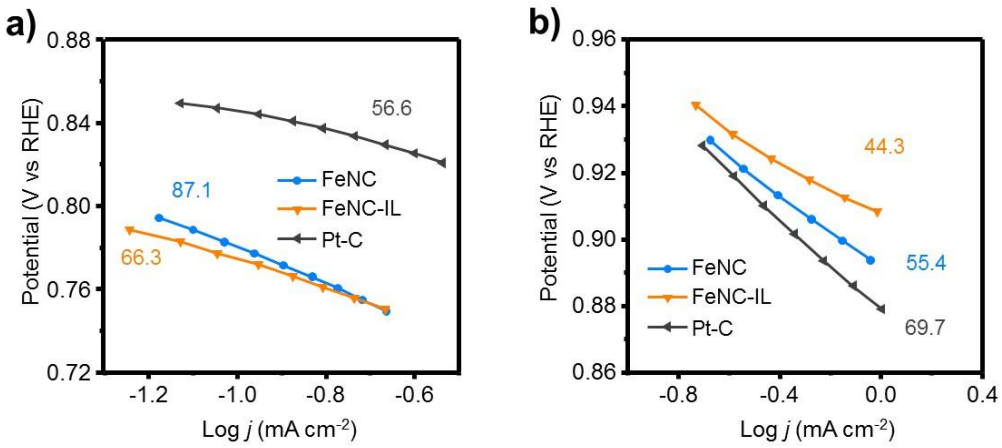

Figure 7-22 Corresponding Tafel plots derived from **Figure 7-18** (a) the LSV curves in O_2-saturated 0.10 M $HClO_4$ solution and (b) LSV curves in O_2-saturated 0.10 M KOH solution (rotating rate = 1600 rpm, scan rate = 10.0 mV s^{-1}).

ORR was also measured in 0.1 M KOH (**Figure 7-18**b, **Figure 7-23**). **Figure 7-18**b shows the LSV curves after the iR correction calculated based on the EIS results (**Figure 7-23**a), the corresponding Tafel plots of iR corrected curves being shown in **Figure 7-22**b. As can be seen in **Figure 7-18**b, both the limiting current density and half-wave potential of the pristine FeNC catalyst match those of commercial Pt-C due to enhanced accessibility to efficient Fe-N and N active sites through the mesoporous structure as has been discussed in the previous work.[194] Meanwhile, the half-wave potential of the FeNC-IL catalyst is 901 mV, which implies a positive voltage shift of 41 mV with respect to that of FeNC (860 mV), and outperforms the Pt-C catalyst (854 mV). The half-wave potential of the pristine FeNC catalyst demonstrated comparable behaviour to many advanced Fe, N-doped carbon catalysts reported in the literature, while this strategy further improves the ORR activity towards an even more positive half-wave potential, which is superior than most of the Fe, N- doped carbon catalysts reported so far (Table 7-7). The Tafel slope in **Figure 7-22**(b) decreases from 55.4 mV dec^{-1} for FeNC to 44.3 mV dec^{-1} for FeNC-

IL, demonstrating faster ORR kinetics after IL coating. Although the process in alkaline medium depends on electron transfer instead of proton transfer, the synergetic effect of

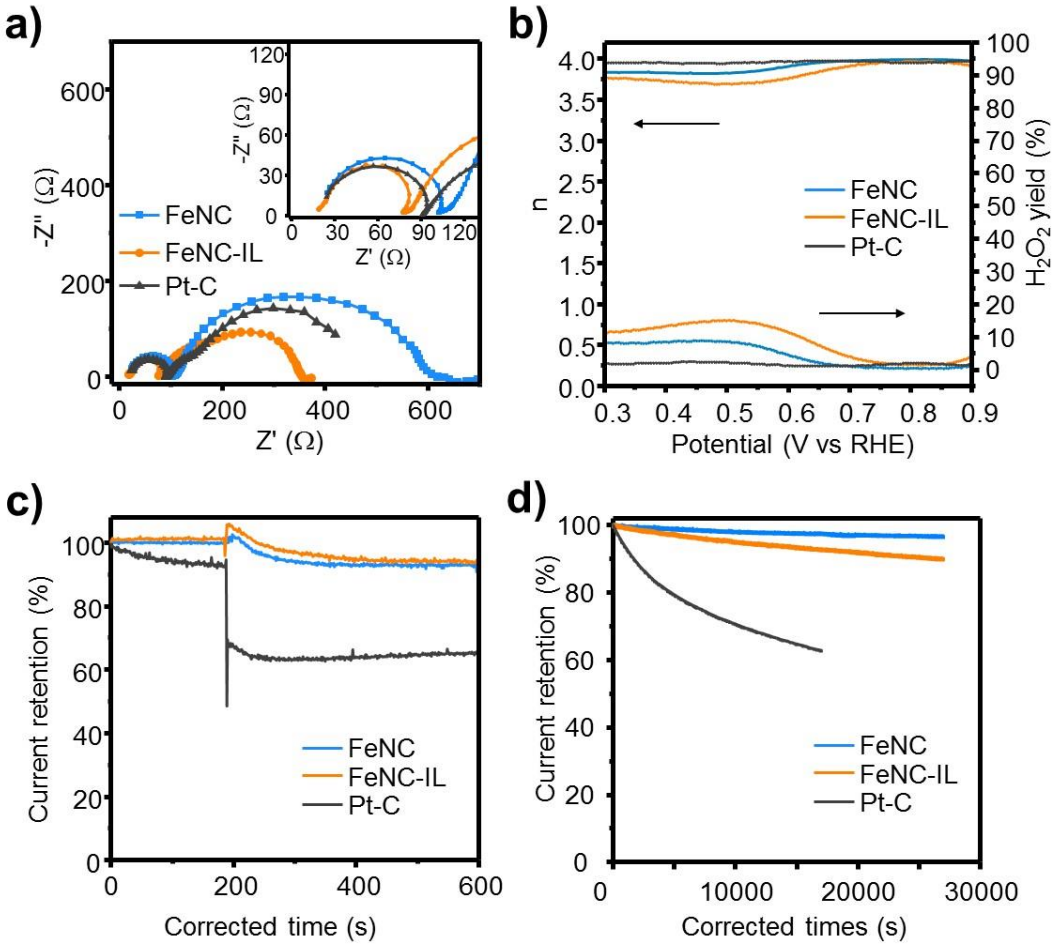

Figure 7-23 ORR performance of the FeNC, FeNC-IL and Pt-C catalysts (same mass loading) in O_2-saturated 0.10 M KOH solution. (a) Nyquist plots of the samples obtained at a voltage near the half-wave potential at the frequency range of 0.01 Hz-10^6 Hz. The rotating rate was 1600 rpm. (b) Peroxide yields and electron transfer numbers of the catalysts calculated from the RRDE measurement results. (c) Chronoamperometric response of samples demonstrating the long-term stability of the samples. (d) Chronoamperometric response of samples in presence of methanol.

oxygenophilic and hydrophobic properties has been shown to improve the ORR performance by promoting the O_2 adsorption and therefore enhancing the overall active sites utilization. The accurate electron transfer number and H_2O_2 yield were analysed by

RRDE (**Figure 7-23**b). At 0.8 V close to the kinetic control region, both the electron transfer number and H_2O_2 yield before and after IL incorporation are similar to Pt-C, which is close to an ideal $4e^-$ pathway. However, after incorporation of the IL layer, the electron transfer number is slightly reduced, and the H_2O_2 yield increased, which probably results from a synergistic effect of improved hydrophobicity and decreased electronic conductivity of the IL surface. Both FeNC and FeNC-IL demonstrated better tolerance to MeOH and superior long-term stability compared to commercial Pt-C (**Figure 7-23**c, d).

All the above results prove that this strategy brings significant improvements to the catalytic activity and long-term stability of carbon-based catalysts. This can be ascribed to the fact that the water-equilibrated secondary phase formed by the IL facilitates the TPB microenvironment as follows: i) it promotes the oxygen adsorption and proton transfer to active centres, thus improving the utilization of the active sites, ii) its hydrophobic nature expels the produced water and prevents it against blocking the active sites, iii) it protects the effective active sites from being poisoned, and therefore improves the long-term stability. Moreover, as previously reported, the nanocarbon surface interacts with the IL through CH-π hydrogen bonding,[244] so that this strategy improves the ORR interface reaction without disturbing the structural properties of the catalyst matrix (e.g. no additional heteroatom doping into carbon matrix). The improvement of ORR catalytic activity in both acid and alkaline electrolyte proves that the oxygen access towards the active centres is the rate-limiting step in ORR in this case. It could be concluded that in the case of the pristine FeNC electrocatalyst the active sites on the nanocarbon catalysts have not been fully utilized because of the limited supply of oxygen

from the aqueous electrolyte, so that the significant role of active sites on nanocarbon catalysts has not been fully performed. Compared with the numerous efforts on improving the active sites on a catalyst's matrix, these findings shed light on a new research pathway to optimize the TPB microenvironment and thus ensure that the existing active sites are fully functional and utilized.

Table 7-7 Comparison of ORR activity of some reported high-performance Fe-N-C catalysts in alkaline media (0.1 M KOH).

Sample	Mass loading of catalyst (mg cm^{-2})	$E_{1/2}$ of catalyst (V vs. RHE)	$E_{1/2}$ of Pt-C (V vs. RHE)	Ref
FeNC-IL	0.285	0.901	0.854	This chapter
GL-Fe/Fe_5C_2/NG-800	0.150	0.86	0.84	[259]
Fe-NMCSs	0.255	0.86	~0.86	[252]
Fe2-Z8-C	0.400	0.871	0.847	[253]
Fe/NMC-11 (0.1 M NaOH)	N/A	0.862	0.872	[260]
NFe/CNs-700-800-NH_3	0.1	0.859	0.816	[261]
FP-Fe-TA-N-850	0.3	~0.81	~0.77	[262]
Fe-TA-800	0.2	~0.8	~0.8	[36]
pCNT@Fe1.5@GL	0.2	0.867	0.845/0.906*	[258]
Fe-ISAs/CN	0.408	0.900	0.842	[263]

*the half-wave potential was evaluated by LSV with different loading amount of 80 and 300 $\mu g_{Pt/C}$ cm^{-2}, and the corresponding half-wave potential are 0.841 and 0.906 $V_{RHE.}$

To further understand the mechanism through which the IL layer facilitates the TPB, various ratios of IL (0.5 and 1.5 times of the original ratio) were further applied to investigate the influence of the IL layer, named as FeNC-IL0.5 and FeNC-IL1.5, respectively. The different IL ratio is supposed to result in the half/ 1.5 times higher IL layer thickness on pristine catalyst compared with FeNC-IL. LSV curves with iR compensation and corresponding Tafel plots calculated based on iR corrected LSV curves in both acid and alkaline electrolytes are shown in **Figure 7-24**(a-d) and **Figure 7-25** respectively. In $HClO_4$ electrolyte (**Figure 7-24**a,b), the FeNC-IL0.5 catalyst exhibits similar onset potential and limiting current density to those of pristine FeNC. Increasing

the IL content in FeNC-IL provides an obvious positive shift from 578 mV in FeNC, 574 mV in FeNC-IL0.5 to 620 mV in FeNC-IL at half-wave potential, with very similar current density under the diffusion-controlled region. However, further increase of the IL content (FeNC- IL1.5) leads to a decrease in both the half-wave potential (590 mV), and the limiting current density at 0.2 V (4.8 mA/cm^2). A similar trend has also been spotted in KOH electrolyte (**Figure 7-24**c,d), the LSV curves after iR correction show also comparable ORR activity for FeNC and FeNC-IL0.5. An increase in the IL ratio in FeNC-IL brings visible improvements on the catalytic activity, with an up-shift of the half-wave potential from 878 mV for FeNC-IL0.5 to 900 mV for FeNC-IL. Further improvement in the IL ratio to FeNC-IL1.5 leads to a reduction of the catalytic activity, as deduced by the similar half-wave potential and decreased limiting current density compared with FeNC-IL.

In both acid and alkaline electrolytes, a visible decrease of the Tafel slope between the pristine and IL coordinated catalysts can be spotted (**Figure 7-25**a, c), indicating increased kinetics after the addition of ionic liquid; however, there is no significant difference within the ionic liquid samples (FeNC-IL0.5, FeNC-IL, FeNC-IL1.5). In alkaline media, a slightly increased content of IL (FeNC-IL0.5, FeNC-IL) leads to a decreased charge resistance due to a synergistic effect of limited electric conductivity and improved mass transfer of oxygen (**Figure 7-25**d). However, as the content of ionic liquid further increases, the charge resistance obviously increased in both acid and alkaline electrolyte (**Figure 7-25**b, d). These results suggest that an excess of IL will bring negative effects, which is most probably a result of the increased thickness of the IL layer which leads to a lower electrical conductivity. Further, this increased water-equilibrated

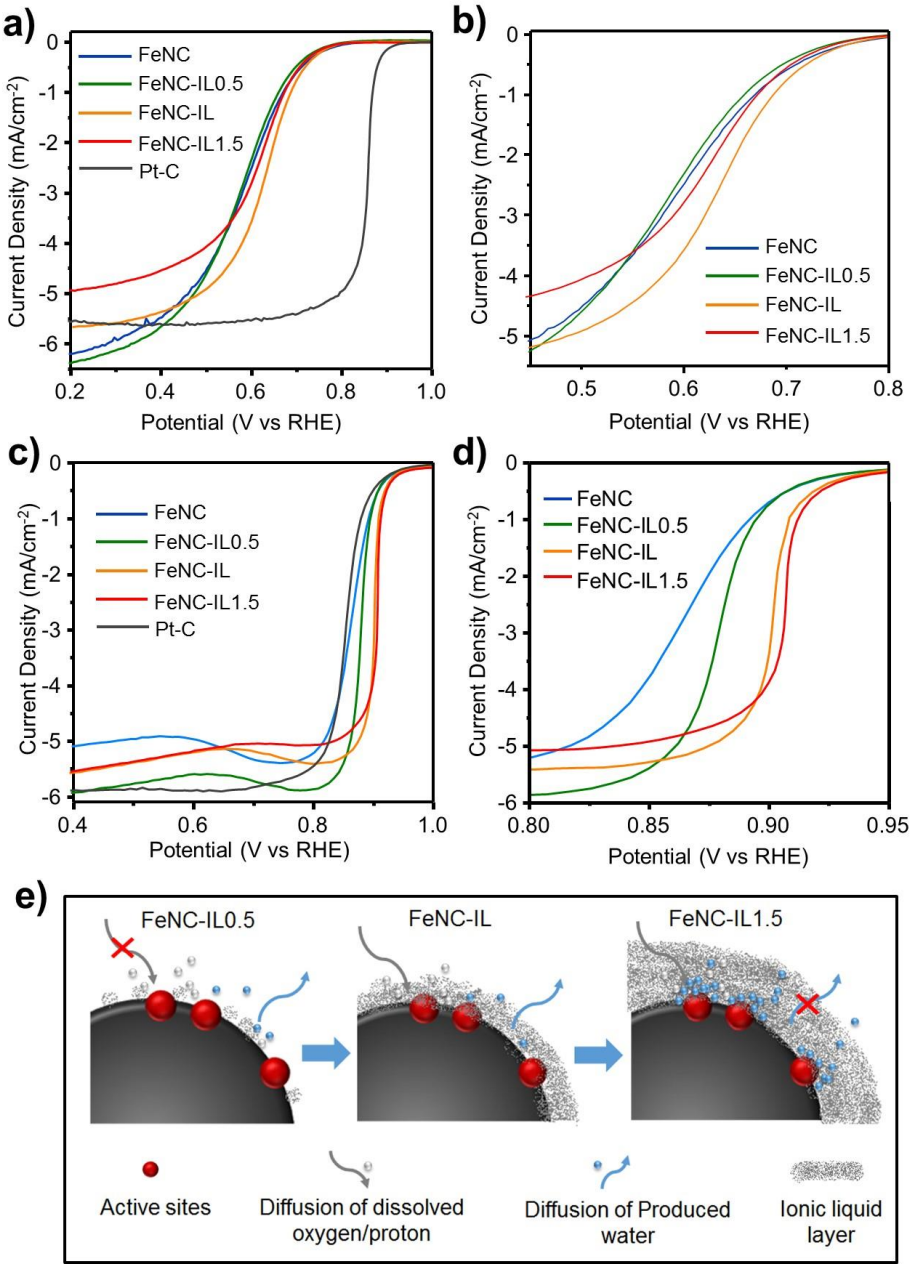

Figure 7-24 ORR performance of the FeNC and IL-modified FeNC catalysts with different ionic liquid content. (a) LSV curves obtained in O_2-saturated 0.10 M $HClO_4$ solution after iR compensation according to the EIS in **Figure 7-25**b, (b) Zoomed in LSV from (a) for a better comparison between FeNC with different IL contents. (c) LSV curves obtained in 0.10 M KOH O_2-saturated solution after iR compensation according to the EIS in **Figure 7-25**d. The rotating rate was 1600 rpm, with a scan rate of 10 mV s^{-1}. (d) Zoomed in LSV from (c) for a better comparison between FeNC with different IL contents. (e) Schematic diagram illustrating the influence of different IL ratios on the TPB microenvironment.

secondary layer, which hinders the electronic transfer, prevents the produced water from diffusing into the electrolyte. The obstructed water molecules therefore accumulate and block the active sites from contacting the reactants such as oxygen and proton (**Figure 7-24**e).

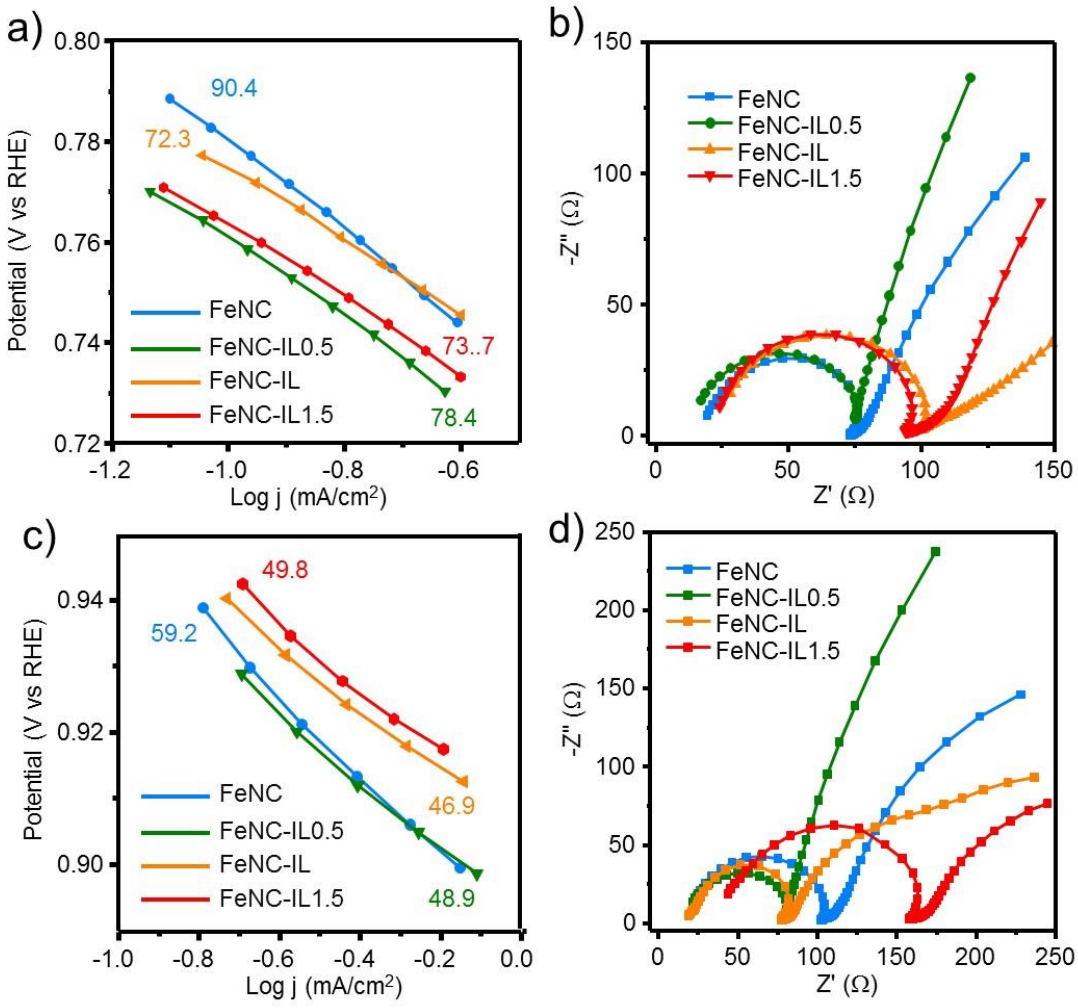

Figure 7-25 Corresponding Tafel plots and EIS spectra of samples: (a) Corresponding Tafel plots derived from the LSV curves (scan rate = 10 mV s^{-1}), and (b) Nyquist plots of the samples obtained at a voltage near the half-wave potential in O_2-saturated 0.10 M $HClO_4$ solution (rotating rate = 1600 rpm). (c) Corresponding Tafel plots derived from the LSV curves (scan rate = 10 mV s^{-1}), and (d) Nyquist plots of the samples obtained at a voltage near the half-wave potential in O_2-saturated 0.10 M KOH solution (rotating rate = 1600 rpm).

This investigation further elucidates the role of the IL in ORR electrocatalysis: the perfluorinated side chains of $[NTf_2]^-$ anions in the IL provide a high affinity for O_2. The solubility of O_2 in the ionic liquid with $[NTf_2]^-$ is *ca.* 2.2 mM,[240] which is almost twice that in aqueous electrolytes (*ca.* 1.1 mM in 0.10 M KOH[264] and *ca.* 1.2 mM in 0.1 M HClO4[183]). The IL layer on the catalyst surface facilitates a higher O_2 diffusion compared with exterior aqueous electrolytes, and thus increases the residence time, intensifies the O_2 diffusion to the active centres, and consequently improves the utilization of the active sites which facilitates an improved interface reaction.[153] Furthermore, the extra "N−H" acidic site of the imidazolium cation in $[C_2im]^+$ in the IL facilitates the water mole fraction solubility (ca. 0.6). This hydrogen bonding largely determines the water solubility in the IL structure.[265] It has been reported that the dissolved water at this mole fraction formed an interconnected through structure in the IL layer that facilitated the transportation of the produced water so that it does not accumulate and block the active sites.[180] When the pathway was enlarged by the thicker IL layer, the water molecules expulsion was indirectly hindered, so that the balance between the production and transportation of the water molecules was broken. Therefore, in both alkaline and acid electrolyte, the hindered water molecules stay at the surface of the active site reducing the accessibility of the reactants (protons/electrons, O_2, etc) to the active centres, so that the catalytic activity of FeNC-IL1.5 decreases compared to FeNC-IL. Moreover, the IL layer plays a role as a reaction medium that partially replaces the aqueous electrolyte and thus can protect the nanocarbon catalysts from being or poisoned by exterior aqueous electrolyte (0.1 M $HClO_4$ or 0.1 M KOH).[240] Considering the benefits and side-effects of the IL layer, the IL ratio in the system should be carefully controlled, so that those advantages can be

maximized to optimize the TPB microenvironment and bring about a substantially improved ORR catalytic activity and stability.

NMR measurements have been conducted to investigate the stability of the ionic liquid layer on the nanocarbon surface. Both $HClO_4$ and KOH electrolytes before and after a long-term stability test for FeNC and FeNC-IL1.5 were collected, condensed *via* evaporation, and then analysed by NMR. After the long-term stability test in both alkaline and acid electrolyte, the electrolytes of FeNC and FeNC-IL1.5 demonstrated a similar composition (**Figure 7-26**a-d), while the spectra of FeNC-IL1.5-$HClO_4$ and FeNC-IL1.5-KOH did not show the typical peaks of the pure IL (**Figure 7-26**e). Although the exchange between the electrolyte and IL is in theory possible to happen, these results prove the stability of the IL layer on the catalyst surface by indicating no additional element in the electrolyte of FeNC-IL1.5 compared with FeNC.

Finally, a metal-free N-doped carbon catalyst using a similar synthesis strategy was also manufactured and tested in order to demonstrate the universality of this strategy. The same ionic liquid was added to a different starting metal-free nitrogen-doped porous carbon, labelled as NC, in order to obtain sample NC-IL. The N_2 adsorption results are shown in **Figure 7-27**(a, b), the surface area and total pore volume of NC and NC-IL have been summarized in **Table 7-8**. The visibly reduced N_2 uptake and pore volume indicates similarly to the FeNC-IL material that a layer of IL has been successfully formed in the pores. The water contact angle increased pore volume and thereby changed the pore size distribution. The water contact angle increased from 133º (NC) to 144º (NC-IL), indicting

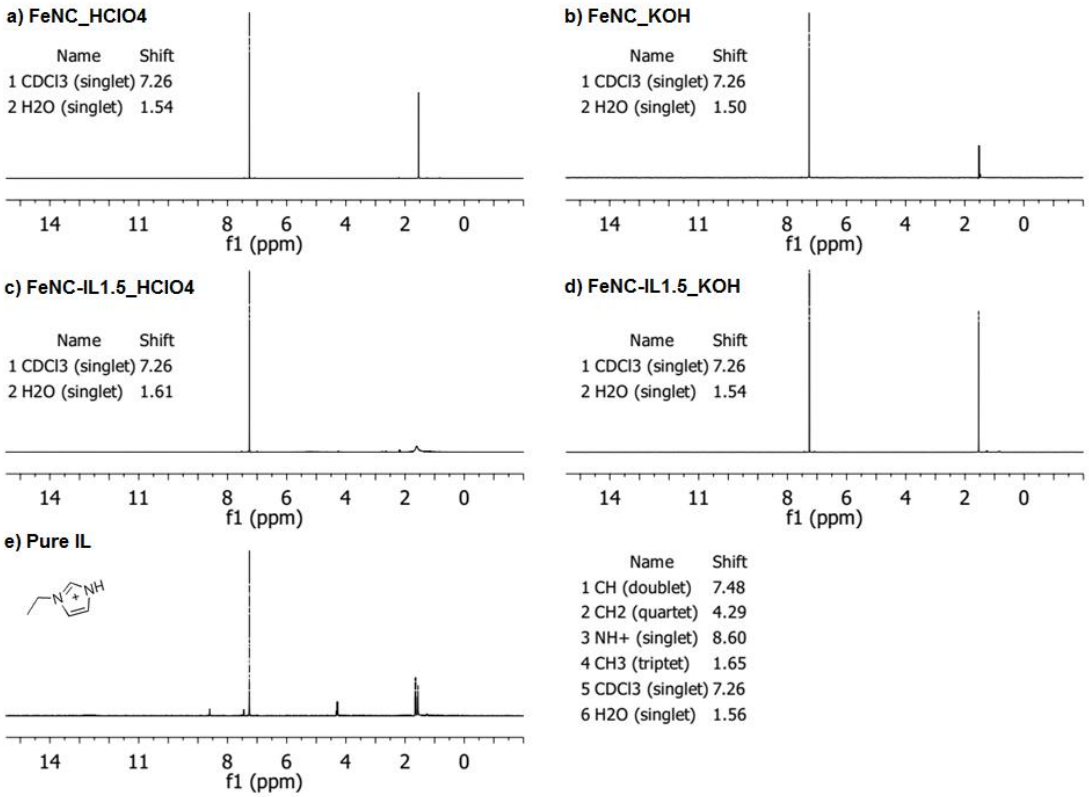

Figure 7-26 ^{1}H NMR spectrum of condensed electrolyte after long term stability test of (a) FeNC and (b) FeNC-IL1.5 in 0.1 M $HClO_4$ electrolyte, (c) FeNC and (d) FeNC-IL1.5 in 0.1 M KOH electrolyte, in comparsion with e) pure 1-Ethylimidazolium bis(trifluoromethylsulfonyl) imide.

the improvement of surface hydrophobicity. This improvement in surface hydrophobicity was further revealed by the water adsorption isotherm. In comparison with the case of FeNC-IL, the effect of the addition of the IL is more clearly seen. There is less interaction between the catalyst and water as demonstrated by the lower slope at low relative humidity, the micropore filling starts at higher RH and the water uptake is decreased (from 163 to 136 %), which is in line with the corresponding nitrogen adsorption isotherms. The FT-IR in **Figure 7-27**(d) confirmed the change of surface chemistry by demonstrating the additional adsorption signals of NC-IL compared with that of NC: the peaks at wavenumbers between 1000~1300 cm^{-1} and 3000~3200 cm^{-1} can be attributed

to the SO_2 and CF_3 vibrations, and the C-H stretching vibration mode of imidazole ring and alkyl chains.[115] This demonstrated the existance of IL on NC surface, similarly to the case of the FeNC-IL samples. Improved ORR catalytic activity in both acid and alkaline electrolyte has been recorded (**Figure 7-28**a, b): in acid electrolyte, the halfwave potential positively shifted from *ca.* 454 mV (NC) to *ca.* 508 mV (NC-IL). In alkaline electrolyte, the halfwave potential shifted from *ca.* 830 mV (NC) to *ca.* 844 mV (NC-IL). The corresponding Tafel plots, as can be seen in the inset of **Figure 7-28**(a, b), respectively, slightly decreased, demonstrating faster ORR kinetics after IL coating in both acid and alkaline electrolytes. The improved catalytic activity of NC after IL modification successfully demonstrated the universal applicability of this concept to different carbon materials.

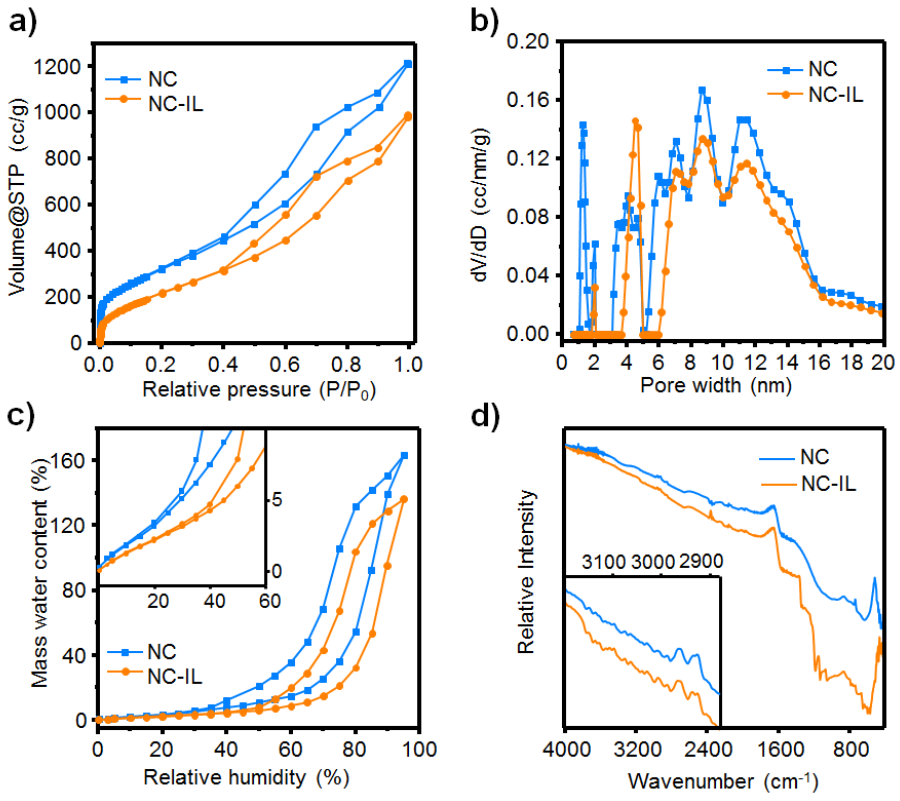

Figure 7-27 (a) N_2 sorption isotherms of NC and NC-IL. (b) QSDFT PSDs of NC and NC-IL. (c) H_2O vapor sorption isotherm at 20 ºC for the samples NC and NC-IL. The insets show zoomed isotherm at low relative humidity. The labels of inset X-axis and Y-axis are relative humidity (%) and mass water content (%), respectively (d) FT-IR spectra of the samples. The inset shows zoomed spectra in the 2800~3300 cm^{-1} range. The labels of inset X-axis and Y-axis are wavenumber (cm^{-1}) and relative intensity, respectively.

Table 7-8 Summary of specific surface area and QSDFT calculated total pore volume applied to the N_2 adsorption branch of FeNC before and after ionic liquid coating.

Sample	**BET**	
	S_{BET}(m^2/g)	**V_{total}(cc/g)**
NC	1069	1.5
NC-IL (mass corrected) *	515	0.9

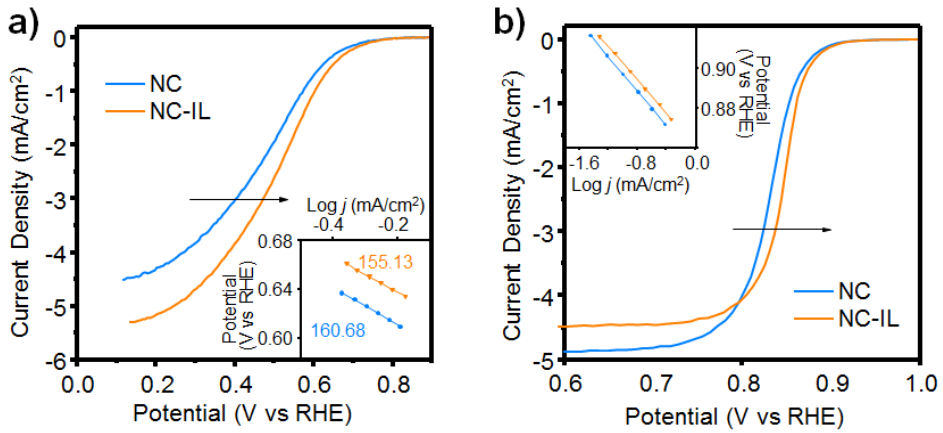

Figure 7-28 ORR performance for pristine and IL-modified NC catalysts. (a) LSV curves in O_2-saturated 0.10 M $HClO_4$ solution and (b) LSV curves in O_2-saturated 0.10 M KOH solution (rotating rate = 1600 rpm, scan rate = 10.0 mV s^{-1}). The insets show the corresponding Tafel plots derived from the LSV results.

7.3 Conclusions

In summary, this chapter has demonstrated an effective strategy to improve the ORR activity and long-term stability, by controlling the TPB to optimize the interface reaction of electrocatalyst surface microenvironment without changing the catalyst matrix. An oxygenophilic and hydrophobic ionic liquid was applied to serve as a water-equilibrated secondary medium on the electrocatalyst surface to facilitate mass transfer, so that the reactant O_2 and protons can easier access the active centres and therefore improve the utilization of the active sites. After IL modification, the Fe-N-C amorphous nanocarbon electrocatalysts outperformed the commercial Pt-C in both catalytic activity and long-term stability, at a lower cost compared with the scarce Pt. Furthermore, this IL layer served also as a reaction medium, expelling the water and any by-products of the ORR process. This has impeded such products from building up locally and therefore protected the active sites from being oxygenated or poisoned, which led to a remarkable

improvement in the long-term stability of the active sites. This study also demonstrates that the hydrophobic layer can have different effects on the reaction system, both positive and negative. Hence the ratio of IL needs to be carefully considered and balanced. Furthermore, this work indicates that the active sites of current electrocatalysts are not fully utilized, and the adsorption of oxygen on the active sites is the rate determining step in ORR. This new discovery is essential for future optimisation of nanocarbon ORR electrocatalysts. While pursuing the transformation to improve the critical property of the catalyst itself, whether these enhanced properties are fully utilized should also be paid attention to. Future studies need to be conducted using spectroscopic and modelling techniques to quantify the interactions between the IL and O_2 on the carbon catalysts as well as the role of water in the ORR reaction along with the O_2 concentration and the nature of the intermediates.

8 Conclusions and perspectives

In this thesis, facial strategies on surface engineering of advanced nanocarbon catalysts have been developed to create efficient, low cost and environmentally benign ORR electrocatalyst. This thesis firstly decoupled the influence of active sites and electric conductivity of the electrocatalyst and investigated the underlying relationships between them. The data showed that a low conductivity limits the exertion of active sites and results in a conductivity-dependent ORR activity. However, when the conductivity reaches critical value, the active sites can be fully utilized and contribute to a positively correlated ORR activity. Secondly, based on the above nanocarbon hybrid structure, an effective strategy was then proposed to enhance the oxygen reduction reaction (ORR) performance of MWCNTs in both acid and alkaline electrolytes by coating them with a layer of biomass derivative N-doped hydrothermal carbons. Thirdly, for the first time in the literature a general and effective strategy was demonstrated to improve the ORR activity of nanocarbon-based electrocatalysts via a facile modification with suitable ILs at room temperature. It was also demonstrated that the water solubility in the selected ILs can significantly determine the ORR activity. This modification strategy exhibited a remarkable ORR improvement in both alkaline and acid electrolytes. This work opened new research directions in efficient Pt-free catalyst development via tailoring the interfaces at the triple point.

The strategies applied in this thesis are powerful and can be actively applied to address more important fundamental issues such as the recognition on typical active sites, and the

validation of mechanisms via decoupling the main factors associated with ORR activity, which involve for example sandwiches structures, core-shell structure, etc.

Surface planting of ionic liquid as secondary hydrophobic oxygenophilic layer is an effective strategy to facilitate mass transfer process at TPB and protects active centre by expelling the produced water and by-product. Due to the fact that thick layer might hinder the electron conductivity, more work on nanostructure construction, such as the porosity of this secondary layer may be a way to explore and balance the electron conductivity and mass transfer.

Moreover, future research will also involve other ILs with higher hydrophobicity, oxygenophilicity and proton conductivity along with more fundamental understanding of the IL-electrocatalyst-O_2 interface. In addition, some specific issues need to be experimentally proved and clarified, those include but are not limited to: the catalytic activity of the pure ionic liquid, the proton conductivity and the mass transfer of oxygen and water molecular from/to the electrolyte - ionic liquid layer - catalyst surface.

Considering that the 3-electrode RDE/RRDE test system is different from the operation condition of real fuel cell devices, therefore the effectiveness of this concept and strategy need to be proved in real fuel cell devices.

Last but not least, more industrial alternative need to be explored, those alternatives need to be hydrophobic, oxygenphilic and have good proton/electron conductivity, and need to be stable in the electrochemistry environment (e.g. they should not be hydrolysed in acid or alkaline electrolyte).

9 Appendix: list of publications

Book Chapter

1 Kathrin Press[§], **Mo Qiao**[§], Magdalena Titirici. Vol II. CHAPTER 3. Hydrothermal Carbon Materials for the Oxygen Reduction Reaction *Carbon-Based Metal-Free Catalysts: Design and Applications*; Wiley. in press. ([§]**Equal contribution**) (Part of Chapter1 and Chapter 2 of this thesis)

Review Paper

2 Haofan Wang[§], Ruixuan Chen[§], Jingyu Feng[§], **Mo Qiao**[§] *etc*. Freestanding Non-Precious Metal Electrocatalysts for Oxygen Evolution and Reduction Reactions, *Chemelectrochem*. 2018, 5, 1786 DOI: 10.1002/celc.201800292R1 ([§]**Equal contribution**)

3 **Mo Qiao**, Magdalena Titirici. Surface engineering to promote non-precious carbon electrocatalysts in oxygen reduction reaction. *Chemistry - A European Journal*, 2018, DOI: 10.1002/chem.201804610 (Part of Chapter 1 and Chapter 3 of this thesis)

Research Paper

4 **Mo Qiao**, Guillermo A. Ferrero, Leticia F. Velasco, Wei Vern Hor, Yan Yang, Hui Luo, Peter Lodewyckx, Antonio B. Fuertes, Marta Sevilla, Maria-Magdalena Titirici*. Boosting the Oxygen Reduction Electrocatalytic Performance of Non-Precious Metal Nanocarbons via Triple Boundary Engineering using Protic Ionic Liquids. *Under*

submission (Part of Chapter 7 of this thesis)

5 **Mo Qiao,** Seyyed Shayan Meysami, Guillermo Alvarez Ferrero, Fei Xie, Han Meng, Nicole Grobert, and Maria-Magdalena Titirici, Low-cost chitosan-derived N-doped carbons boost electrocatalytic activity of multi-wall carbon nanotubes. *Adv. Funct. Mater*. 2018, 28, 1707284. DOI: 10.1002/adfm.201707284 (Chapter 6 of this thesis)

6 **Mo Qiao**, Cheng Tang, Liviu Cristian Tanase, Cristian Mihail Teodorescu, Chengmeng Chen, Qiang Zhang, Maria-Magdalena Titirici, Oxygenophilic Ionic Liquids Promote the Oxygen Reduction/Evolution Reaction in Metal-Free Nanocarbon Electrocatalysts, *Mater Horizons* 2017, 4**,** 895 DOI: 10.1039/c7mh00298j (Part of Chapter 7 of this thesis)

7 **Mo Qiao**, Cheng Tang, Guanjie He, Kaipei Qiu, Russell Binions, Ivan P. Parkin, Qiang Zhang, Zhengxiao Guo and Maria-Magdalena Titirici, Graphene/nitrogen-doped porous carbon sandwiches for the metal-free oxygen reduction reaction: conductivity versus active sites, *J. Mater. Chem. A,* 2016, 4, 12658 DOI: 10.1039/C6TA04578B (Chapter 5 of this thesis)

8 Guanjie He, **Mo Qiao**, Wenyao Li, Yao Lu, Tingting Zhao, Rujia Zou, Bo Li, Jawwad A. Darr, Junqing Hu, Maria-Magdalena Titirici, Ivan P. Parkin, S, N-Co-Doped graphene-nickel cobalt sulfide aerogel: Improved energy storage and electrocatalytic performance, *Advanced Science,* 2017, 4, 1600214 DOI:10.1002/advs.201600214

9 Guo-Liang Chai, Kaipei Qiu, **Mo Qiao**, Maria-Magdalena Titirici and Zhengxiao Guo, Identification and promotion of active Sites in P, N co-doped metal-free bifunctional

oxygen electrocatalysts, *Energy Environ. Sci.* 2017, 10, 1186 DOI: 10.1039/C6EE03446B

10 Yaxiang Lu, Lianqin Wang, Kathrin Preuss[§], **Mo Qiao**[§], Maria-Magdalena Titirici, John Varcoe, Qiong Cai, Halloysite-derived nitrogen doped carbon electrocatalysts for anion exchange membrane fuel cells, *Journal of Power Sources* 2017,372, 82 DOI: 10.1016/j.jpowsour.2017.10.037 ([§] **Equal contribution)**

11 Maria K. Rybarczyk, Yunming Li, **Mo Qiao**, Marek Lieder, Yong-Sheng Hu and Maria Magdalena Titirici, Hard carbon derived from rice husk as low cost negative electrodes in Na-ion batteries, *Journal of Energy Chemistry*, 2018, DOI: 10.1016/j.jechem.2018.01.025

12 Yaxiang Lu, Katherine Preuss[§], **Mo Qiao**[§], Maria-Magdalena Titirici, Qiong Cai, N-doped porous carbon electrocatalysts for oxygen reduction in alkaline media: effect of the amount of dopant and carbonization temperature, *under submission* ([§] **Equally contribution**)

In Process

13 **Mo Qiao**, *etc al*. The Influence of the Iron Amount and Chemical Environment on the Oxygen Reduction Reaction Activity of Nitrogen Doped Carbon Nanotubes.

10 References

1. O. Z. Sharaf and M. F. Orhan, *Renewable and Sustainable Energy Reviews*, 2014, **32**, 810-853.
2. J. B. Benziger, M. B. Satterfield, W. H. J. Hogarth, J. P. Nehlsen and I. G. Kevrekidis, *Journal of Power Sources*, 2006, **155**, 272-285.
3. in *Materials for Low-Temperature Fuel Cells*, DOI: doi:10.1002/9783527644308.ch02.
4. J. Wu, X. Yuan, H. Wang, M. Blanco, J. Martin and J. Zhang, *International Journal of Hydrogen Energy*, 2008, **33**, 1735-1746.
5. A. Zehtab Yazdi, H. Fei, R. Ye, G. Wang, J. Tour and U. Sundararaj, *ACS applied materials & interfaces*, 2015, **7**, 7786-7794.
6. J. Zhu, G. He, L. Liang, Q. Wan and P. K. Shen, *Electrochimica Acta*, 2015, **158**, 374-382.
7. B. Xia, Y. Yan, X. Wang and X. W. Lou, *Mater. Horiz.*, 2014, **1**, 379-399.
8. L. M. Dai, Y. H. Xue, L. T. Qu, H. J. Choi and J. B. Baek, *Chem Rev*, 2015, **115**, 4823-4892.
9. Y. Jiao, Y. Zheng, M. T. Jaroniec and S. Z. Qiao, *Chem Soc Rev*, 2015, **44**, 2060-2086.
10. G. Yang, W. Choi, X. Pu and C. Yu, *Energy Environ. Sci.*, 2015, **8**, 1799-1807.
11. J. Zhang, Z. Xia and L. Dai, *Science Advances*, 2015, **1**.
12. Z. Jiang, Z.-j. Jiang, X. Tian and W. Chen, *Journal of Materials Chemistry A*, 2014, **2**, 441-450.
13. Y. Nie, L. Li and Z. Wei, *Chemical Society reviews*, 2015, **44**, 2168-2201.

14. D. Chi Linh, P. Thy San, N. Ngoc Phong and T. Viet Quan, *Advances in Natural Sciences: Nanoscience and Nanotechnology*, 2013, **4**, 035011.

15. A. J. Bard, M. Stratmann and P. R. Unwin, *Encyclopedia of electrochemistry: Vol. 3: Instrumentation and electroanalytical chemistry*, Wiley-VCH, Weinheim, 2003.

16. F. M. Tchieno Melataguia, DOI: 10.13140/RG.2.1.3892.8881, 2016.

17. J. D. Costa, J. L. Lado, E. Carbó-Argibay, E. Paz, J. Gallo, M. F. Cerqueira, C. Rodríguez-Abreu, K. Kovnir and Y. V. Kolen'ko, *The Journal of Physical Chemistry C*, 2016, **120**, 16537-16544.

18. R. G. Compton and C. E. Banks, *Understanding Voltammetry*, 2007.

19. C. Song and J. Zhang, in *PEM Fuel Cell Electrocatalysts and Catalyst Layers: Fundamentals and Applications*, ed. J. Zhang, Springer London, London, 2008, DOI: 10.1007/978-1-84800-936-3_2, pp. 89-134.

20. X. Liu and L. M. Dai, *Nat. Rev. Mater.*, 2016, **1**, 12.

21. Q. H. Li, W. X. Chen, H. Xiao, Y. Gong, Z. Li, L. R. Zheng, X. S. Zheng, W. S. Yan, W. C. Cheong, R. A. Shen, N. H. Fu, L. Gu, Z. B. Zhuang, C. Chen, D. S. Wang, Q. Peng, J. Li and Y. D. Li, *Advanced materials*, 2018, **30**, 6.

22. N. Antonio Castro, G. Francisco and P. Nuno Miguel, *Physics World*, 2006, **19**, 33.

23. F. D. Kuanping Gong, Zhenhai Xia, Michael Durstock, Liming Dai, 2009, **323**, 5.

24. L. Tao, Q. Wang, S. Dou, Z. Ma, J. Huo, S. Wang and L. Dai, *Chemical communications*, 2016, **52**, 2764-2767.

25. A. Shen, Y. Zou, Q. Wang, R. A. Dryfe, X. Huang, S. Dou, L. Dai and S. Wang, *Angewandte Chemie*, 2014, **53**, 10804-10808.

26. Y. Jiao, Y. Zheng, M. Jaroniec and S. Z. Qiao, *Journal of the American Chemical Society*, 2014, **136**, 4394-4403.

27. I. R. G. Dangsheng Su, *ChemSusChem* 2015, **8**, 2772 – 2788

28. P. Zhang, F. Sun, Z. H. Xiang, Z. G. Shen, J. Yun and D. P. Cao, *Energy & Environmental Science*, 2014, **7**, 442-450.

29. C. Tang and Q. Zhang, *Advanced materials*, 2017, **29**.

30. C. Tang, H. F. Wang, X. Chen, B. Q. Li, T. Z. Hou, B. Zhang, Q. Zhang, M. M. Titirici and F. Wei, *Advanced materials*, 2016, **28**, 6845-6851.

31. Y. Zheng, Y. Jiao, L. Ge, M. Jaroniec and S. Z. Qiao, *Angewandte Chemie*, 2013, **52**, 3110-3116.

32. A. Kruse, A. Funke and M. M. Titirici, *Curr. Opin. Chem. Biol.*, 2013, **17**, 515-521.

33. Y. Liu, Y. Shen, L. Sun, J. Li, C. Liu, W. Ren, F. Li, L. Gao, J. Chen, F. Liu, Y. Sun, N. Tang, H. M. Cheng and Y. Du, *Nature communications*, 2016, **7**, 10921.

34. A. Kulkarni, S. Siahrostami, A. Patel and J. K. Nørskov, *Chemical Reviews*, 2018, **118**, 2302-2312.

35. T. Xing, Y. Zheng, L. H. Li, B. C. C. Cowie, D. Gunzelmann, S. Z. Qiao, S. Huang and Y. Chen, *ACS Nano*, 2014, **8**, 6856-6862.

36. H. B. Yang, J. Miao, S.-F. Hung, J. Chen, H. B. Tao, X. Wang, L. Zhang, R. Chen, J. Gao, H. M. Chen, L. Dai and B. Liu, *Science Advances*, 2016, **2**.

37. K. Mamtani, D. Jain, D. Zemlyanov, G. Celik, J. Luthman, G. Renkes, A. C. Co and U. S. Ozkan, *ACS Catalysis*, 2016, **6**, 7249-7259.

38. D. Guo, R. Shibuya, C. Akiba, S. Saji, T. Kondo and J. Nakamura, *Science*, 2016, **351**, 361-365.

39. W. Gu, L. Hu, J. Li and E. Wang, *Electroanalysis*, 2018, **30**, 1217-1228.

40. D. Liu, L. Tao, D. Yan, Y. Zou and S. Wang, *ChemElectroChem*, 2018, **5**, 1775-1785.

41. M. Shao, Q. Chang, J.-P. Dodelet and R. Chenitz, *Chemical Reviews*, 2016, **116**, 3594-3657.

42. W. Yang, X. Liu, X. Yue, J. Jia and S. Guo, *Journal of the American Chemical Society*, 2015, **137**, 1436-1439.

43. S. Koh and P. Strasser, *Journal of the American Chemical Society*, 2007, **129**, 12624-12625.

44. Y. P. Zhu, C. Guo, Y. Zheng and S.-Z. Qiao, *Accounts of Chemical Research*, 2017, **50**, 915-923.

45. A. Sarapuu, E. Kibena-Põldsepp, M. Borghei and K. Tammeveski, *J. Mater. Chem. A*, 2018, **6**, 776-804.

46. H. Huang, X. Wei and S. Gao, *Electrochimica Acta*, 2016, **220**, 427-435.

47. Z. I. Zhiyi Wu, Xianqin Wang, *Front. Chem. Sci. Eng.*, 2015, **9**, 280-294.

48. X. R. Wang, J. Y. Liu, Z. W. Liu, W. C. Wang, J. Luo, X. P. Han, X. W. Du, S. Z. Qiao and J. Yang, *Advanced Materials*, 2018, **30**, 10.

49. D. Geng, Y. Chen, Y. Chen, Y. Li, R. Li, X. Sun, S. Ye and S. Knights, *Energy & Environmental Science*, 2011, **4**, 760-764.

50. L. Qu, Y. Liu, J.-B. Baek and L. Dai, *ACS Nano*, 2010, **4**, 1321-1326.

51. K. Preuss, L. C. Tanase, C. M. Teodorescu, I. Abrahams and M. M. Titirici, *J. Mater. Chem. A*, 2017, **5**, 8.

52. R. Silva, D. Voiry, M. Chhowalla and T. Asefa, *Journal of the American Chemical Society*, 2013, **135**, 7823-7826.

53. C. H. Choi, C. Baldizzone, G. Polymeros, E. Pizzutilo, O. Kasian, A. K. Schuppert, N. Ranjbar Sahraie, M.-T. Sougrati, K. J. J. Mayrhofer and F. Jaouen, *ACS Catalysis*, 2016, **6**, 3136-3146.

54. M. Xiao, J. Zhu, L. Feng, C. Liu and W. Xing, *Advanced materials*, 2015, **27**, 2521-2527.

55. Y. Li, W. Zhou, H. Wang, L. Xie, Y. Liang, F. Wei, J. C. Idrobo, S. J. Pennycook and H. Dai, *Nat Nanotechnol*, 2012, **7**, 394-400.

56. Y. J. Sa, D.-J. Seo, J. Woo, J. T. Lim, J. Y. Cheon, S. Y. Yang, J. M. Lee, D. Kang, T. J. Shin, H. S. Shin, H. Y. Jeong, C. S. Kim, M. G. Kim, T.-Y. Kim and S. H. Joo, *Journal of the American Chemical Society*, 2016, **138**, 15046-15056.

57. W.-J. Jiang, L. Gu, L. Li, Y. Zhang, X. Zhang, L.-J. Zhang, J.-Q. Wang, J.-S. Hu, Z. Wei and L.-J. Wan, *Journal of the American Chemical Society*, 2016, **138**, 3570-3578.

58. J.-C. Li, P.-X. Hou, C. Shi, S.-Y. Zhao, D.-M. Tang, M. Cheng, C. Liu and H.-M. Cheng, *Carbon*, 2016, **109**, 632-639.

59. D. Dehui, Y. Liang, C. Xiaoqi, W. Guoxiong, J. Li, P. Xiulian, D. Jiao, S. Gongquan and B. Xinhe, *Angewandte Chemie International Edition*, 2013, **52**, 371-375.

60. M. Lefèvre, J. P. Dodelet and P. Bertrand, *The Journal of Physical Chemistry B*, 2002, **106**, 8705-8713.

61. H. Schulenburg, S. Stankov, V. Schünemann, J. Radnik, I. Dorbandt, S. Fiechter, P. Bogdanoff and H. Tributsch, *The Journal of Physical Chemistry B*, 2003, **107**, 9034-9041.

62. R. L. Arechederra, K. Artyushkova, P. Atanassov and S. D. Minteer, *ACS applied materials & interfaces*, 2010, **2**, 3295-3302.

63. E. Proietti, F. Jaouen, M. Lefevre, N. Larouche, J. Tian, J. Herranz and J. P. Dodelet, *Nat Commun*, 2011, **2**, 416.

64. M. Lefèvre, E. Proietti, F. Jaouen and J.-P. Dodelet, *Science*, 2009, **324**, 71-74.

65. U. I. Kramm, J. Herranz, N. Larouche, T. M. Arruda, M. Lefèvre, F. Jaouen, P. Bogdanoff, S. Fiechter, I. Abs-Wurmbach, S. Mukerjee and J.-P. Dodelet, *Physical Chemistry Chemical Physics*, 2012, **14**, 11673-11688.

66. M. Ferrandon, X. Wang, A. J. Kropf, D. J. Myers, G. Wu, C. M. Johnston and P. Zelenay, *Electrochimica Acta*, 2013, **110**, 282-291.

67. K. Singh, F. Razmjooei and J.-S. Yu, *J. Mater. Chem. A*, 2017, **5**, 20095-20119.

68. G. Wu, K. Artyushkova, M. Ferrandon, A. J. Kropf, D. Myers and P. Zelenay, *ECS Transactions*, 2009, **25**, 1299-1311.

69. Q. Wang, Z. Y. Zhou, Y. J. Lai, Y. You, J. G. Liu, X. L. Wu, E. Terefe, C. Chen, L. Song, M. Rauf, N. Tian and S. G. Sun, *Journal of the American Chemical Society*, 2014, **136**, 10882-10885.

70. F. J. Eric Proietti, Jean-Pol Dodelet, Michel Lefèvre, Nicholas Larouche, Juan Tian, Juan Herranz, Jean-Pol Dodelet, *Nature communications*, 2011.

71. E. P. Michel Lefèvre, Frédéric Jaouen, Jean-Pol Dodelet, *Science*, 2009, **324**, 4.

72. M. Lefevre, E. Proietti, F. Jaouen and J. P. Dodelet, *Science*, 2009, **324**, 71-74.

73. N. Ramaswamy, U. Tylus, Q. Jia and S. Mukerjee, *Journal of the American Chemical Society*, 2013, **135**, 15443-15449.

74. J. Deng, L. Yu, D. Deng, X. Chen, F. Yang and X. Bao, *J. Mater. Chem. A*, 2013, **1**, 14868-14873.

75. D. Deng, K. S. Novoselov, Q. Fu, N. Zheng, Z. Tian and X. Bao, *Nature Nanotechnology*, 2016, **11**, 218.

76. U. Tylus, Q. Jia, K. Strickland, N. Ramaswamy, A. Serov, P. Atanassov and S. Mukerjee, *The Journal of Physical Chemistry C*, 2014, **118**, 8999-9008.

77. L. L. Wenhan Niu, Xiaojun Liu, Nan Wang, Ji Liu, Weijia Zhou, Zhenghua Tanga and Shaowei Chen, *Journal of the American Chemical Society*, 2015, **137**, 8.

78. J. Liu, X. Sun, P. Song, Y. Zhang, W. Xing and W. Xu, *Advanced materials*, 2013, **25**, 6879-6883.

79. W. Niu, L. Li, X. Liu, N. Wang, J. Liu, W. Zhou, Z. Tang and S. Chen, *Journal of the American Chemical Society*, 2015, **137**, 5555-5562.

80. D. Deng, L. Yu, X. Pan, S. Wang, X. Chen, P. Hu, L. Sun and X. Bao, *Chemical communications*, 2011, **47**, 10016-10018.

81. Y. Chen, J. Li, T. Mei, X. g. Hu, D. Liu, J. Wang, M. Hao, J. Li, J. Wang and X. Wang, *Journal of Materials Chemistry A*, 2014, **2**, 20714-20722.

82. R. Sharma, J. H. Baik, C. J. Perera and M. S. Strano, *Nano letters*, 2010, **10**, 398-405.

83. C. Su, M. Acik, K. Takai, J. Lu, S. J. Hao, Y. Zheng, P. Wu, Q. Bao, T. Enoki, Y. J. Chabal and K. P. Loh, *Nature communications*, 2012, **3**, 1298.

84. W. Yuan, Y. Zhou, Y. Li, C. Li, H. Peng, J. Zhang, Z. Liu, L. Dai and G. Shi, *Scientific reports*, 2013, **3**, 2248.

85. Z. Wen, S. Ci, F. Zhang, X. Feng, S. Cui, S. Mao, S. Luo, Z. He and J. Chen, *Advanced materials*, 2012, **24**, 1399-1404.

86. A. H. Castro Neto, F. Guinea, N. M. R. Peres, K. S. Novoselov and A. K. Geim, *Reviews of Modern Physics*, 2009, **81**, 109-162.

87. L. Zhang, Q. Xu, J. Niu and Z. Xia, *Physical chemistry chemical physics : PCCP*, 2015, **17**, 16733-16743.

88. S. Anli, Z. Yuqin, W. Qiang, D. R. A. W., H. Xiaobing, D. Shuo, D. Liming and W. Shuangyin, *Angewandte Chemie*, 2014, **126**, 10980-10984.

89. Y. Jiang, L. Yang, T. Sun, J. Zhao, Z. Lyu, O. Zhuo, X. Wang, Q. Wu, J. Ma and Z. Hu, *ACS Catalysis*, 2015, **5**, 6707-6712.

90. C. Tang, B. Wang, H. F. Wang and Q. Zhang, *Advanced materials*, 2017, **29**.

91. D. Yan, Y. Li, J. Huo, R. Chen, L. Dai and S. Wang, *Advanced materials*, 2017, **29**.

92. M. M. Titirici and M. Antonietti, *Chem. Soc. Rev.*, 2010, **39**, 103-116.

93. R. J. White, N. Brun, V. L. Budarin, J. H. Clark and M. M. Titirici, *ChemSusChem*, 2014, **7**, 670-689.

94. B. Hu, K. Wang, L. Wu, S. H. Yu, M. Antonietti and M. M. Titirici, *Advanced materials*, 2010, **22**, 813-828.

95. E. Berl and A. Schmidt, *Justus Liebigs Annalen der Chemie*, 1932, **493**, 97-123.

96. M. M. Titirici, *Sustainable Carbon Materials from Hydrothermal Processes*, Wiley, 2013.

97. M. M. Titirici, A. Thomas, S.-H. Yu, J.-O. Müller and M. Antonietti, *Chemistry of Materials*, 2007, **19**, 4205-4212.

98. M.-M. Titirici, A. Thomas and M. Antonietti, *New Journal of Chemistry*, 2007, **31**, 787-789.

99. N. Baccile, G. Laurent, F. Babonneau, F. Fayon, M.-M. Titirici and M. Antonietti, *The Journal of Physical Chemistry C*, 2009, **113**, 9644-9654.

100. M.-M. Titirici, R. J. White, C. Falco and M. Sevilla, *Energy & Environmental Science*, 2012, **5**, 6796.

101. J. Wu, D. Zhang, Y. Wang and B. Hou, *Journal of Power Sources*, 2013, **227**, 185-190.

102. M. Qiao, C. Tang, G. He, K. Qiu, R. Binions, I. P. Parkin, Q. Zhang, Z. Guo and M. M. Titirici, *Journal of Materials Chemistry A*, 2016, **4**, 12658-12666.

103. Q. Li, R. Cao, J. Cho and G. Wu, *Advanced Energy Materials*, 2014, **4**, 19.

104. X. J. Zhou, J. L. Qiao, L. Yang and J. J. Zhang, *Adv. Energy Mater.*, 2014, **4**, 25.

105. W. J. Jiang, L. Gu, L. Li, Y. Zhang, X. Zhang, L. J. Zhang, J. Q. Wang, J. S. Hu, Z. Wei and L. J. Wan, *Journal of the American Chemical Society*, 2016, **138**, 3570-3578.

106. J. Wang, Z. Q. Huang, W. Liu, C. R. Chang, H. L. Tang, Z. J. Li, W. X. Chen, C. J. Jia, T. Yao, S. Q. Wei, Y. Wu and Y. D. Lie, *Journal of the American Chemical Society*, 2017, **139**, 17281-17284.

107. Y. J. Sa, D. J. Seo, J. Woo, J. T. Lim, J. Y. Cheon, S. Y. Yang, J. M. Lee, D. Kang, T. J. Shin, H. S. Shin, H. Y. Jeong, C. S. Kim, M. G. Kim, T. Y. Kim and S. H. Joo, *Journal of the American Chemical Society*, 2016, **138**, 15046-15056.

108. D. Malko, A. Kucernak and T. Lopes, *Nat. Commun.*, 2016, **7**, 7.

109. J. A. Varnell, E. C. M. Tse, C. E. Schulz, T. T. Fister, R. T. Haasch, J. Timoshenko, A. I. Frenkel and A. A. Gewirth, *Nature Communications*, 2016, **7**, 9.

110. C. Tang, H. F. Wang and Q. Zhang, *Acc Chem Res*, 2018, DOI: 10.1021/acs.accounts.7b00616.

111. T. Asefa, *Accounts of Chemical Research*, 2016, **49**, 1873-1883.

112. Y. Zheng, Y. Jiao and S. Z. Qiao, *Advanced Materials*, 2015, **27**, 5372-5378.

113. M. Qiao and M. M. Titirici, *Chemistry - A European Journal*.

114. B. Zheng, J. Wang, F.-B. Wang and X.-H. Xia, *Electrochemistry Communications*, 2013, **28**, 24-26.

115. B. Men, Y. Sun, M. Li, C. Hu, M. Zhang, L. Wang, Y. Tang, Y. Chen, P. Wan and J. Pan, *ACS Applied Materials & Interfaces*, 2016, **8**, 1415-1423.

116. W.-J. Niu, R.-H. Zhu, H. Yan, H.-B. Zeng, S. Cosnier, X.-J. Zhang and D. Shan, *Carbon*, 2016, **109**, 402-410.

117. H. Fei, R. Ye, G. Ye, Y. Gong, Z. Peng, X. Fan, E. L. G. Samuel, P. M. Ajayan and J. M. Tour, *ACS Nano*, 2014, **8**, 10837-10843.

118. C. Hu, C. Yu, M. Li, X. Wang, Q. Dong, G. Wang and J. Qiu, *Chemical Communications*, 2015, **51**, 3419-3422.

119. P. Chen, T.-Y. Xiao, Y.-H. Qian, S.-S. Li and S.-H. Yu, *Advanced Materials*, 2013, **25**, 3192-3196.

120. Z.-j. Jiang, Z. Jiang and W. Chen, *Journal of Power Sources*, 2014, **251**, 55-65.

121. J. G. Sun, L. Wang, R. R. Song and S. B. Yanga, *Nanotechnology*, 2016, **27**, 7.

122. A. A. Ensafi, M. Jafari-Asl and B. Rezaei, *Electrochimica Acta*, 2016, **194**, 95-103.

123. C. Zhang, R. Hao, H. Liao and Y. Hou, *Nano Energy*, 2013, **2**, 88-97.

124. Y. Su, Y. Zhang, X. Zhuang, S. Li, D. Wu, F. Zhang and X. Feng, *Carbon*, 2013, **62**, 296-301.

125. J. Tai, J. Hu, Z. Chen and H. Lu, *RSC Advances*, 2014, **4**, 61437-61443.

126. C. Xu, Y. Su, D. Liu and X. He, *Physical Chemistry Chemical Physics*, 2015, **17**, 25440-25448.

127. I. M. Patil, M. Lokanathan and B. Kakade, *Journal of Materials Chemistry A*, 2016, **4**, 4506-4515.

128. D. Yu, E. Nagelli, F. Du and L. Dai, *The Journal of Physical Chemistry Letters*, 2010, **1**, 2165-2173.

129. Y. Zheng, Y. Jiao, J. Chen, J. Liu, J. Liang, A. Du, W. Zhang, Z. Zhu, S. C. Smith, M. Jaroniec, G. Q. Lu and S. Z. Qiao, *Journal of the American Chemical Society*, 2011, **133**, 20116-20119.

130. Y. Zhang, W.-J. Jiang, X. Zhang, L. Guo, J.-S. Hu, Z. Wei and L.-J. Wan, *Physical Chemistry Chemical Physics*, 2014, **16**, 13605-13609.

131. L. Chen, R. Du, J. Zhu, Y. Mao, C. Xue, N. Zhang, Y. Hou, J. Zhang and T. Yi, *Small*, 2015, **11**, 1423-1429.

132. B. Men, Y. Sun, M. Li, C. Hu, M. Zhang, L. Wang, Y. Tang, Y. Chen, P. Wan and J. Pan, *ACS applied materials & interfaces*, 2016, **8**, 1415-1423.

133. R. Y. Huilong Fei, Gonglan Ye, Yongji Gong, Zhiwei Peng, Xiujun Fan, Errol L. G. Samuel, Pulickel M. Ajayan, James M. Tour, *ACS Nano*, 2014, **8**.

134. C. Hu, C. Yu, M. Li, X. Wang, Q. Dong, G. Wang and J. Qiu, *Chemical communications*, 2015, **51**, 3419-3422.

135. T.-Y. X. Ping Chen , Yu-Hong Qian , Shan-Shan Li , and Shu-Hong Yu *Adv. Mater.* , 2013, **25**, 3192–3196.

136. Z. Jiang, Z.-j. Jiang, X. Tian and W. Chen, *J. Mater. Chem. A*, 2014, **2**, 441-450.

137. Y. Chen, J. Li, T. Mei, X. g. Hu, D. Liu, J. Wang, M. Hao, J. Li, J. Wang and X. Wang, *J. Mater. Chem. A*, 2014, **2**, 20714-20722.

138. C. Yu, P. Zhang, J. Wang and L. Jiang, *Advanced materials*, 2017, **29**.

139. P. Wang, T. Hayashi, Q. a. Meng, Q. Wang, H. Liu, K. Hashimoto and L. Jiang, *Small*, 2017, **13**, 1601250.

140. S. Park and B. N. Popov, *Fuel*, 2009, **88**, 2068-2073.

141. N. Karousis, N. Tagmatarchis and D. Tasis, *Chemical Reviews*, 2010, **110**, 5366-5397.

142. E. Zhang, G.-P. Hao, M. E. Casco, V. Bon, S. Grätz and L. Borchardt, *Journal of Materials Chemistry A*, 2018, **6**, 859-865.

143. Q. Wang, Z.-Y. Zhou, Y.-J. Lai, Y. You, J.-G. Liu, X.-L. Wu, E. Terefe, C. Chen, L. Song, M. Rauf, N. Tian and S.-G. Sun, *Journal of the American Chemical Society*, 2014, **136**, 10882-10885.

144. S. Holdcroft, *Chemistry of Materials*, 2014, **26**, 381-393.

145. I.-Y. Jeon, H.-J. Choi, S.-M. Jung, J.-M. Seo, M.-J. Kim, L. Dai and J.-B. Baek, *Journal of the American Chemical Society*, 2013, **135**, 1386-1393.

146. C. Tang, H. F. Wang and Q. Zhang, *Accounts of chemical research*, 2018, **51**, 881-889.

147. Z. Lu, W. Xu, J. Ma, Y. Li, X. Sun and L. Jiang, *Advanced materials*, 2016, **28**, 7155-7161.

148. P. Zhang, S. Wang, S. Wang and L. Jiang, *Small*, 2015, **11**, 1939-1946.

149. J. E. George, S. Chidangil and S. D. George, *Advanced Materials Interfaces*, 2017, **4**, 1601088.

150. M. F. Costa Gomes, J. Deschamps and D. H. Menz, *Journal of Fluorine Chemistry*, 2004, **125**, 1325-1329.

151. C. Tang, H.-F. Wang and Q. Zhang, *Accounts of Chemical Research*, 2018, **51**, 881-889.

152. Z. Burton and B. Bhushan, *Nano Letters*, 2005, **5**, 1607-1613.

153. G. P. Hao, N. R. Sahraie, Q. Zhang, S. Krause, M. Oschatz, A. Bachmatiuk, P. Strasser and S. Kaskel, *Chemical communications*, 2015, **51**, 17285-17288.

154. G.-P. Hao, N. R. Sahraie, Q. Zhang, S. Krause, M. Oschatz, A. Bachmatiuk, P. Strasser and S. Kaskel, *Chemical communications*, 2015, **51**, 17285-17288.

155. W. Tian, H. Li, B. Qin, Y. Xu, Y. Hao, Y. Li, G. Zhang, J. Liu, X. Sun and X. Duan, *J. Mater. Chem. A*, 2017, **5**, 7103-7110.

156. E. Yoo and H. Zhou, *ACS Nano*, 2011, **5**, 3020-3026.

157. *AIP Advances*, 2015, **5**, 067136.

158. S. Dou, L. Tao, R. Wang, S. El Hankari, R. Chen and S. Wang, *Advanced materials*, 2018, **30**, 1705850.

159. C. Chen, B. Liang, A. Ogino, X. Wang and M. Nagatsu, *The Journal of Physical Chemistry C*, 2009, **113**, 7659-7665.

160. S. Dou, L. Tao, J. Huo, S. Wang and L. Dai, *Energy & Environmental Science*, 2016, **9**, 1320-1326.

161. Z. Li, Q. Jiang, Z. Ma, Q. Liu, Z. Wu and S. Wang, *RSC Advances*, 2015, **5**, 79473-79478.

162. Z. Liu, Z. Zhao, Y. Wang, S. Dou, D. Yan, D. Liu, Z. Xia and S. Wang, *Advanced materials*, 2017, **29**, 1606207.

163. Z. Yongqi, O. Bo, X. Jing, J. Guichong, C. Shi, R. R. Singh and F. H. Jin, *Angewandte Chemie International Edition*, 2016, **55**, 8670-8674.

164. E. J. Biddinger and U. S. Ozkan, *The Journal of Physical Chemistry C*, 2010, **114**, 15306-15314.

165. S.-M. Yuen, C.-C. M. Ma, Y.-Y. Lin and H.-C. Kuan, *Composites Science and Technology*, 2007, **67**, 2564-2573.

166. V. Datsyuk, M. Kalyva, K. Papagelis, J. Parthenios, D. Tasis, A. Siokou, I. Kallitsis and C. Galiotis, *Carbon*, 2008, **46**, 833-840.

167. L. Chen, H. Xie, Y. Li and W. Yu, *Materials Letters*, 2009, **63**, 45-47.

168. J. A. Kim, D. G. Seong, T. J. Kang and J. R. Youn, *Carbon*, 2006, **44**, 1898-1905.

169. X. Wang, C. Ouyang, S. Dou, D. Liu and S. Wang, *RSC Advances*, 2015, **5**, 41901-41904.

170. Y. F. Li, S. M. Chen, W. H. Lai, Y. J. Sheng and H. K. Tsao, *The Journal of chemical physics*, 2013, **139**, 064703.

171. W. Zhenhai, C. Suqin, Z. Fei, F. Xinliang, C. Shumao, M. Shun, L. Shenglian, H. Zhen and C. Junhong, *Advanced materials*, 2012, **24**, 1399-1404.

172. H. Yang, J. J. Oluf, Z. Wei, C. L. N., X. Wei, B. N. J. and L. Qingfeng, *Angewandte Chemie International Edition*, 2014, **53**, 3675-3679.

173. H. T. Chung, J. H. Won and P. Zelenay, *Nature Communications*, 2013, **4**, 1922.

174. L. Zhiyi, X. Wenwen, M. Jun, L. Yingjie, S. Xiaoming and J. Lei, *Advanced materials*, 2016, **28**, 7155-7161.

175. E. Guerrini, M. Grattieri, A. Faggianelli, P. Cristiani and S. Trasatti, *Bioelectrochemistry*, 2015, **106**, 240-247.

176. S. Zhang, Q. Zhang, Y. Zhang, Z. Chen, M. Watanabe and Y. Deng, *Progress in Materials Science*, 2016, **77**, 80-124.

177. S. E. Goodwin, D. E. Smith, J. S. Gibson, R. G. Jones and D. A. Walsh, *Langmuir*, 2017, **33**, 8436-8446.

178. V. V. Singh, A. K. Nigam, A. Batra, M. Boopathi, B. Singh and R. Vijayaraghavan, *International Journal of Electrochemistry*, 2012, **2012**, 19.

179. G. R. Zhang, M. Munoz and B. J. Etzold, *ACS applied materials & interfaces*, 2015, **7**, 3562-3570.

180. J. Snyder, K. Livi and J. Erlebacher, *Advanced Functional Materials*, 2013, **23**, 5494-5501.

181. G.-R. Zhang, M. Munoz and B. J. M. Etzold, *Angewandte Chemie International Edition*, 2016, **55**, 2257-2261.

182. Y. Tan, C. Xu, G. Chen, N. Zheng and Q. Xie, *Energy & Environmental Science*, 2012, **5**, 6923.

183. J. Snyder, T. Fujita, M. W. Chen and J. Erlebacher, *Nature materials*, 2010, **9**, 904-907.

184. M. A. Sutton, N. Li, D. C. Joy, A. P. Reynolds and X. Li, *Experimental Mechanics*, 2007, **47**, 775-787.

185. H. Abudayyeh, .*Synthesis and Analysis of ZnO Nanowires*, 2012

186. N. Iwashita, in *Materials Science and Engineering of Carbon*, eds. M. Inagaki and F. Kang, Butterworth-Heinemann, 2016, DOI: https://doi.org/10.1016/B978-0-12-805256-3.00002-7, pp. 7-25.

187. J. Epp, in *Materials Characterization Using Nondestructive Evaluation (NDE) Methods*, eds. G. Hübschen, I. Altpeter, R. Tschuncky and H.-G. Herrmann, Woodhead Publishing, 2016, DOI: https://doi.org/10.1016/B978-0-08-100040-3.00004-3, pp. 81-124.

188. G.-P. Hao, A.-H. Lu, W. Dong, Z.-Y. Jin, X.-Q. Zhang, J.-T. Zhang and W.-C. Li, *Advanced Energy Materials*, 2013, **3**, 1421-1427.

189. I. Kondratowicz, M. Nadolska, S. Şahin, M. Łapiński, M. Prześniak-Welenc, M. Sawczak, E. H. Yu, W. Sadowski and K. Żelechowska, *Appl. Surf. Sci.*, 2018, **440**, 651-659.

190. S. S. Meysami, P. Dallas, J. Britton, J. G. Lozano, A. T. Murdock, C. Ferraro, E. S. Gutierrez, N. Rijnveld, P. Holdway, K. Porfyrakis and N. Grobert, *Nanoscale*, 2016, **8**, 11993-12001.

191. S. S. Meysami, A. A. Koós, F. Dillon, M. Dutta and N. Grobert, *Carbon*, 2015, **88**, 148-156.

192. S. S. Meysami, A. A. Koós, F. Dillon and N. Grobert, *Carbon*, 2013, **58**, 159-169.

193. S. S. Meysami, F. Dillon, A. A. Koós, Z. Aslam and N. Grobert, *Carbon*, 2013, **58**, 151-158.

194. G. A. Ferrero, K. Preuss, A. Marinovic, A. B. Jorge, N. Mansor, D. J. Brett, A. B. Fuertes, M. Sevilla and M. M. Titirici, *ACS Nano*, 2016, **10**, 5922-5932.

195. G. Büchel, K. K. Unger, A. Matsumoto and K. Tsutsumi, *Advanced Materials*, 1998, **10**, 1036-1038.

196. G. A. Ferrero, A. B. Fuertes, M. Sevilla and M.-M. Titirici, *Carbon*, 2016, **106**, 179-187.

197. Z. Yang and N. Nakashima, *Scientific Reports*, 2015, **5**, 12236.

198. D. W. Wang and D. S. Su, *Energy Environ Sci*, 2014, **7**, 576-591.

199. L. Dai, Y. Xue, L. Qu, H.-J. Choi and J.-B. Baek, *Chemical Reviews*, 2015, **115**, 4823-4892.

200. S. B. Yang, X. L. Feng, X. C. Wang and K. Mullen, *Angew Chem Int Ed*, 2011, **50**, 5339-5343.

201. M. W. Chung, C. H. Choi, S. Y. Lee and S. I. Woo, *Nano Energy*, 2015, **11**, 526-532.

202. G. L. Chai, Z. F. Hou, D. J. Shu, T. Ikeda and K. Terakura, *J Am Chem Soc*, 2014, **136**, 13629-13640.

203. L. Tao, Q. Wang, S. Dou, Z. Ma, J. Huo, S. Wang and L. Dai, *Chemical communications*, 2016, **52**, 2764-2767.

204. M. K. Rybarczyk, M. Lieder and M. Jablonska, *RSC Adv*, 2015, **5**, 44969-44977.

205. J. Duan, S. Chen, M. Jaroniec and S. Z. Qiao, *ACS Catalysis*, 2015, **5**, 5207-5234.

206. Z. H. Zhang and P. Y. Wu, *RSC Adv*, 2014, **4**, 45619-45624.

207. B. Hu, K. Wang, L. H. Wu, S. H. Yu, M. Antonietti and M. M. Titirici, *Advanced materials*, 2010, **22**, 813-828.

208. M. M. Titirici, R. J. White, N. Brun, V. L. Budarin, D. S. Su, F. del Monte, J. H. Clark and M. J. MacLachlan, *Chemical Society reviews*, 2015, **44**, 250-290.

209. L. Zhao, L.-Z. Fan, M.-Q. Zhou, H. Guan, S. Qiao, M. Antonietti and M.-M. Titirici, *Advanced materials*, 2010, **22**, 5202-5206.

210. J. Popovic, R. Demir-Cakan, J. Tornow, M. Morcrette, D. S. Su, R. Schlogl, M. Antonietti and M. M. Titirici, *Small*, 2011, **7**, 1127-1135.

211. R. Demir Cakan, M. M. Titirici, M. Antonietti, G. Cui, J. Maier and Y. S. Hu, *Chemical communications*, 2008, DOI: 10.1039/b805671b, 3759-3761.

212. J. Zhang, L. Qu, G. Shi, J. Liu, J. Chen and L. Dai, *Angewandte Chemie*, 2016, **55**, 2230-2234.

213. X. Fu, X. Hu, Z. Yan, K. Lei, F. Li, F. Cheng and J. Chen, *Chemical communications*, 2016, **52**, 1725-1728.

214. M. Kim, S. Hwang and J.-S. Yu, *Journal of Materials Chemistry*, 2007, **17**, 1656-1659.

215. J. R. Pels, F. Kapteijn, J. A. Moulijn, Q. Zhu and K. M. Thomas, *Carbon*, 1995, **33**, 1641-1653.

216. L. Roldan, S. Armenise, Y. Marco and E. Garcia-Bordeje, *Physical Chemistry Chemical Physics*, 2012, **14**, 3568-3575.

217. K. Stanczyk, R. Dziembaj, Z. Piwowarska and S. Witkowski, *Carbon*, 1995, **33**, 1383-1392.

218. G. Liu, X. G. Li, P. Ganesan and B. N. Popov, *Appl Catal B*, 2009, **93**, 156-165.

219. D. S. Geng, Y. Chen, Y. G. Chen, Y. L. Li, R. Y. Li, X. L. Sun, S. Y. Ye and S. Knights, *Energy Environ Sci*, 2011, **4**, 760-764.

220. L. F. Lai, J. R. Potts, D. Zhan, L. Wang, C. K. Poh, C. H. Tang, H. Gong, Z. X. Shen, L. Y. Jianyi and R. S. Ruoff, *Energy Environ Sci*, 2012, **5**, 7936-7942.

221. C. H. Choi, C. Baldizzone, J. P. Grote, A. K. Schuppert, F. Jaouen and K. J. Mayrhofer, *Angewandte Chemie*, 2015, **54**, 12753-12757.

222. D. Higgins, P. Zamani, A. Yu and Z. Chen, *Energy Environ. Sci.*, 2016, **9**, 357-390.

223. M. Qiao, C. Tang, G. He, K. Qiu, R. Binions, I. P. Parkin, Q. Zhang, Z. Guo and M. M. Titirici, *J. Mater. Chem. A*, 2016, **4**, 12658-12666.

224. M. Xiao, J. Zhu, L. Feng, C. Liu and W. Xing, *Advanced materials*, 2015, **27**, 2521-2527.

225. Y. Hu, J. O. Jensen, W. Zhang, L. N. Cleemann, W. Xing, N. J. Bjerrum and Q. Li, *Angewandte Chemie*, 2014, **126**, 3749-3753.

226. J. Sanetuntikul, C. Chuaicham, Y.-W. Choi and S. Shanmugam, *J. Mater. Chem. A*, 2015, **3**, 15473-15481.

227. P. Zhao, W. Xu, X. Hua, W. Luo, S. Chen and G. Cheng, *The Journal of Physical Chemistry C*, 2016, **120**, 11006-11013.

228. J. K. Florian Banhart, Arkady V. Krasheninnikov*, *ACS Nano*, 2011, **5(1)**.

229. J. Youngmi Yi, Elena Willinger, Marc G. Willinger Chinmoy Ranjan, and Robert Schlçgl, *ChemElectroChem*, 2015, **2**, 9.

230. V. Goellner, V. Armel, A. Zitolo, E. Fonda and F. Jaouen, *Journal of the Electrochemical Society*, 2015, **162**, H403-H414.

231. Y. Wang, L. L. Wang and C. Q. Sun, *Chemical Physics Letters*, 2009, **480**, 243-246.

232. J. Snyder, T. Fujita, M. W. Chen and J. Erlebacher, *Nature materials*, 2010, **9**, 904.

233. G.-R. Zhang, M. Munoz and B. J. M. Etzold, *ACS applied materials & interfaces*, 2015, **7**, 3562-3570.

234. Y. Ding, X. Sun, L. Zhang, S. Mao, Z. Xie, Z.-W. Liu and D. S. Su, *Angewandte Chemie*, 2015, **127**, 233-237.

235. Z. Yang, Z. Yao, G. Li, G. Fang, H. Nie, Z. Liu, X. Zhou, X. a. Chen and S. Huang, *ACS Nano*, 2012, **6**, 205-211.

236. J. Masa, W. Xia, M. Muhler and W. Schuhmann, *Angewandte Chemie International Edition*, 2015, **54**, 10102-10120.

237. X. Zhong, L. Liu, Y. Jiang, X. Wang, L. Wang, G. Zhuang, X. Li, D. Mei, J.-g. Wang and D. S. Su, *ChemCatChem*, 2015, **7**, 1826-1832.

238. C. Tang, H.-F. Wang, X. Chen, B.-Q. Li, T.-Z. Hou, B. Zhang, Q. Zhang, M.-M. Titirici and F. Wei, *Advanced materials*, 2016, **28**, 6845-6851.

239. C. Tang and Q. Zhang, *Advanced materials*, 2017, DOI: 10.1002/adma.201604103, n/a-n/a.

240. M. M. Zhang Gui-Rong, and Etzold Bastian J. M. , *Angew. Chem. Int. Ed*, 2016, **55**, 4.

241. J. L. Qiao, L. Xu, L. Ding, P. H. Shi, L. Zhang, R. Baker and J. J. Zhang, *Int. J. Electrochem. Sci.*, 2013, **8**, 1189-1208.

242. M. A. R. Martins, C. Neves, K. A. Kurnia, L. Santos, M. G. Freire, S. P. Pinho and J. A. P. Coutinho, *Fluid Phase Equilib.*, 2014, **381**, 28-35.

243. J. L. Anthony, J. L. Anderson, E. J. Maginn and J. F. Brennecke, *The Journal of Physical Chemistry B*, 2005, **109**, 6366-6374.

244. M. Qiao, C. Tang, L. C. Tanase, C. M. Teodorescu, C. Chen, Q. Zhang and M.-M. Titirici, *Materials Horizons*, 2017, **4**, 895-899.

245. T. Horikawa, Y. Zeng, D. D. Do, K.-I. Sotowa and J. R. Alcántara Avila, *Journal of Colloid and Interface Science*, 2015, **439**, 1-6.

246. L. F. Velasco, D. Snoeck, A. Mignon, L. Misseeuw, C. O. Ania, S. Van Vlierberghe, P. Dubruel, N. de Belie and P. Lodewyckx, *Carbon*, 2016, **106**, 284-288.

247. Y. Li, W. Zhou, H. Wang, L. Xie, Y. Liang, F. Wei, J.-C. Idrobo, S. J. Pennycook and H. Dai, *Nature Nanotechnology*, 2012, **7**, 394.

248. R. J. E. Härk, E. Lust, *ECS Transactions*, 2014, **59**, 8.

249. D. van der Vliet, D. S. Strmcnik, C. Wang, V. R. Stamenkovic, N. M. Markovic and M. T. M. Koper, *Journal of Electroanalytical Chemistry*, 2010, **647**, 29-34.

250. M. Qiao, S. S. Meysami, G. A. Ferrero, F. Xie, H. Meng, N. Grobert and M. M. Titirici, *Advanced Functional Materials*, **0**, 1707284.

251. M. Asad, P. Jonas, A. Ghulam, H. H. Yong, R.-Z. Francisco and F. Tim-Patrick, *Advanced Energy Materials*, 2018, **8**, 1701771.

252. F. L. Meng, Z. L. Wang, H. X. Zhong, J. Wang, J. M. Yan and X. B. Zhang, *Advanced Materials*, 2016, **28**, 7948-7955.

253. Q. T. Liu, X. F. Liu, L. R. Zheng and J. L. Shui, *Angew. Chem.-Int. Edit.*, 2018, **57**, 1204-1208.

254. Q. X. Lai, L. R. Zheng, Y. Y. Liang, J. P. He, J. X. Zhao and J. H. Chen, *Acs Catalysis*, 2017, **7**, 1655-1663.

255. W. Wei, L. Haiwei, P. Khaled, Z. Xiaodong, F. Xinliang and M. Klaus, *Angewandte Chemie International Edition*, 2014, **53**, 1570-1574.

256. A. Kelong, L. Yanlan, R. Changping, L. Lehui and L. Gaoqing, *Advanced materials*, 2013, **25**, 998-1003.

257. K. Parvez, S. Yang, Y. Hernandez, A. Winter, A. Turchanin, X. Feng and K. Müllen, *ACS Nano*, 2012, **6**, 9541-9550.

258. S. H. Ahn, X. W. Yu and A. Manthiram, *Advanced Materials*, 2017, **29**, 10.

259. E. L. Hu, X. Y. Yu, F. Chen, Y. D. Wu, Y. Hu and X. W. Lou, *Advanced Energy Materials*, 2018, **8**, 8.

260. Z. Liu, F. Sun, L. Gu, G. Chen, T. T. Shang, J. Liu, Z. Y. Le, X. Y. Li, H. B. Wu and Y. F. Lu, *Advanced Energy Materials*, 2017, **7**, 6.

261. S. Li, C. Cheng, H. W. Liang, X. L. Feng and A. Thomas, *Advanced Materials*, 2017, **29**, 9.

262. J. Wei, Y. Liang, Y. X. Hu, B. A. Kong, G. P. Simon, J. Zhang, S. P. Jiang and H. T. Wang, *Angew. Chem.-Int. Edit.*, 2016, **55**, 1355-1359.

263. Y. J. Chen, S. F. Ji, Y. G. Wang, J. C. Dong, W. X. Chen, Z. Li, R. A. Shen, L. R. Zheng, Z. B. Zhuang, D. S. Wang and Y. D. Li, *Angew. Chem.-Int. Edit.*, 2017, **56**, 6937-6941.

264. J. Qiao, L. Xu, L. Ding, P. Shi, L. Zhang, R. Baker and J. Zhang, *International Journal of Electrochemical Science*, 2013, **8**, 1189-1208.

265. M. A. R. Martins, C. M. S. S. Neves, K. A. Kurnia, L. M. N. B. F. Santos, M. G. Freire, S. P. Pinho and J. A. P. Coutinho, *Fluid Phase Equilibr*, 2014, **381**, 28-35.